LUND UNIVERSITY

Automated Photoluminescence Experimentation for Understanding Dynamic Metal-Halide Perovskite Semiconductors

Kiligaridis, Alexander

2023

Document Version:
Publisher's PDF, also known as Version of record

Link to publication

Citation for published version (APA):
Kiligaridis, A. (2023). *Automated Photoluminescence Experimentation for Understanding Dynamic Metal-Halide Perovskite Semiconductors*. Lund.

Total number of authors:
1

General rights
Unless other specific re-use rights are stated the following general rights apply:
Copyright and moral rights for the publications made accessible in the public portal are retained by the authors and/or other copyright owners and it is a condition of accessing publications that users recognise and abide by the legal requirements associated with these rights.
• Users may download and print one copy of any publication from the public portal for the purpose of private study or research.
• You may not further distribute the material or use it for any profit-making activity or commercial gain
• You may freely distribute the URL identifying the publication in the public portal

Read more about Creative commons licenses: https://creativecommons.org/licenses/

Take down policy
If you believe that this document breaches copyright please contact us providing details, and we will remove access to the work immediately and investigate your claim.

LUND UNIVERSITY

PO Box 117
221 00 Lund
+46 46-222 00 00

Automated Photoluminescence Experimentation for Understanding Dynamic Metal-Halide Perovskite Semiconductors

ALEXANDER KILIGARIDIS
DEPARTMENT OF CHEMISTRY | FACULTY OF SCIENCE | LUND UNIVERSITY

Automated Photoluminescence Experimentation for Understanding Dynamic Metal-Halide Perovskite Semiconductors

Alexander Kiligaridis

LUND UNIVERSITY

DOCTORAL DISSERTATION

by due permission of the Faculty of Science, Lund University, Sweden. To be defended at Lecture hall B, Kemicentrum, Naturvetarvägen 16, 22362 Lund, Monday the 20th of November 2023 at 9:00 am.

Faculty opponent
Prof. Dr. Thomas Kirchartz

Organization: LUND UNIVERSITY, Division of Chemical Physics Department of Chemistry Box 124 SE-221 00 Lund, Sweden

Document name: Doctoral Dissertation **Date of issue**:

Author(s): Alexander Kiligaridis **Sponsoring organization:**

Title and subtitle: Automated Photoluminescence Experimentation for Understanding Dynamic Metal-Halide Perovskite Semiconductor

Abstract: Metal halide perovskites have garnered significant attention for their remarkable optoelectronic properties and unique photophysical characteristics. Combined with low cost for fabrication, this new class of materials is among the most promising candidates within next generation photovoltaic technologies. However, the complex nature of metal halide perovskites' crystal structures and compositions requires precise control during synthesis to achieve desired properties. Small variations in composition can significantly impact the material's behavior, demanding meticulous experimentation and characterization. Another challenge associated with the research of perovskite metal halides is the observer effect, a concept most often associated with quantum mechanics and refers to the alteration of a state by the act of observing it. In the context of perovskite materials, the very act of measurement or characterization can influence the material's behavior, potentially leading to discrepancies between observed and actual properties. Photoluminescence spectroscopy is a powerful analytical technique that plays a pivotal role in unraveling the optical properties and electronic behavior of perovskite materials. The emission of light upon excitation provides insights into the material's band structure, defect states and recombination dynamics. This thesis presents a comprehensive exploration of the convergence between photoluminescence spectroscopy and automation testing techniques, tailored to the specific requirements of metal halide perovskite materials. The integration of these two domains offers a novel approach to accelerate the characterization of the optoelectronic properties of metal halide perovskites. The integration of automation not only enhances the efficiency of experimentation but also enables the exploration of a wider parameter space. One of the examples that we will present in this work is a novel experimental methodology, incorporating photoluminescence measurements within a two-dimensional parameter space of excitation energy and laser pulse repetition frequency. We demonstrate the effectiveness of this technique in comprehensively investigating the dynamic photochemical properties of our material due to sample aging and degradation, photo-induced reversible and irreversible processes during the act of measuring.

Key words: Photoluminescence, Perovskites, Semiconductor, Spectroscopy, Microscopy

Classification system and/or index terms (if any)

Supplementary bibliographical information

Language: English **ISSN and key title**:

ISBN: 978-91-7422-998-1

Recipient's notes **Number of pages**: 56

Price Security classification

I, the undersigned, being the copyright owner of the abstract of the above-mentioned dissertation, hereby grant to all reference sources permission to publish and disseminate the abstract of the above-mentioned dissertation.

Signature Date 2023-10-12

Automated Photoluminescence Experimentation for Understanding Dynamic Metal-Halide Perovskite Semiconductors

Alexander Kiligaridis

LUND UNIVERSITY

Coverpicture by Yana Vaynzof

Faculty of Science, Department of Chemistry - Division Chemical Physics

isbn: 978-91-7422-998-1 (print)

isbn: 978-91-7422-999-8 (pdf)

Printed in Sweden by Media-Tryck, Lund University

Lund 2023

Media-Tryck is a Nordic Swan Ecolabel
certified provider of printed material.
Read more about our environmental
work at www.mediatryck.lu.se

MADE IN SWEDEN

Αφιερωμένο στους γονείς μου,
Ανδρονίκη και Γρηγόρη
και στην αδερφή μου Κατερίνα

Table of Contents

Abstract 8
Popular Science Summary 9
Populärvetenskaplig Sammanfattning 10
Acknowledgments 11
List of Papers 12
Abbreviations 14

Chapter 1 Introduction 15

1.1 Metal Halide Perovskite Materials 15
1.2 Photophysics of Semiconductors 16
1.2.1 Charge Carrier Recombination in Direct Bandgap Semiconductors 16
1.2.2 Shockley-Read-Hall and ABC Recombination Models 16
1.2.3 Photoluminescence Emission 18
1.2.4 Photoluminescence Quantum Yield 19
1.3 Photoluminescence Spectroscopy 20
1.3.1 Combining Photoluminescence Spectroscopy with Microscopy 20
1.3.2 Time-Resolved Photoluminescence 21
1.4 Metastable Photoluminescence Processes 22
1.4.1 Photosensitivity and Degradation 22
1.4.2 Observer Effect 23
1.4.3 Photoluminescence Blinking 24

Chapter 2 Experimental Methods 25

2.1 PLQY Portraits 25
2.1.1 Photoluminescence Intensity Dependence the on Excitation Power Fluence 26
2.1.2 PL Dependence on the Laser Repetition Rate 26
2.1.3 PLQY Portraits – Horse Method. 27
2.1.4 PLQY Portrait - Experimental Setup. 28
2.2 PLE Microscopy 29
2.1.1 PLE – Experimental Setup. 30

Chapter 3 Robot Microscope **31**
3.1 LabVIEW – Arduino 33
3.2 Horse Table – Recipe 33
3.2 Reference Points 34
3.3 Synchronization of the Optical Shutter 35
Chapter 4 Results & Discussion **38**
4.1 Paper I: Excitation Wavelength Dependence of Photoluminescence Flickering in Degraded $MAPbI_3$ Perovskite and its Connection to Lead Iodide Formation 38
4.2 Paper II: Impact of Excess Lead Iodide on the Recombination Kinetics in Metal Halide Perovskites 40
4.3 Paper III - Utilizing PLQY Portrait Method on $MAPI_3$ Films to Examine the Validity of the ABC and SRH Models 44
4.4 Paper IV - Fast Defect Kinetics in Non-Stoichiometric Hybrid Perovskite ($MAPbI_3$) Films 46
Chapter 5 Conclusions **50**
References **51**

Abstract

Metal halide perovskites have garnered significant attention for their remarkable optoelectronic properties and unique photophysical characteristics. Combined with low fabrication cost, this new class of materials is among the most promising candidates within the next generation photovoltaic technologies.

However, the complex nature of metal halide perovskites' crystal structures and compositions requires precise control during synthesis to achieve desired properties. Small variations in composition can significantly impact the material's behavior, demanding meticulous experimentation and characterization. Another challenge associated with the research of metal halide perovskites is the observer effect, a concept most often associated with quantum mechanics and refers to the alteration of a quantum system state by the act of observing it. In the context of perovskite halides materials, the very act of measurement or characterization can influence the material's behavior, potentially leading to discrepancies between observed and actual properties.

Photoluminescence spectroscopy is a powerful analytical technique that plays a pivotal role in unraveling the optical properties and electronic behavior of perovskite materials. The emission of light upon excitation provides insights into the material's band structure, defect states and charge recombination dynamics.

This thesis presents a comprehensive exploration of the convergence between photoluminescence spectroscopy and automation testing techniques, tailored to the specific requirements of the metal halide perovskite materials. The integration of these two domains offers a novel approach to accelerate the characterization of the optoelectronic properties of metal halide perovskites. The integration of automation not only enhances the efficiency of experimentation but also enables the exploration of a wider parameter space which is otherwise out of practical reach.

One of the examples that is presented in this work is a novel experimental methodology, incorporating photoluminescence measurements within a two-dimensional parameter space of the excitation energy and the laser pulse repetition frequency. We demonstrate the effectiveness of this technique by employing it to investigate the dynamic photochemical properties of our materials due to sample aging and degradation, as well as photo-induced reversible and irreversible processes during the act of measuring.

Popular Science Summary

Perovskite metal halides are a fascinating group of materials with incredible potential for revolutionizing technology, particularly in fields like solar energy and lighting. These materials exhibit remarkable optoelectronic properties that make them highly sought after for various applications. However, delving into the secrets of these materials comes with its own set of challenges, one of which is known as the observer effect.

Imagine trying to study something so delicate that just looking at it can change its behaviour. That is the predicament researchers face when investigating perovskite metal halides. The observer effect refers to how the act of observing or measuring these materials can alter their properties. It is like trying to take a photo of a butterfly without scaring it away – the mere presence of the observer can cause changes that you are trying to capture.

Perovskite metal halides are sensitive to light, heat, and even the equipment used for measurements. This means that when researchers try to understand their properties, they unintentionally modify them. It is as if the act of looking causes the material to change its behaviour, making it challenging to get accurate data about its true nature.

Despite the challenges, researchers are making significant strides in overcoming the observer effect. By collaborating across disciplines and using advanced technology, they are working to uncover the true potential of perovskite metal halides. The goal is to find ways to study these materials without altering their behaviour and to harness their incredible properties for efficient solar cells, better lighting, and more.

So, next time you hear about perovskite metal halides and their potential to change the way we power our world, remember the hidden challenge of the observer effect that researchers are tackling to unveil their secrets.

Populärvetenskaplig Sammanfattning

Perovskitmetallhalider är en fascinerande grupp material med otrolig potential att revolutionera teknologin, särskilt inom områden som solenergi och belysning. Dessa material uppvisar enastående optoelektroniska egenskaper som gör dem mycket eftertraktade för olika tillämpningar. Men att utforska dessa materials hemligheter kommer med sina egna utmaningar, varav en är känd som observatörseffekten.

Föreställ dig att försöka studera något så känsligt att bara att titta på det kan ändra dess beteende. Det är den situation forskare står inför när de undersöker perovskitmetallhalider. Observatörseffekten hänvisar till hur själva handlingen att observera eller mäta dessa material kan ändra deras egenskaper. Det är som att försöka ta en bild av en fjäril utan att skrämma den bort - observatörens närvaro kan orsaka förändringar som du försöker fånga.

Perovskitmetallhalider är känsliga för ljus, värme och till och med utrustningen som används för mätningar. Det innebär att när forskare försöker förstå deras egenskaper, ändrar de oavsiktligt på dem. Det är som om själva handlingen att titta på materialet får det att ändra beteende, vilket gör det svårt att få noggranna data om dess sanna natur.

Trots utmaningarna gör forskare betydande framsteg när det gäller att övervinna observatörseffekten. Genom samarbete över discipliner och användning av avancerad teknik arbetar de för att avslöja perovskitmetallhaliders sanna potential. Målet är att hitta sätt att studera dessa material utan att ändra deras beteende och dra nytta av deras otroliga egenskaper för effektiva solceller, bättre belysning och mer.

Så nästa gång du hör talas om perovskitmetallhalider och deras potential att förändra sättet vi driver vår värld på, kom ihåg den dolda utmaningen med observatörseffekten som forskare kämpar med för att avslöja deras hemligheter.

Acknowledgments

Firstly, I want to say a big thank you to my supervisor, Ivan. You have been a tremendous support throughout my PhD journey and research. We have had many interesting discussions about both work and personal matters, and I truly appreciate your mentorship and encouragement.

I am also grateful to my mentor and friend, Aboma, for introducing me to the world of research and for being a significant influence on my career. Your dedication and inspiration have played a crucial role in my academic and professional development.

Being part of the Single Molecule Spectroscopy group has been a wonderful experience. We have worked together, enjoyed pizza nights, and had fun outings to Ivan's country house. I am thankful for the friendship and the great memories we've made together.

I would also like to thank all the members of the Chemical Physics division for creating a positive work environment and organizing fun social activities. Your collective efforts have made my academic journey rewarding and enjoyable.

List of Papers

Paper I

Excitation wavelength dependence of photoluminescence flickering in degraded $MAPbI_3$ perovskite and its connection to lead iodide formation.

Alexander Kiligaridis, Aboma Merdasa, Carolin Rehermann, Eva L. Unger, Ivan G. Scheblykin. *Journal of Luminescence*, Volume 222, 117129, (2020). doi:10.1016/j.jlumin.2020.117129

Assisted AM in designing and calibrating the experimental setup. Analysed the data and wrote the manuscript together with IGS.

Paper II

Impact of Excess Lead Iodide on the Recombination Kinetics in Metal Halide Perovskites

Aboma Merdasa, **Alexander Kiligaridis**, Carolin Rehermann, Mojtaba Abdi-Jalebi, Jonas Stöber, Boris Louis, Marina Gerhard, Samuel D. Stranks, Eva L. Unger, Ivan G. Scheblykin. *ACS Energy Letters*, s. 1370-1378, (2019). doi:10.1021/acsenergylett.9b00774

Assisted AM in designing and calibrating the experimental setup. Also assisted AM in the experimental measurements.

Paper III

Are Shockley-Read-Hall and ABC models valid for lead halide perovskites?

Alexander Kiligaridis, Pavel A. Frantsuzov, Aymen Yangui, Sudipta Seth, Jun li, Qingzhi An, Yana Vaynzof, Ivan G. Scheblykin. *Nature Communications* 12, 3329, (2021). doi:10.1038/s41467-021-23275-w

Built the optical setup together with IGS. Designed the automated experimental protocol and its practical realization. Wrote the software to control the experimental setup and performed the measurements together with AY. Wrote the analysis software and performed the analysis on the experimental data. Wrote the manuscript together with IGS.

Paper IV

Photoluminescence Mapping over Laser Pulse Fluence and Repetition Rate as a Fingerprint of Charge and Defect Dynamics in Perovskites.

Shraddha M. Rao, **Alexander Kiligaridis**, Aymen Yangui, Qingzi An, Yana Vaynzof, Ivan G. Scheblykin. *Advanced Optical Materials*, 2300996, (2023). doi:10.1002/adom.202300996

Built the optical setup together with IGS. Wrote the software to control the experimental setup. Wrote the analysis software.

Abbreviations

CW – Continuous-Wave

EM-CCD – Electron Multiplying Charge-Coupled Device

MAPI – Methylammonium Lead Iodide

MHP – Metal Halide Perovskite

OD – Optical Density

PL – Photoluminescence

PLE – Photoluminescence Excitation

PLQY – Photoluminescence Quantum Yield

PSC – Perovskite Solar Cell

SRH – Shockley-Read-Hall

TRPL – Time Resolved Photoluminescence

Chapter 1 Introduction

1.1 Metal Halide Perovskite Materials

In the past decade, metal halide perovskites (MHPs) have become a promising star in the field of optoelectronics. The optoelectronic technologies based on MHPs, such as perovskite solar cells (PSCs), light emitting diodes, photodetectors and lasers, have been advancing the current paradigm due to the remarkable optoelectronic properties of MHPs.[1–4] This family of compounds, having the general formula of ABX_3 ($A = CH_3NH_3^+$ (MA), $HC(NH_2)_2^+$ (FA), and Cs^+, $B = Pb^{2+}$, Sn^{2+}, $X = I^-$, Cl^-, Br^-), has the advantages of easy and cost-efficient preparation. The crystal structure and chemical composition of MHPs give them their unique characteristics, including high optical absorption, high carrier mobility and long diffusion lengths,[5–9] while also enabling a high degree of flexibility and tunability.[10–12]

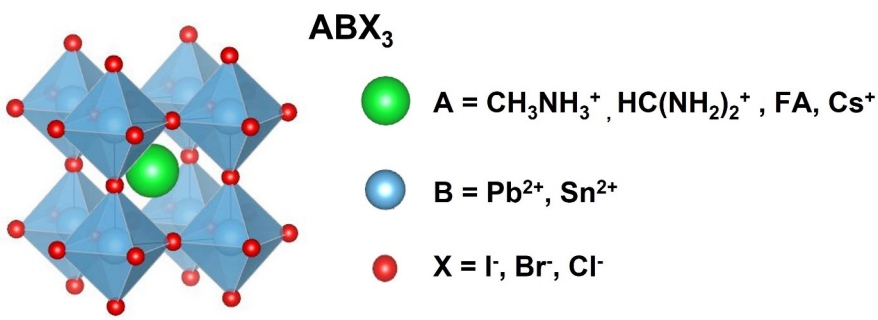

Figure 1. Structure of a metal halide perovskite with the general chemical formula ABX_3.

The typical ABX_3 perovskite has B at the centre of an octahedral $[BX_6]^{4-}$ cluster, with the BX_6 framework made up of corner-shared octahedrons. A is arranged in a 12-fold cuboctahedral coordination with X anions, located between the octahedral BX_6 framework (Figure 1).

The power conversion efficiency of PSCs has been improved from an initial 3.8% in 2009[13], to 25.7%, 28% and 31.3%, for single-junction PSCs, all-perovskite tandem solar cells and hybrid tandem PSCs respectively[14].

Despite of their remarkable properties and promising efficiencies in devices, there are great challenges in the research of MHP's, originating in both their long-term instability and also temporary and reversible photo-induced changes in the material when illuminated. In this thesis, I will present new experimental methods to further elucidate the optoelectronic properties of MHP's, specifically designed to take into account any changes introduced to the material by the act of studying it through light illumination.

1.2 Photophysics of Semiconductors

1.2.1 Charge Carrier Recombination in Direct Bandgap Semiconductors

Free charge carriers can be generated in a semiconductor when light with sufficient energy is absorbed, exciting electrons from the valence band, across the band gap to the conduction band. After the generation of a free electron-hole pair has occurred, the semiconductor system can return to its ground state when the mobile charge carriers have been eliminated through a variety of possible relaxation routes.

In the case of direct bandgap semiconductors, the three primary pathways for recombination are: radiative (band to band) recombination, trap-assisted non-radiative, and Auger recombination. The total energy of the system must be conserved.

(i) During the radiative band-to-band recombination, an electron-hole pair is annihilated, and the energy is emitted as a photon to produce photoluminescence (PL) emission.

(ii) In the case of trap-assisted non-radiative recombination, the excited carriers are trapped by crystal defect sites, and the energy is released as phonons progressively relaxing towards the ground state.

(iii) Finally, in the process of Auger recombination, which is also non-radiative, the excess energy released from the electron-hole recombination is transferred to a third charge carrier, which is excited to a higher energy level.

1.2.2 Shockley-Read-Hall and ABC Recombination Models

One of the models describing the kinetics of charge carrier concentrations in a semiconductor with defect states was proposed by Shockley and Read[15] and

independently by Hall[16] and is known as the Shockley–Read–Hall (SRH) model. It is important to note that in the SRH model the concentration of free electron can be different from the concentration of free holes, due to trapping in the defect states. Furthermore, only the non-radiative recombination of trapped electrons and free holes as well as the radiative band-to-band recombination are considered (the first and second order kinetic processes respectively). One possible realization of the model can be described by the following set of equations:

$$\frac{d}{dt}n(t) = G(t) - k_r np - k_t(N - n_t)n \qquad (1)$$

$$\frac{d}{dt}n_t(t) = k_t(N - n_t) - k_n n_t p \qquad (2)$$

$$\frac{d}{dt}p(t) = G(t) - k_r np - k_n n_t p \qquad (3)$$

Where $G(t)$ is density of the photogenerated carriers per second [$\mathrm{cm}^{-3}s^{-1}$], $n(t)$,$n_t(t)$ and $p(t)$ are the densities of electrons in the conduction band, trapped electrons and holes respectively (charge conservation: $n(t) + n_t(t) = p(t)$), N is the density of traps. k_r,k_t and $k_n$are radiative electron-hole recombination rate, electron trapping rate and non-radiative recombination rate of a trapped electron and a free hole respectively, see the scheme in Figure 2.

Shen et al.[17] suggested another simplified model called ABC, to account for the missing third order processes, most importantly the non-radiative Auger recombination. The name derives from the coefficients A, B, and C for the first-order (monomolecular), second-order (bi-molecular), and third-order Auger recombination, respectively, and the model is described by the equation

$$\frac{d}{dt}n(t) = -An - Bn^2 - Cn^3 \qquad (4)$$

An important difference between the two models is that in the ABC the concentration of free electrons and holes are always equal, which is not necessarily the case for the SRH due to presence of long-lived trapped charge carriers.

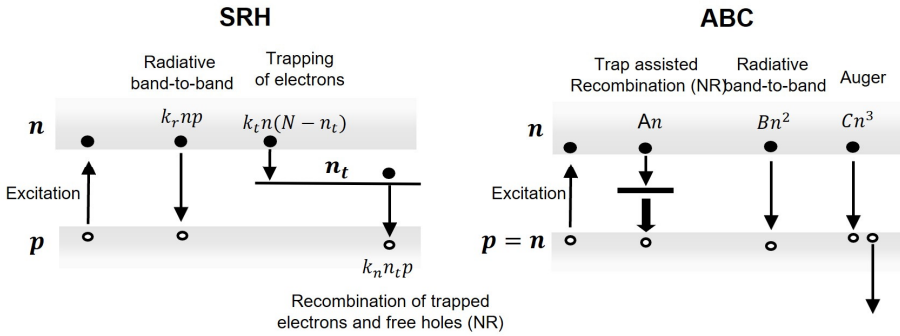

Figure 2. The energy level scheme and charge recombination processes of the SRH and ABC models.

1.2.3 Photoluminescence Emission

As mentioned earlier, during band-to-band recombination of free charge carriers in a direct band gap material, the energy is released in the form of emitting photons, the photoluminescence phenomenon. The physical processes involved in photoluminescence are much more intricate than absorption due to its close connection with the energy relaxation mechanisms within the solid. The emission spectrum is further influenced by the thermal distribution of electrons and holes in their respective bands.

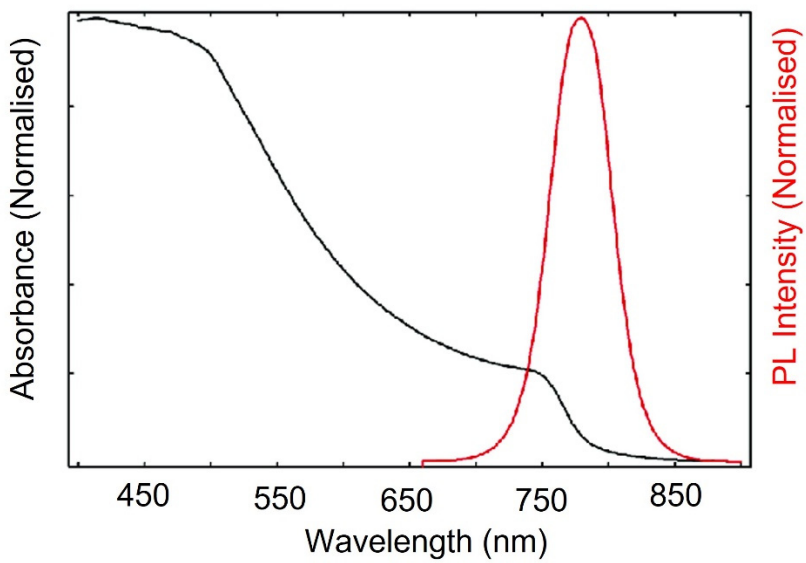

Figure 3. Absorption (black) and photoluminescence emission (red) spectra of a methylammonium lead iodide (MAPI) perovskite.

PL emission is purely a product of the bimolecular recombination of electrons and holes in the conduction and valence band respectively. Nonetheless, analysis of the PL signal can still give valuable information on the non-radiative relaxation processes as well, since the PL emission from a material is directly related to both radiative and nonradiative recombination rates (see the previous section).

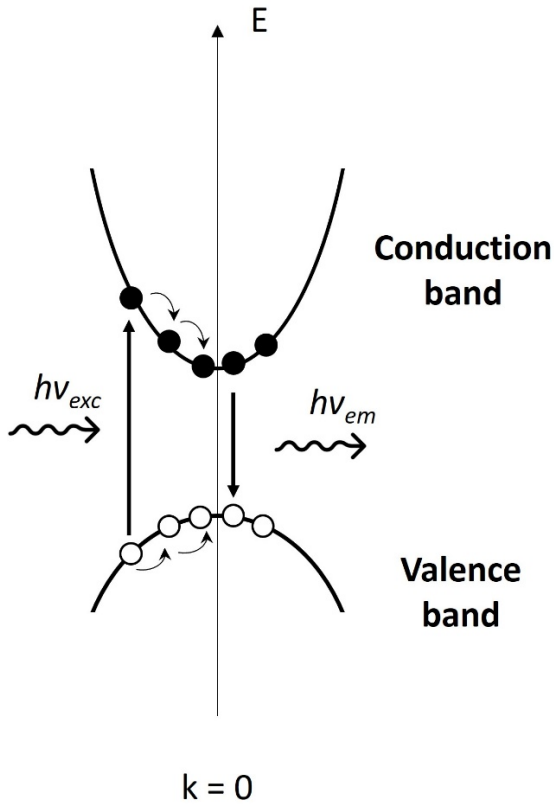

Figure 4. Diagram of the relaxation processes in the momentum-energy space preceding photoluminescence in a direct gap semiconductor.

1.2.4 Photoluminescence Quantum Yield

The ratio of the number of photons emitted to the total number of photons absorbed is referred to as the photoluminescence quantum yield ($PLQY, \Phi$) of the system.

In organic fluorophores, quantum yield is defined as:

$$\Phi = \frac{k_r}{k_r + \sum k_{nr}} \qquad (5)$$

where k_r is the rate constant for radiative relaxation and k_{nr} is the rate constant for all the non-radiative relaxation processes.

We can similarly define the photoluminescence quantum yield of a semiconductor. For each of the SRH and ABC models we get the following two equations respectively:

$$PLQY = \frac{k_r np}{k_r np + k_n n_t p} \qquad (6)$$

$$PLQY = \frac{k_r n^2}{Bn^2 + An} \qquad (7)$$

The PLQY of a semiconductor is a very interesting parameter which can give valuable information regarding the charge recombination processes.

1.3 Photoluminescence Spectroscopy

Photoluminescence spectroscopy is a field of study which employs a number of different techniques that typically involve exciting the sample by a light source (e.g. laser) and detecting the photoluminescence emission. The advantages of these techniques are that they are typically fast and non-destructive while simultaneously providing valuable information on the electronic structure and properties of materials.

1.3.1 Combining Photoluminescence Spectroscopy with Microscopy

A microscope can act as a platform for performing photoluminescence experiments. Fluorescence microscopes are instruments that study characteristics of organic or inorganic substances using fluorescence. The specimen is illuminated by light at a certain wavelength through the objective lens of the microscope, which is absorbed and causes the sample to emit light at longer wavelengths. The emission is collected by the microscope objective and a spectral emission filter is used to separate the excitation light from the fluorescence which is much weaker.

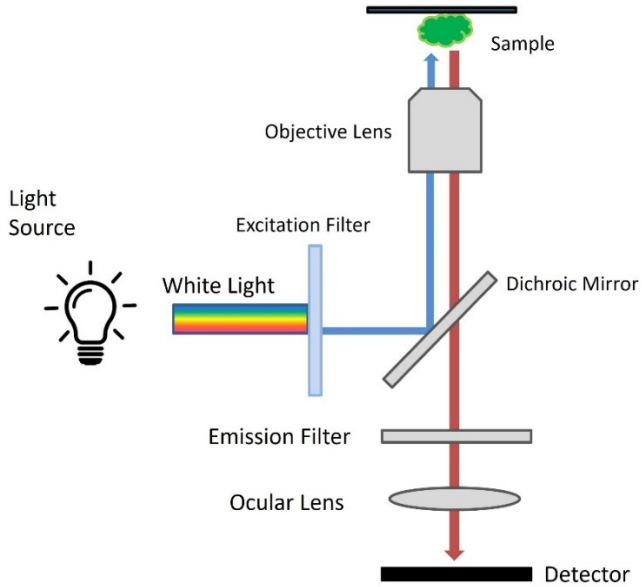

Figure 5. Schematic of a fluorescence microscope.

A light source, excitation filter, dichroic mirror and emission filter are the typical parts of a fluorescence microscope. The spectral excitation and emission properties of the material are considered when selecting the filters and the dichroic mirror.

By combining various spectroscopy techniques with the microscope, we can pinpoint many photophysical and photochemical properties of materials with diffraction-limited spatial resolution.

In the field of MHP semiconductor research, a broad range of PL methodologies have been applied combined with variation of temperature[18–20], and/or the excitation fluence[21–23], voltage dependence[24] and many other parameters. Today many if not all of these methods have been used with PL microscopes as the optical platforms with imaging capabilities to study devices, films, micro and nanocrystals. It is worth mentioning the role of PL microscopy in discovery and study of the fascinating phenomenon of PL blinking of these materials[18,25]. PL microscope combined with various spectroscopy techniques is the main instrument used in this thesis.

1.3.2 Time-Resolved Photoluminescence

Time-resolved photoluminescence (TRPL) is measured by marking the time between the sample excitation by a laser pulse and the arrival of the emitted photon at the detector. TRPL requires a defined “start”, provided by the electronics steering

the laser pulse, and a defined "stop" signal, realized by detection with single-photon sensitive detectors. The measurement of this time delay is repeated many times to account for the statistical nature of the PL emission. The detected events are then sorted into a histogram according to their arrival time which allows reconstruction of the photoluminescence decay. TRPL (Figure 6) is a very powerful tool for the study of fast electronic deactivation processes.

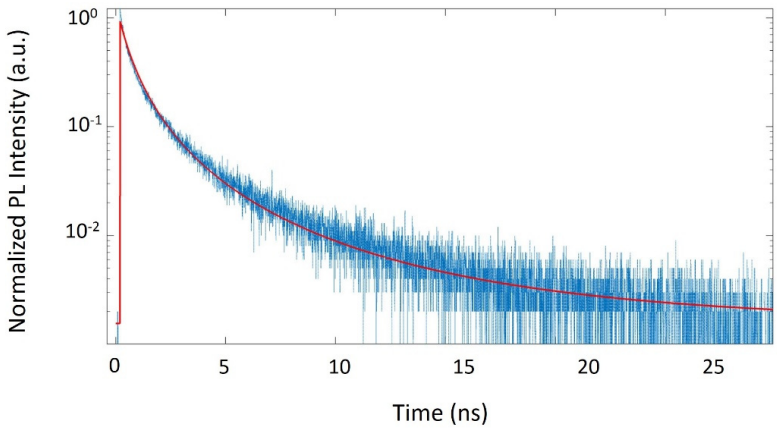

Figure 6. Example of a PL decay histogram. Blue represents the experimental data and the red curve shows a fit of the data.

1.4 Metastable Photoluminescence Processes

1.4.1 Photosensitivity and Degradation

For many luminescent materials, PL intensities are rather stable under constant low power excitation. However, this is not the case for most MHP materials. MHPs are well known for instability and metastability under illumination[25–29]. This is revealed as:

1. Fast induced processes, such as photoluminescence intensity enhancement and bleaching occurring within a time range of milliseconds to minutes of light exposure. Many of these effects can typically be reversed by switching off the excitation light (self-healing).[28,30–32]
2. Permanent changes in the chemical composition and crystal structure of the material when exposed to a combination of light, moisture and

oxygen[33–37]. These processes are generally slower, occurring over several hours or days.

1.4.2 Observer Effect

The observer effect is the phenomenon in which the act of observing a system influences the system being observed[38,39]. One of the most prominent examples is in quantum mechanics and the double slit experiment, which demonstrates the wave-particle duality of matter.[40,41] In this experiment, electron particles are sent through a barrier with two slits. The particles then hit a screen behind the barrier. The pattern that is created on the screen will depend on whether an observer is measuring which slit the particles are going through.

However, the observer effect can also be found in classical physics, as well as psychology and sociology. When measuring voltage for example, the connected voltmeter will draw some current from the circuit, thereby changing the voltage that is being measured.

It is important to consider the observer effect when studying MHPs by spectroscopic methods, since illumination by light will have a significant impact on the properties of the material due to its photosensitive nature, making it difficult to interpret the results of experiments.

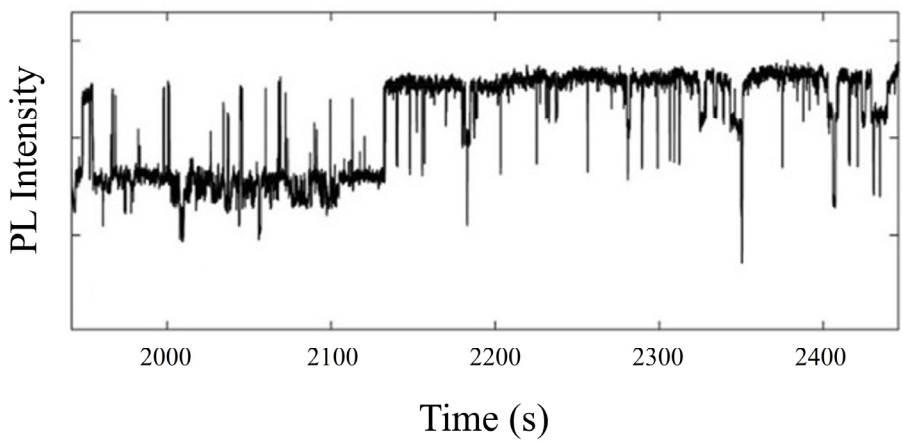

Figure 7. Experimental PL trace of MHP's crystals exhibiting PL blinking. Adapted from [25]

1.4.3 Photoluminescence Blinking

Photoluminescence intermittency, or blinking, is a phenomenon in which a fluorophore, such as a dye, molecule, or quantum dot, exhibits a sudden and random change in its fluorescence intensity under continuous excitation.[42–44] This change can occur on timescales ranging from microseconds to hours and can be observed as an apparent "blinking" of a fluorophore's fluorescence, as shown in Figure 7. Fluorescence intermittency is often used as a tool in single-molecule imaging and spectroscopy.[45–47] Although this phenomenon has been recognized to be characteristic of nanoscale objects, MHP micrometer-sized crystals have exhibited similar effect.[48–51] While the nature of these fluctuations in MHP materials is still under debate, it has been suggested that they are caused by the activation/passivation of extremely efficient quenching-defect states ("supertraps")[29,52]. Several studies have shown these PL fluctuations to be dependent on the size, composition and structure of the sample, as well as the external environment, such as temperature and light intensity[18,25].

Chapter 2 Experimental Methods

2.1 PLQY Portraits

In this chapter we will present a novel experimental photoluminescence measurement technique that involves mapping of the external PLQY in two-dimensional space as a function of both the excitation pulse fluence (*P*, in photons/cm^2) and excitation pulse frequency (*f*, in Hz). The acquired PLQY (y axis, log scale) is plotted against the average excitation density (= pulse fluence × repetition rate, W / cm^2, log scale) which we will further on refer to as PLQY or Horse portraits (Figure 8).

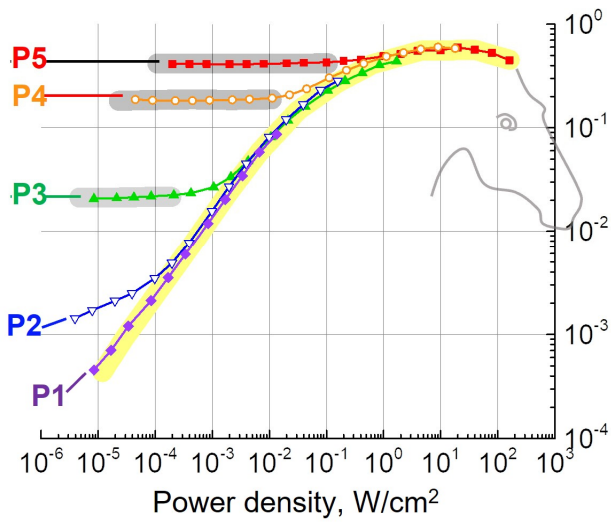

Figure 8. Example of a PLQY - Horse portrait. Each colored line (P1-P5) is a pulse fluence which is scanned over a large range of repetition rates of the pulsed laser (typically from 10KHz to 80MHz). Consecutive pulse fluences (P1-P2 , P2-P3, P3-P4, P4-P5) are different by a factor of 10. Adapted from Paper III.

The name Horse portrait was given to the plot because of the resemblance of the shape to that of a horse neck and mane from the data obtained originally from measurements on methylammonium lead iodide ($MAPbI_3$) MHP materials.

2.1.1 Photoluminescence Intensity Dependence the on Excitation Power Fluence

The more common and simple measurements of photoluminescence intensity dependence on the excitation power – PL(W), involves varying only the excitation fluence for either a continuous-wave (CW) excitation source or a pulsed laser at a specific repetition rate. This is typically achieved by placing a set of neutral attenuation filters (excitation filters) in the path of the laser beam. Several studies on MHPs have employed the PL(W) measurements, often in combination with PL decay, to fit recombination models with the experimental data.[21,23,53,54] Most of these models are based on SRH or ABC recombination theories, sometimes with the addition of diffusion terms. This allows for the extraction of fundamental material parameters, such as recombination rates and trap densities. We will further show, however, that measuring the PL as a function of solely the pulse fluence is not sufficient to obtain unambiguous results.

2.1.2 PL Dependence on the Laser Repetition Rate

When the excitation source is pulsed, we can distinguish two different regimes based on the effect of increasing or decreasing the repetition rate of the laser and monitoring the response of the PLQY.

i) **Single pulse regime**. Here, time (1/f) between consecutive laser pulses is long enough that all excited species created by one pulse (electrons, holes, trapped electron, trapped holes, excitons and so on) have returned to their ground state before the next incoming pulse (Figure 9a). In this case, each excitation has no memory from previous excitation events. In the single pulse regime, the external PLQY remains constant over scanning of the pulse repetition rate, since the PL intensity proportionally scales with the number of pulses within the same time window.

ii) **Quasi-CW regime**. In this condition the system does not have enough time to return to the ground state during the time between two consecutive pulses (Figure 9b). In other words, the population generated by one pulse is dependent on the history of the excitations by the previous pulses. This regime is evident for longer PL decay times (Figure 9b-i) but can also appear in samples with short PL decays where there are still long-lived states present in the system (trapped electrons – free holes or trapped holes – free electrons) (Figure 9b-ii). In the quasi-CW regime, the PL intensity

has a more complex dependence on the scanning of the repetition rate and the PLQY is no longer constant under such scanning.

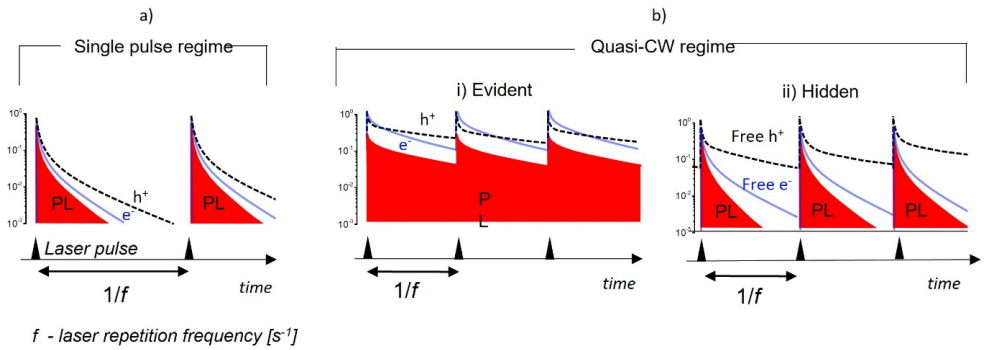

Figure 9. Illustration of the single pulse and quasi-cw regimes. Adapted from Paper III.

2.1.3 PLQY Portraits – Horse Method.

Measuring PLQY as function of average power density with lasers of only a few different repetition rates (Figure 10a) can produce ambiguous results since it is not possible to determine the excitation regime (see previous section). We therefore developed a new methodology of sweeping the pulse frequency over a large range at several fixed pulse fluences and measuring the PLQY (Figure 10b) which provides simple and certain separation between the single pulse and quasi-CW excitation regimes.

One of the challenges that arises is the multiplicity of data points, since we are scanning the excitation power density over pairs of laser pulse fluence and repetition rate. A typical PLQY portrait, like the one shown in Figure 10b, contains approximately 100 measurement points (combinations of pulse fluence (P) and repetition rate (f) pairs).

The average excitation power density (proportional to P*f) ranges over seven orders of magnitude, while the PL intensity is acquired from images obtained from a detector (CCD camera of the PL microscope in our case). To accomplish this in practice, the acquisition time of the detector needs to be substantially increased (up to 5-15mins per image) to compensate for the extremely weak PL signal at the lowest excitation powers. On the other hand, for the high pulse fluences and repetition rates, an additional set of neutral attenuation filters is introduced in the optical path between the sample and the detector (emission filters). It is also crucial to obtain the precise attenuation coefficient of the emission filters to convert the experimentally obtained PL signal to its non-attenuated value. All these parameters

are set and controlled during the experiment through a fully automated system, which will be further discussed in the next chapter.

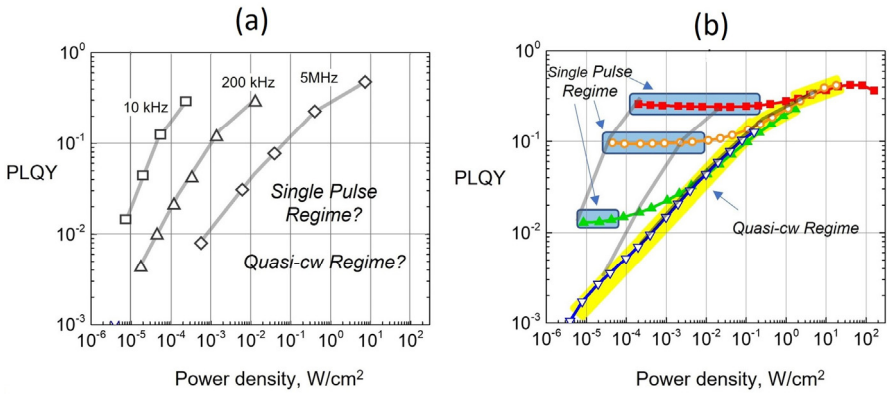

Figure 10. (a) PLQY as a function of power for three different repetition rates, (b) PLQY portrait where the repetition rate of the laser is instead scanned over a braod range for four different pulse fluences (red, orange, green and blue). Yellow shows the quasi-CW regime which is common for all pulse fluences.

The PLQY portraits are complemented with measuring the PL decays at a few combinations of pulse fluences and repetition rates, and together provides a clear and unambiguous criterion to test kinetic models.

2.1.4 PLQY Portrait - Experimental Setup.

The PLQY(f,P) map and PL decays were measured in a custom-built photoluminescence microscopy setup. A pulsed 485 nm laser (Pico Quant, 150 ps pulse width) was used to excite the sample through an objective lens (Olympus 40X, NA = 0.6) of a wide-field fluorescence microscope based on Olympus IX-71. The emission of the sample was then collected by the same objective and captured by one of two detectors. The first detector is an electron multiplying charge-coupled device (EM-CCD) (Princeton Inst. ProEM 512B) for measuring PL(f,P)) .

The second detector is a hybrid photomultiplier/single-photon detector (SPD, Picoquant PMA Hybrid-42) which is connected to a time correlated single photon counting module (Picoquant, Picoharp 300) for the measurement of PL decays kinetics. The instrumental response function width is 200 ps.

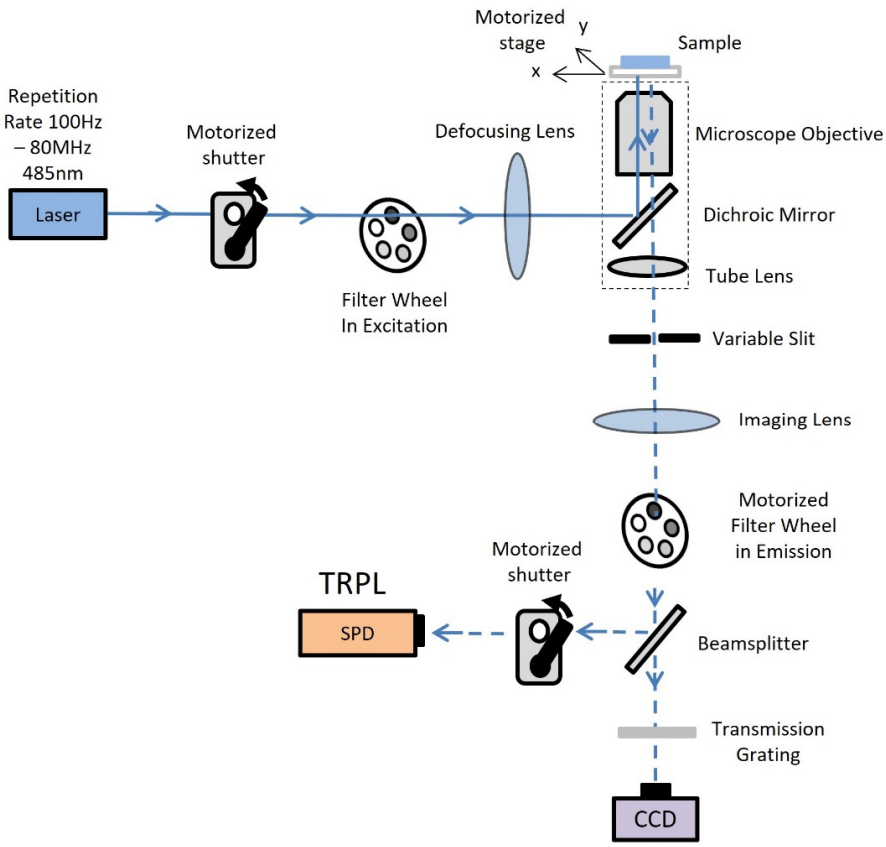

Figure 11. Schematic of the PL microscopy setup designed for measurements of PLQY(f,P) portraits and PL decays.

2.2 PLE Microscopy

Photoluminescence excitation (PLE) is a type of spectroscopic measurement where the wavelength of the excitation light is varied, and the PL intensity is monitored at a fixed emission wavelength of the material being studied.

Through the use of a microscope as the platform for PLE measurements, an advantageous technique is available to measure excitation spectra in situ, while also identifying spatially localized characteristics of the optical and electronic properties of the sample.

2.1.1 PLE – Experimental Setup.

The PLE experiments are conducted using a custom-made microscopy setup (Figure 12). The setup consists of a supercontinuum light source (SuperK Extreme, NKT Photonics) which generates pulsed white laser light. The output beam of the laser is directed to a rotating diffraction grating for creating a narrow (<1 nm) tunable excitation beam from 450 to 800 nm wavelength.

The samples are illuminated using an Olympus 40× objective lens, with a numerical aperture (NA) of 0.6, and the emitted PL is detected by the EM-CCD camera. As a result of this configuration, a wide-field PL image with diffraction-limited resolution is achieved for each of the selected excitation wavelengths. Linear variable long-pass and short-pass filters (3G LVLWP/LVSWP, Delta Optical Thin Film) are employed to significantly suppress (OD > 5) the excitation light before detection, thereby enabling single nanocrystal sensitivity. By illuminating the sample across a range of excitation wavelengths from 450 to 700nm, a set of PL images are obtained that provided all the necessary data for constructing spatially resolved excitation spectra of different parts of the sample.

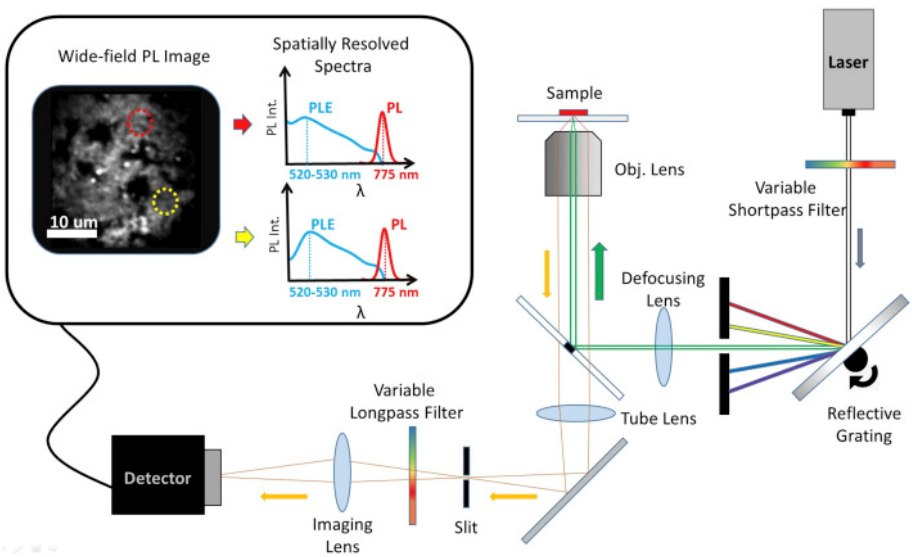

Figure 12. Schematic of photoluminescence excitation microscopy setup. Inserts illustrate $MAPbI_3$ photoluminescence excitation and emission spectra. Adapted from Paper I.

Chapter 3 Robot Microscope

Perovskite material is characterized by their high degree is instability and metastability. The same physical sample can produce significantly different experimental results depending on the measurement conditions. This experimental discrepancy can be attributed to:

- Sample aging. Due to the delicate stability of the material, the same sample, when repeatedly measured over the course of several days or weeks, behaves differently and leading to poor reproducibility of experimental results. Storing the sample in nitrogen and dark environment reduces but still does not prevent changes in the sample.

- Observer effect. Perovskites are especially unstable under light illumination. This means that during any spectroscopy measurements, the act of measuring is affecting the properties of the material and the results of the actual measurement. We have studied this effect to a great extent and introduced various methods to both monitor and mitigate it when we perform our PLQY(f, P) scanning.

Obtaining high degree of reproducibility during the synthesis of MHP samples is also a challenge. Samples prepared by individual scientists using the same preparation recipe very often exhibit different experimental behaviours. Sometimes even two samples prepared by same person and in the same sample-batch shows variations in optoelectronic properties[55].

In order to adequately study and understand the dynamic properties of our material due to i) sample aging and degradation, ii) photo-induced reversible and irreversible processes during the act of measuring (observer effect) as well as iii) sample to sample variation due to difficulties in the synthesis reproducibility, we need to explore a large volume-space of experimental data. We illustrate this by using the PLQY maps as an example (Figure 13). One PLQY(f,P) measurement alone is already a complicated, multi-parameter experiment, and therefore in order for us to practically be able to obtain a large number of PLQY maps it was crucial to build a fully automated experimental system, which we refer to as “Robot microscope”. This was achieved by designing and constructing several custom-built components

in the experimental setup, combining both our own hardware and software and integrating all the devices in one custom-built LabVIEW program, named "SMS-View", where SMS stands for Single Molecule Spectroscopy group.

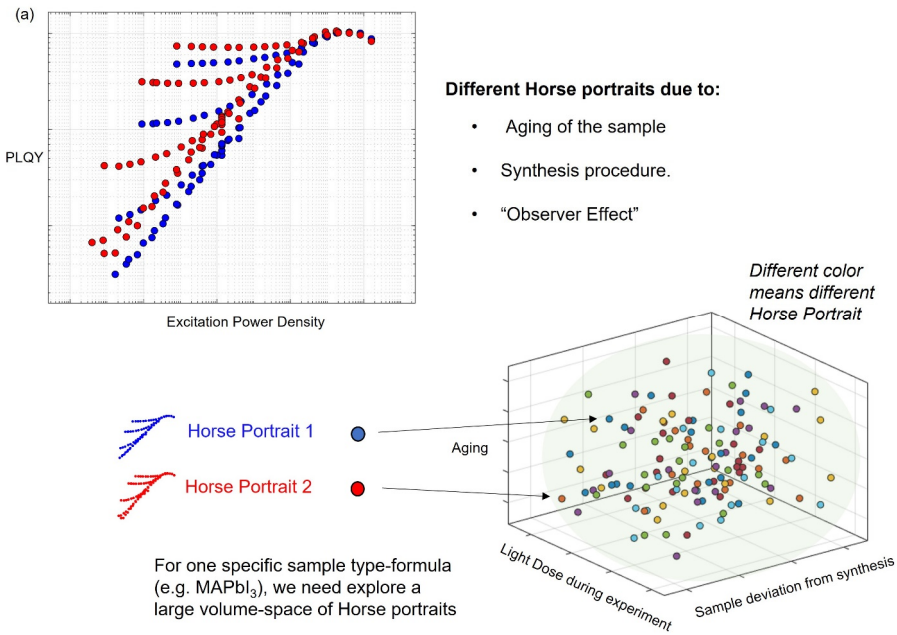

Figure 13. (a) Example of measured PLQY maps (Horse portrains) for two samples of the same formula ($MAPbI_3$). (b) Illustration of the large volume-space of possible experimental outcomes from the different samples of the same MHP material.

The advantage of automating the whole measurement process of Horse portraits is first an immense increase in efficiency. To manually measure a Horse portrait, a person would need to sit in the lab, change parameters, measure and save data for over 100 different measurement points, over a time duration of at least 8-10 hours. The robot microscope can perform the same measurement in less than 2 hours, with no need for supervision from an operator. Furthermore, a fully automated experimental procedure provides greatly improved accuracy of the measurements, eliminates the chance of human error and moreover can perfectly replicate precisely the same experimental conditions for each measurement.

3.1 LabVIEW – Arduino

LabVIEW is a graphical programming language commonly used in laboratory setups to easily control instruments, acquire and analyze data, and create custom user interfaces.

One of the key parts of the robot microscope is a custom-built LabVIEW program that was written and improved upon during the course of this doctoral thesis work. All the instruments and optical elements of the experimental setup are integrated in this "SMS-View" software. Below is a list of the main components which are part of the automated experimental setup.

- **EM-CCD Camera** - main detector for acquiring PL images.
- **Single-photon detector** - to obtain PL decays.
- **Pulsed Laser Module** - changing the repetition rate of the laser pulses.
- **Optical shutters** - Both for eye safety and protection of detectors but also to control and minimize the exposure of the sample to light.
- **Optical filter wheel** – in the excitation path, to change the laser pulse fluence.
- **Optical filter wheels** – in the emission path, in front of each detector to prevent them from saturation.
- **Beamspliter -** to redirect the light between either EM-CCD or the single-photon detector.
- **Motorized Sample Stage –** for high precision positioning of the sample.

For many of these components I designed custom-built systems to move or rotate them with the use of stepper-motors, dc-motors or servos connected to Arduino microcontrollers. An Arduino microcontroller is a cheap and easily programmable circuit board that can act as a communication bridge between the computer and SMS-View software with the physical components of the experimental setup. The SMS-View software sends the necessary instructions to the microcontrollers on how to translate or rotate the components during the automated experiments.

3.2 Horse Table – Recipe

To measure a full Horse portrait, the EM-CCD acquires a series of PL images, one for each combination of the laser repetition rate f and the pulse fluence P. In practice, the "SMS-View" software reads the instructions from input tables. These tables serve as an experiment recipe, and we can easily save and load different recipes

from text files. These recipes contain a step-by-step guide for the robot microscope on how to perform a desired complex experiment.

Experimental Parameters

	Laser Repetiton Rate (Hz)	CCD Exposure time (ms)	Excitation. Filter OD	Emission. Filter OD	Move X-Y Stage (µm)	……	……
Step 1.	10.000	6.000	4	1	0	……	……
Step 2.	500.000	4000	4	2	20	……	……
Step 3.	1.000.000	1000	3	2	0	……	……
…	3.000.000	200	3	3	-30	……	……
Step 500.	8.000.000	100	2	3	0	……	……

Figure 14. Example of an experimental recipe-table that is given as the input to the robot microscope.

Each row of the table is such a step and contains a combination of experimental parameters. The main parameters set in the table include repetition rate of the laser (f), optical filter in the laser beam to regulate the pulse power fluence (Exc.OD), optical attenuation of the emission to protect the detector from saturation (Em.OD) and exposure time of the CCD. The pulse power fluence and the emission attenuation are controlled by two motorized filter wheels placed in the excitation and emission path, respectively, each containing a set of neutral optical density (OD) filters.

3.2 Reference Points

Due to the observer effect and the dynamic changes of the sample during the experiment, we established a procedure involving measuring something that we call a reference point.

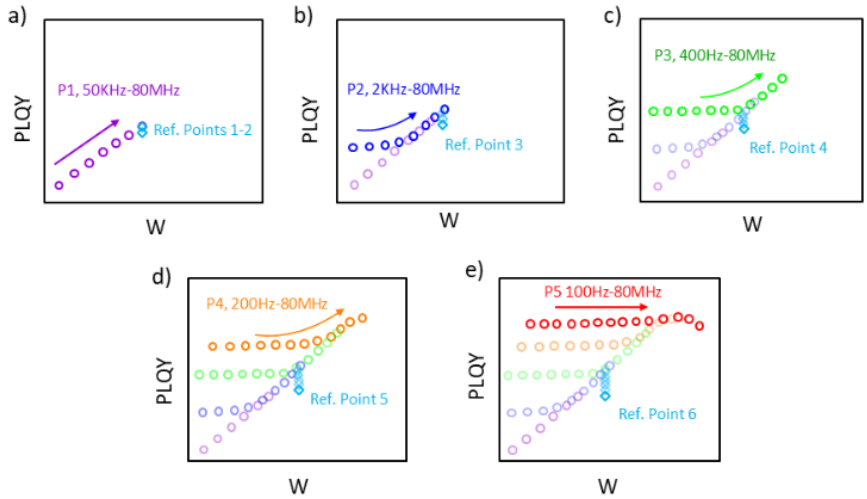

Figure 15. Example sequence in which one complete PL(f,P) map is measured. The entire scan is performed in a sequence of 5 measurements as schematically shown: a) P=P1, f scanned, with the reference points 1 and 2 measured before and after the scan respectively; b) P=P2, f scanned followed by the reference point 3; c) P=P3, f scanned followed by the reference point 4; d) P=P4, f scanned followed by the reference point 5; e) P=P5, f scanned and the full round is finished by measuring the final reference point 6. The change in the reference points in the figure is exaggerated to make it clearly distinguishable.

The reference point is a PL image (from which the PL intensity is determined) acquired at a specific combination of pulse fluence and repetition rate of the laser (P_{ref}, f_{ref}) and measured multiple times throughout one full Horse portrait. What this means is that a measurement starts with acquiring an PL image with reference parameters (P_{ref}, f_{ref}). It then acquires one or more measurement points (P_1, f_1), (P_2, f_2) … then again a reference point (P_{ref}, f_{ref}), and continue to alternate between measurements and the reference. Figure 15 illustrates the build-up of a Horse portrait during an experiment with reference points.

3.3 Synchronization of the Optical Shutter

To minimize photo-induced changes to the sample properties during experiments, the SMS-View program also controls an optical shutter which can block the laser excitation during the idle cycle of the setup, namely while different optical components are physically moving and turning in order to set the desired parameters in preparation for the image acquisitions, and only opens the shutter when everything is set for the EM-CCD to acquire an image. This way we can keep the amount of light soaking the sample to a bare minimum in order to reduce the

observer effect. Furthermore, since the opening-closing of the shutter is computer controlled and takes a known time, we can calculate the dose of light experienced by the sample with good precision.

Here it is important to distinguish between the two types of synchronization between the opening-closing of the shutter and the image acquisition by the EM-CCD:

1) Mode A. The sequence begins with the shutter opening, followed by the camera capturing the PL image. Once the image acquisition is complete, the shutter is closed (as illustrated in Figure 16a). In this scenario, as the EM-CCD initiates PL acquisition, the sample has already been exposed to light for a brief duration. Consequently, the resulting PL image records a later phase of the rapid dynamics of the PL. Also, the sample is exposed to light for time which is longer than necessary for the image acquisition.

2) Mode B. Initially, the camera acquisition starts, followed by the shutter opening and closing before the image acquisition is completed (as depicted in Figure 16b). This synchronization allows us to capture the initial onset of the PL dynamic processes. Also, all PL emitted the sample is detected.

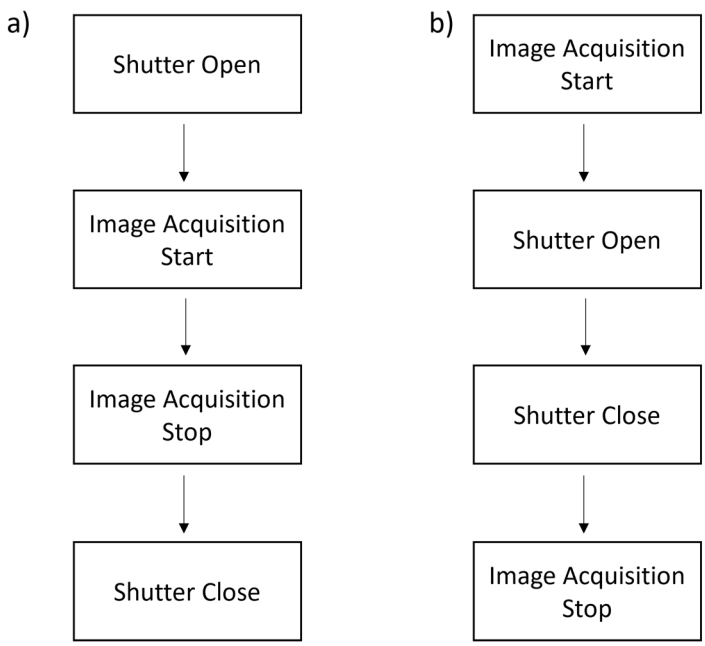

Figure 16. The two synchronization modes of the optical shutter and the CCD camera.

Applying either of these two types of synchronization may have substantial impact on the experimental results in the presence of the observer effect. Such is especially the case if the sample reveals fast dynamic PL properties when it is exposed to light, as illustrated in detail in Figure 17.

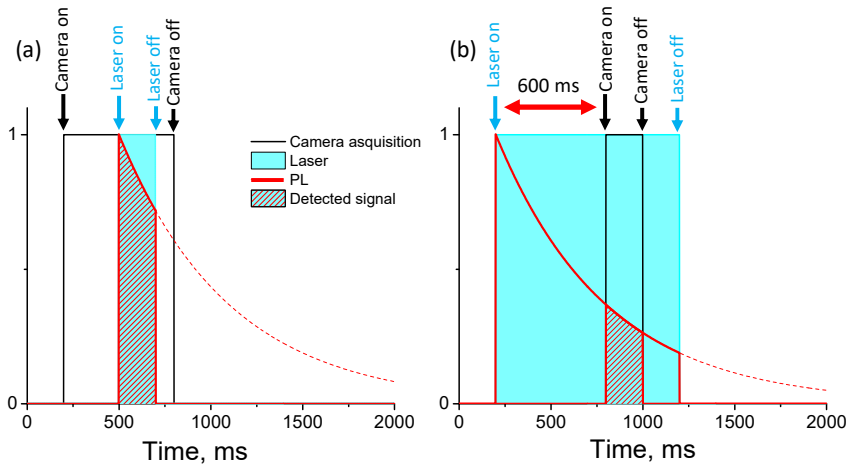

Figure 17. A schematic representation of the critical importance of synchronization between the laser irradiation interval and the signal acquisition window. The evolution of PL intensity after opening the laser shutter is shown by the red line. (a) Data acquisition in mode B, where the effective data acquisition time is equal to the laser irradiation time as both are determined by the laser shutter. (b) Data acquisition in the mode A, where there is a delay between the start of the laser illumination and the start of PL acquisition. This delay is 600 ms in our experiments. The acquisition time is 100 ms in both cases, however, the signal detected in (b) is several times smaller than in (a) due to the PL bleaching over the first 600 ms after opening the laser shutter. Adapted from Paper IV.

Chapter 4 Results & Discussion

4.1 Paper I: Excitation Wavelength Dependence of Photoluminescence Flickering in Degraded $MAPbI_3$ Perovskite and its Connection to Lead Iodide Formation

In Paper 1 we employ the PLE microscopy methodology to in-situ monitor the spatially resolved photo-degradation of methylammonium lead iodide ($MAPbI_3$) thin films. We show that the $MAPbI_3$ samples start exhibiting a distinguishable photoluminescence flickering mainly after degradation and formation of lead iodide (PbI_2). Further we report a clear dependence of the intensity of the PL flickering on the excitation wavelength.

The evolution of the photoluminescence image during the photodegradation of the $MAPbI_3$ film is depicted in Figure 18a–c. The power density in the laser spot caused a faster degradation in the central area, and a much slower degradation at the edges (region 2 in Figure 18c). After 1.5 hours of illumination, the PL in the centre of the excitation spot was largely replaced by PbI_2. Moreover, the regions that still exhibited strong PL (region 3 in Figure. 18c) showed PLE spectrum which has been identified as the result of PbI_2 formation on top of $MAPbI_3$.[56]

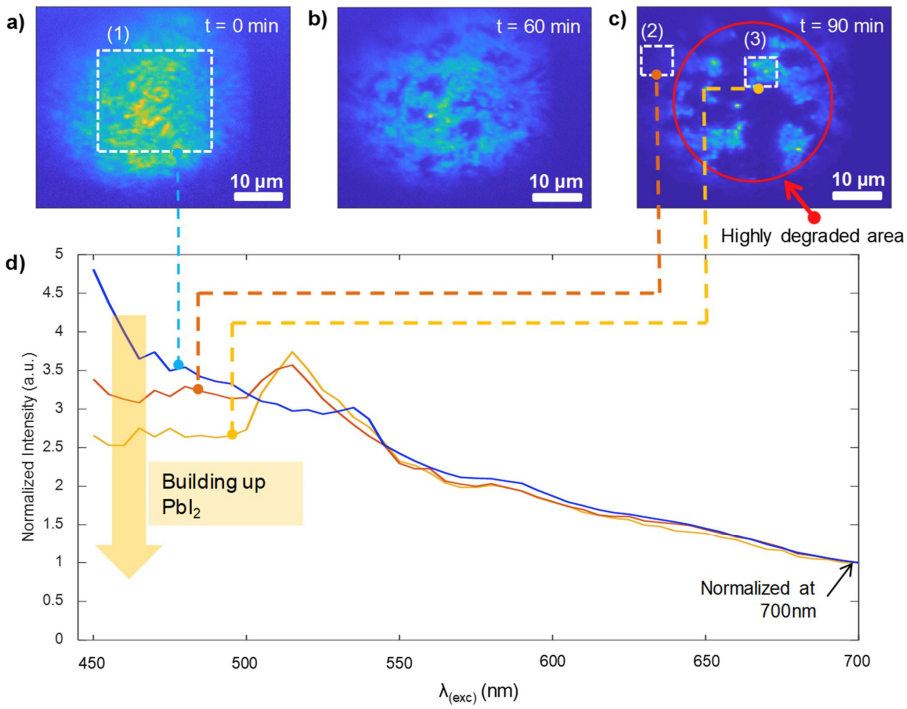

Figure 18. Wide-field photoluminescence images of the same area of a MAPbI3 film after (a) t = 0 (fresh film), (b) t = 60 min and (c) t = 90 min of 1 Sun illumination at ambient conditions. The PL intensity distribution in the fresh film reflects the laser excitation spot profile. (d) Photoluminescence excitation (PLE) spectra at different conditions: blue line - PLE of the fresh film, collected from region (1), orange line – PLE of a slightly degraded region (2), yellow line – PLE of the luminescence coming from region (3) in the highly degraded area. All PLE spectra are normalized at 700 nm. Adapted from Paper I.

For the regions of the sample that had been visibly degraded by photodegradation yet still exhibited luminescence corresponding to $MAPbI_3$ (Fig. 19c, region 3), the PL intensity flickering was much more prominent than in the less degraded parts of the film (Fig. 19c, region 2). This is evidenced by Figure 19b,d. Furthermore, the PL flickering effect fluctuated depending on the excitation wavelength. It was much more significant for $\lambda exc > 530$ nm, as is made clear by comparing the various panels of Figure 18d. In addition, no enhanced flickering occurred under low-energy excitation in region 2, which had only been slightly impacted by the photodegradation (Figure 18b).

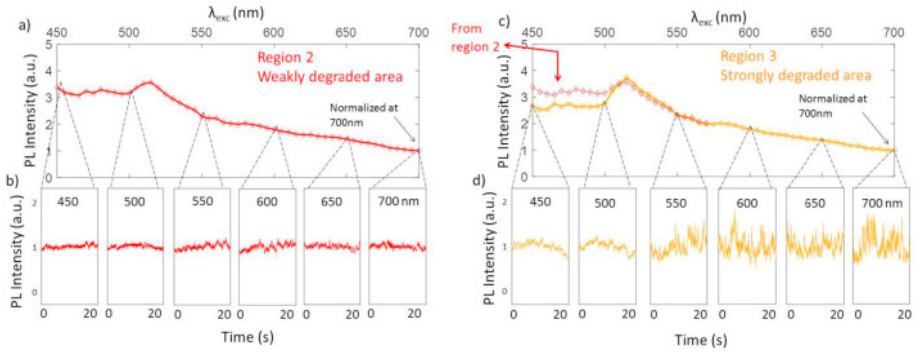

Figure 19. Photoluminescence excitation spectra of regions 2 (panel a)) and 3 (panel c)), see Fig. 2c for the PL image. b), d) - photoluminescence intensity time traces of regions 2 and 3 measured under different excitation wavelengths from 450 to 700 nm with steps of 50 nm. The excitation wavelength is indicated on each graph. Graphs in d) for $\lambda_{exc} \geq 550$ nm show strong PL intensity flickering. Also, see the video in SI for clarity. Adapted from Paper I.

It is possible that the wavelength dependence of the phenomenon may be connected to the excitation wavelength dependence of the photochemical reactions in the material, resulting in the formation or breakdown of the reversible non-radiative centres in $MAPbI_3$. An alternate hypothesis proposes that the PL flickering is diminished due to the restricted mobility of charge carriers, caused by their anchoring in the boundary layer between $MAPbI_3$ and PbI_2.

4.2 Paper II: Impact of Excess Lead Iodide on the Recombination Kinetics in Metal Halide Perovskites

In this work, we analyse the influence of excess lead iodide on the charge carrier recombination kinetics by measuring the PLE spectra and time-resolved photoluminescence as a function of excitation wavelength in the range from 450 to 780 nm. We recognize the presence of PbI_2 in the perovskite film with a distinctive spectroscopic signature in the PLE spectrum. Examining the recombination with and without this feature, we uncover a radiative bimolecular recombination mechanism induced by PbI_2. Investigating the photoluminescence spatially, we determine that this radiative process occurs in a confined region at the PbI_2/perovskite interface, which is only active when charge carriers are generated in PbI_2, thus providing a better understanding of how an excess of PbI_2 may enhance the capabilities of perovskite-based devices.

We carried out parallel PLE studies on 120 consecutive excitation scans, from which we obtained spectra for each scan. The experiments were conducted in ambient air conditions with a relative humidity of 40%, which are ideal for the formation of PbI_2

upon exposure to light[57]. The 2D maps in Figure 20a-b illustrate the changes in absorptance and normalized PLE spectra during the 6-hour measurement, with chosen spectra from three points in time plotted in Figure 20c-d. By examining the absorptance, we can confirm that $MAPbI_3$ decomposes into PbI_2. After 2.5 hours, we observe a noteworthy decrease in the PLE at the particular spectral range between 450 and 520 nm, which we call the "dip". This coincides with the PbI_2 absorption. We propose that this is caused by the filter effect; some of the photons that are absorbed by PbI_2 and generate charge carriers are consequently lost since PbI_2 emission (~520 nm) is blocked in our detection method[58].

In Figure 21, we utilize the time-correlated single-photon counting (TCSPC) approach and fit the PL decays to a stretched exponential function to acquire the average lifetimes. Before any extensive light-soaking, the mean lifetimes from both 450 and 700 nm excitation wavelengths are similar. The monoexponential behavior of the decays implies that the dominant recombination mechanism is trap-assisted. Despite the same photon flux, 450 nm excitation is expected to create a slightly higher carrier generation at the excited surface (where we detect PL), which is reflected in the marginally higher initial amplitude of the decay. Nevertheless, at t = 0 min this disparity in generation is not enough to bring about a dissimilar recombination mechanism.

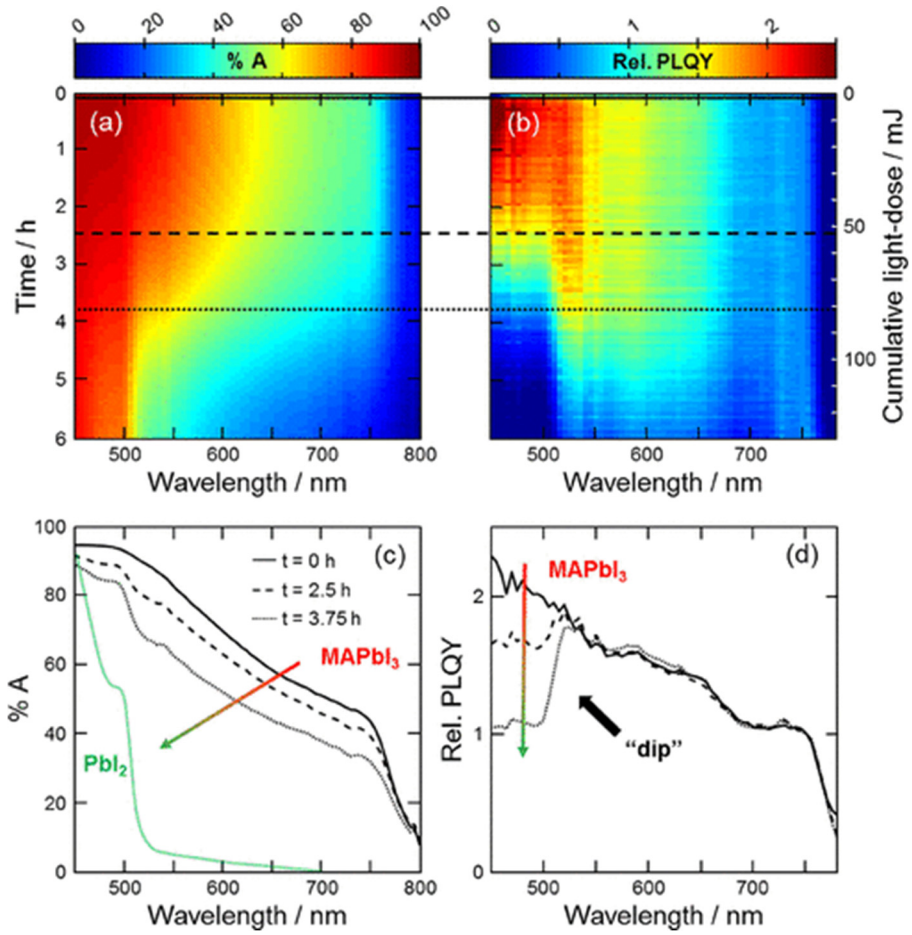

Figure 20. 2D maps showing the temporal evolution of (a) absorptance and (b) normalized PLQY spectra during 6 h of light-soaking. PLQY spectra are normalized at 750 nm. The right vertical axis shows the cumulative light dose throughout the experiment. (c,d) Selected spectra from the two maps at three points in time, t = 0 (solid), 2.5 (dashed), and 3.75 h (dotted). Adapted from Paper II.

In Figure 21b, we can perceive two different traits in the PL kinetics: (i) a boost in the slow decay component, visible directly when light-soaking begins, and (ii) a surge in the fast decay component, which appears after a few hours. Characteristic (i) occurs for both excitation wavelengths, while (ii) is exclusive to 450 nm. We can conclude that (i) was caused by the passivation of nonradiative recombination channels. Moreover, (ii) occurs when there is a marked dip in the PLE spectrum (t = 420 min), which is only observed when exciting in the spectral range of PbI_2 absorption (450–520 nm). As the detection excludes emission from PbI_2, we can infer that the carrier recombination kinetics can be altered in the perovskite simply by the presence of PbI_2, if photons are absorbed by it.

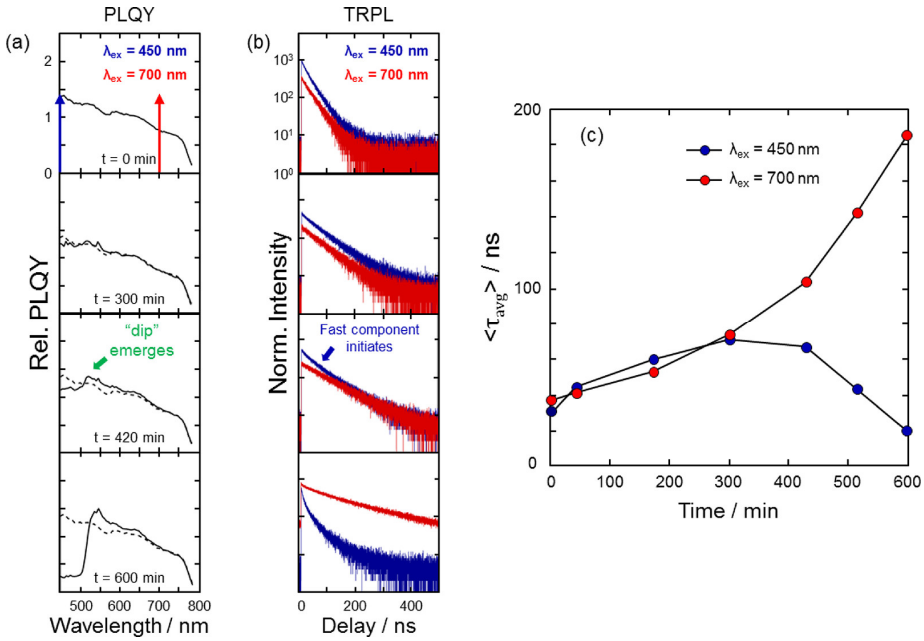

Figure 21. (a) PLE spectra at four instances throughout the 10 h light-soaking experiment. The dashed traces in the bottom three panels represent the PLE at t = 0 min. The vertical scale is the same for all panels. (b) PL decays generated with 450 (blue traces) and 700 nm (red traces) excitation energies at the same time instances as those shown in (a). The vertical scale is the same for all panels. The two excitation wavelengths generating the PL decays in (b) are indicated by blue (450 nm) and red (700 nm) arrows in the top panel of (a). (c) Average lifetimes extracted using stretched exponential fits for both excitation wavelength. Adapted from Paper II.

This study offers a comprehensive insight into the optical characteristics of PbI_2 in $MAPbI_3$ thin films. Employing PLQY and TRPL measurements, we have identified three optical signatures that can be used to determine the presence of PbI_2 in $MAPbI_3$ films: (i) parasitic absorption, (ii) a rapid recombination component in the PL decay, and (iii) a blue shift of PL emission. These features display a dependence on excitation wavelength and the geometry of the sample when PbI_2 is present. Furthermore, these signs are only present when charge carriers are generated in PbI_2 directly. Thus, depending on the configuration of the measurement, one can access information concerning where in the perovskite (sample) PbI_2 is mostly found or begins forming (i.e., at the top or the bottom surface of the film).

4.3 Paper III - Utilizing PLQY Portrait Method on $MAPI_3$ Films to Examine the Validity of the ABC and SRH Models

In this paper, we employ the novel approach for mapping the PLQY described in section 2.1.3 on a set of $MAPI_3$ thin films and try to fit both PLQY portraits and PL decays to validate the ABC and SRH recombination models (Figure 22). Typically, these models are used to semi-quantitatively explain experimental results and derive various rate constants[21,22,53,59–61], often without necessarily taking into account their limitations.

There have been very few attempts to fit both the PL decay and PLQY dependencies of excitation power using ABC/SRH-based models or at least compare the experimental data with theory.[21,23,53,54] However, these methods had limited success due to the frequent existence of huge disparities between experimental data and theoretical fits. Any model of charge carrier dynamics that is believed to be accurate must be able to account for not only typical one-dimensional PLQY(W) data, but also the entire PLQY(f,P) map and PL decays at varied powers and pulse repetition rates.

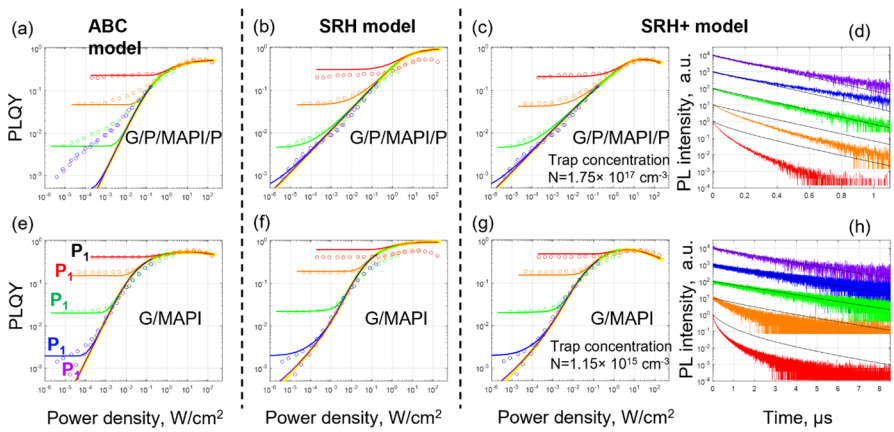

Figure 22. (a) ABC, (b)SRH, (c) SRH+ models applied to the $MAPbI_3$ film and (e) ABC, f (SRH), (g) SRH+ models applied to the $MAPbI_3$ film with PMMA interfaces (G/P/MAPI/P - $MAPbI_3$ deposited on PMMA/glass and then coated by PMMA . In PLQY maps the symbols are experimental points, the lines of the same colour are the theoretical curves. (d) and (h) show experimental and theoretical (black lines) PL decays according to the SRH+ model for both samples, laser repetition rate—100 kHz. The pulse fluences are indicated according to the colour scheme shown in (e) in the whole figure. Adapted from Paper III.

Here, we acquire the PLQY maps on a series of high quality $MAPbI_3$ films with different combination of PMMA interfaces. We emphasize that the (f,P) space (laser

repetition rate, pulse fluence) used in this work is extremely large, with f varying from 100 Hz to 80 MHz (6 orders of magnitude) and P varying over 4 orders of magnitude. We show that neither the ABC nor classical SRH model can fit the acquired PLQY maps across the entire excitation parameter space. To tackle this issue, we develop an enhanced SRH model (SRH+) which accounts for Auger recombination and Auger trapping processes and demonstrates that SRH+ is able to describe and quantitatively fit the PLQY maps over the entire range of excitation conditions with excellent accuracy (Figure 22c,g). PL decays can be also fitted, albeit, with more moderate accuracy (Figure 22d,h).

One possible explanation for the mismatch of the decay rates at high excitation powers might be provided by considering experimental errors. It is well documented that the PL of MHP samples is sensitive to both illumination and environmental conditions, which, may lead to both photodarkening or photobrightening of the sample's PL[27,62–64].

Despite achieving only moderate success at high charge concentrations levels, the outcomes of the SRH+ fitting still represent a substantial improvement over all prior attempts to explain charge carrier dynamics in $MAPbI_3$ samples and allowed us to gain invaluable insights regarding the photophysics of the samples investigated herein and the roles of traps within them.

Upon analysing PLQY maps, it was determined that the concentration of dominant traps within high-quality $MAPbI_3$ approximates $\sim 1.2 \times 10^{15}$ cm^{-3}. Notably, very recent studies using impedance spectroscopy and deep-level transient spectroscopy on $MAPbI_3$ samples prepared using the exact same method yielded nearly identical trap concentration values.[65] This concurrence also aligns remarkably well with the range of values previously proposed by Stranks et al.[21]

An ongoing debate within the perovskite community centres on the impact of defects on charge carrier dynamics in perovskite films. While some studies argue that these defects, often located at grain boundaries, have no significant influence on charge recombination,[66,67] others contend that such defects do affect the optoelectronic quality of the perovskite layer.[68,69] Given these conflicting findings, it becomes evident that traditional PLQY measurements fall short in discerning the role of defects.

We believe that the PLQY(f,P) map represents the most informative signature of a sample concerning its charge recombination pathways and has the potential to help resolve this and other unresolved questions in the field. We anticipate that this non-invasive and straightforward method will have practical applications in the control and optimization of semiconducting materials and the devices built upon them.

4.4 Paper IV - Fast Defect Kinetics in Non-Stoichiometric Hybrid Perovskite ($MAPbI_3$) Films

In this paper we investigate the changes in the photoluminescence response of fractionally non-stoichiometric $MAPbI_3$ perovskite films, whereas previous studies have examined the effect of deviations in precursor stoichiometry on device stability and perovskite response in general.[55,70–73] Using the PLQY mapping approach, samples are tracked over a six-week period. The aging research of the stability of the stoichiometrically altered $MAPbI_3$ films reveals that their PL response varies significantly. In these samples, we found the presence of rapid reversible dynamics that are highly repeatable and evolve over time. We also describe how PL measurements are particularly sensitive to photo-excitation and data gathering techniques, which are typically overlooked in the standard PL studies.

The PLQY maps of $MAPbI_3$ film samples with fractionally deviating stoichiometries (Figure 23c,d) differed markedly from that of standard $MAPbI_3$ films (Figure 23a). They exhibit a reduced absolute PLQY across all excitation regimes. They also display an uncharacteristic initial reduction of PLQY in the single pulse regime as f increases (three grey arrows in Figure 23d). Another untypical characteristic appears as a “discontinuity” within the single regime at the highest pulse fluence, highlighted by the double-sided arrows in Figure 23c,d. These last two features have their origin traced back to the observer effect, related to the photosensitivity of the material and the precise details of the sample light exposure controlled by a shutter as previously explained in section 3.3.

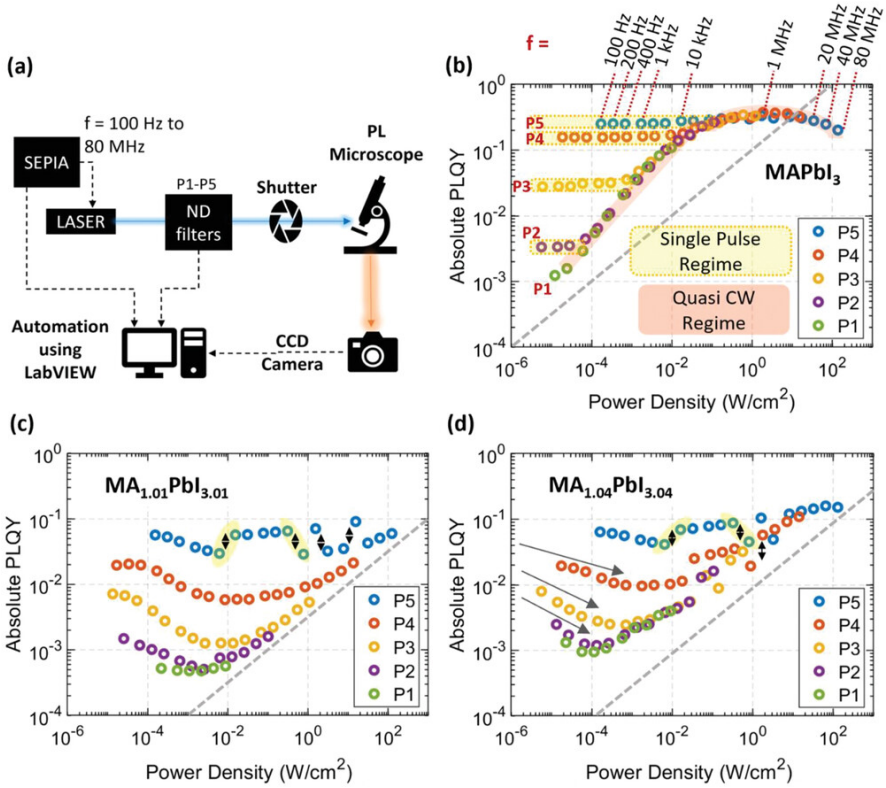

Figure 23. A schematic representation of the setup for acquisition of PLQY(f,P) maps. PLQY maps of b) $MAPbI_3$, c) $MA_{1.04}PbI_{3.04}$, and d) $MA_{1.1}PbI_{3.1}$ films. The map is formed by plotting together a family of 5 curves of PLQY versus Power Density. Each curve is obtained for its own pulse fluence, P_n. P1 is the lowest and P5 is the highest pulse fluence (in photons/cm^2/pulse). The scanning of the laser repetition rate f is illustrated in (b) for pulse fluence P5. See the text for details. The grey dash lines show the square root dependence between the excitation power density and PLQY, which aids to compare the slopes of the quasi-CW-regime of the samples. Different excitation regimes are marked in (b). Adapted from Paper IV.

After identifying the causes of the artifacts in the PLQY maps, we investigate how these maps evolve as the samples undergo storage. It is worth noting that we consistently employed exactly the same data acquisition procedure, enabling direct comparisons between maps of different samples and those of the same samples measured at varying storage durations. Our findings indicate that the artifacts stemming from defect dynamics in over-stoichiometric samples diminish as the films age (Figure 24).

As evidenced by the PLQY maps, PLQY increases with the aging of the samples, and the abrupt jumps caused by fast dynamics at high excitation power also decrease. While the PLQY map for the sample aged six weeks still exhibits artifacts, such as non-constant PLQY in the single-pulse regime, it has significantly converged with the reference stoichiometric MAPI (as compared to Figure 23b).

This substantial shift in PL response signifies a healing process occurring within the sample. We propose that the excessive iodide within the crystal structure (inherent to over-stoichiometric samples), initially migrates to the surface of the grains and subsequently departs from the surface over time, particularly upon exposure to oxygen and light illumination. This process aligns with the discussion presented by Goetz et al[74], where the healing of an over-stoichiometric MAPI film was observed following deliberate photo-oxidation.

The evolution of the PLQY maps for the considerably over-stoichiometric $MA_{1.1}PbI_{3.1}$ is illustrated in the lower row of Figure 24. While the PLQY values exhibit a slight increase with the sample's aging, the anomalies stemming from rapid light-induced defect dynamics persist at the same level. This indicates that when the extent of over-stoichiometry surpasses a certain threshold, the sample does not naturally revert to its standard state over time. Even after an extended period of storage, it maintains charge carrier and defect dynamics significantly distinct from those of the stoichiometric MAPI film.

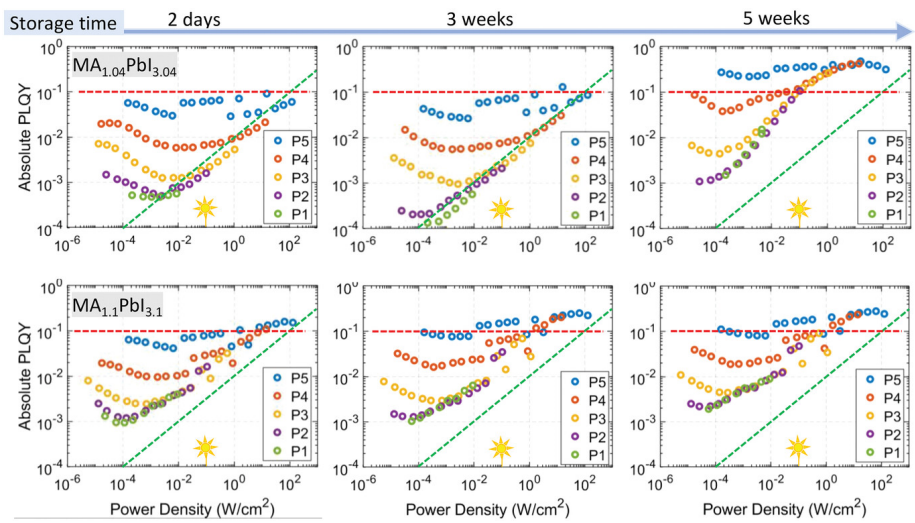

Figure 24. A series of PLQY(f,P) maps demonstrating the evolution of the response of the non-stoichiometric MAPI films as a function of the storage time after synthesis. Top raw—the slightly over-stoichiometric $MA_{1.04}PbI_{3.04}$, bottom raw—the significantly over-stoichiometric $MA_{1.1}PbI_{3.1}$ films. Red horizontal dash line shows PLQY = 10%, the tilted green dash line is the square root dependence (slope 0.5 in log-log scale) expected for the quasi-CW regime for the case of photodoping without trap saturation. These lines aid comparison of the plots between each other. The "sun" marks the excitation power density of 0.1 W cm^{-2}. Adapted from Paper IV.

There still remains a lack of comprehensive understanding regarding the specific defects responsible for the apparent photosensitivity observed in MAPI by researchers. Previous studies suggests that iodide interstitials, which naturally occur

at significant levels in over-stoichiometric samples, are, to some extent, a contributing factor[26,27,75,76]. In these over-stoichiometric samples, there is also an excess of MA^+ counter ions. However, it is generally understood that these excess MA^+ ions play a far less significant role in non-radiative recombination processes.[65]

Due to the automated experimental process and the distinctive mapping across extensive parameter space encompassing f and P, we can promptly recognize certain samples displaying atypical characteristics. These samples should be approached cautiously for analysis, particularly in the light of their photosensitivity. In a strict sense, for materials featuring photosensitive defect concentrations, conventional spectroscopic techniques and established theoretical models may not be entirely suitable or reliable for comprehensive analysis.

Chapter 5 Conclusions

The findings presented in Paper I highlight the successful utilization of PLE microscopy for real-time monitoring of spatially resolved photodegradation in $MAPbI_3$ thin films. Notably, the emergence of discernible photoluminescence flickering withing the samples is prominently associated with the degradation process and the subsequent formation of PbI_2. Additionally, our study reveals a significant correlation between the intensity of observed PL flickering and the excitation wavelength used.

In Paper II we utilize PLQY and TRPL measurements to successfully identify three distinct optical markers that serve to indicate the presence of PbI_2 within $MAPbI_3$ films. These characteristics exhibit variations based on the excitation wavelength and sample geometry, specifically in cases where PbI_2 is detected. Consequently, depending on the measurement configuration, researchers can access valuable insights into the specific location of PbI_2 within the perovskite film-providing insights into whether it is primarily concentrated at the film's top or bottom surface, or where its formation initiates.

In Papers III and IV we introduced and applied a novel experimental methodology, incorporating PL measurements within a two-dimensional parameter space of laser pulse excitation fluence and pulse repetition frequency. These maps allow for distinction between single-pulse and quasi-continuous excitation regimes and provide a useful tool for examining the validity of commonly employed and future kinetic models of charge recombination. This approach has further revealed distinct features (fingerprints) withing the PLQY maps that enable clear differentiation between samples and by their electronic properties.

In conclusion, perovskite metal halides hold immense promise as a class of materials with remarkable optoelectronic properties, making them attractive candidates for various technological applications. However, the pursuit of harnessing their potential is not without its challenges. We show the necessity of designing meticulous experiments, implementing advanced measurement techniques, and adopting controlled environments in order to mitigate the observer effect's impact. Moreover, since experimental results on MHP's are strongly influenced on synthesis methods, environmental condition, and measurement protocols, interdisciplinary collaborations and standardized practices become essential to ensure the reproducibility and reliability of results across different research groups.

References

1. Jena, A. K., Kulkarni, A. & Miyasaka, T. Halide Perovskite Photovoltaics: Background, Status, and Future Prospects. *Chem Rev* **119**, 3036–3103 (2019).
2. Schmidt-Mende, L. *et al.* Roadmap on organic–inorganic hybrid perovskite semiconductors and devices. *APL Mater* **9**, 109202 (2021).
3. Dong, H., Zhang, C., Liu, X., Yao, J. & Zhao, Y. S. Materials chemistry and engineering in metal halide perovskite lasers. *Chem Soc Rev* **49**, 951–982 (2020).
4. Xie, C., Liu, C.-K., Loi, H.-L. & Yan, F. Perovskite-Based Phototransistors and Hybrid Photodetectors. *Adv Funct Mater* **30**, 1903907 (2020).
5. Park, N.-G. Perovskite solar cells: an emerging photovoltaic technology. *Materials Today* **18**, 65–72 (2015).
6. Faridi, A. W. *et al.* Synthesis and Characterization of High-Efficiency Halide Perovskite Nanomaterials for Light-Absorbing Applications. *Ind Eng Chem Res* **62**, 4494–4502 (2023).
7. Agbaoye, R. O., Akinlami, J. O., Afolabi, T. A. & Adebayo, G. A. Unraveling the Stable Phase, High Absorption Coefficient, Optical and Mechanical Properties of Hybrid Perovskite CH3NH3PbxMg1–xI3: Density Functional Approach. *J Inorg Organomet Polym Mater* **30**, 299–309 (2020).
8. Tablero Crespo, C. Absorption coefficients data of lead iodine perovskites using 14 different organic cations. *Data Brief* **27**, 104636 (2019).
9. Habibi, M., Zabihi, F., Ahmadian-Yazdi, M.-R. & Eslamian, M. Progress in emerging solution-processed thin film solar cells – Part II :Perovskite solar cells. *RenewableandSustainableEnergyReviews* **62**, 10–12 (2016).
10. Kulkarni, S. A. *et al.* Band-gap tuning of lead halide perovskites using a sequential deposition process. *J Mater Chem A Mater* **2**, 9221–9225 (2014).
11. Ou, Q. *et al.* Band structure engineering in metal halide perovskite nanostructures for optoelectronic applications. *Nano Materials Science* **1**, (2019).

12. Ju, D. *et al.* Tunable Band Gap and Long Carrier Recombination Lifetime of Stable Mixed CH3NH3PbxSn1–xBr3 Single Crystals. *Chemistry of Materials* **30**, 1556–1565 (2018).

13. Kojima, A., Teshima, K., Shirai, Y. & Miyasaka, T. Organometal halide perovskites as visible-light sensitizers for photovoltaic cells. *J Am Chem Soc* **131**, 6050–6051 (2009).

14. Best Research-Cell Efficiency Chart | Photovoltaic Research | NREL. https://www.nrel.gov/pv/cell-efficiency.html.

15. Shockley, W. & Read, W. T. Statistics of the Recombinations of Holes and Electrons. *Physical Review* **87**, 835–842 (1952).

16. Hall, R. N. Electron-Hole Recombination in Germanium. *Physical Review* **87**, 387 (1952).

17. Shen, Y. C. *et al.* Auger recombination in InGaN measured by photoluminescence. *Appl Phys Lett* **91**, 141101 (2007).

18. Gerhard, M. *et al.* Microscopic insight into non-radiative decay in perovskite semiconductors from temperature-dependent luminescence blinking. *Nat Commun* **10**, 1698 (2019).

19. Dobrovolsky, A., Merdasa, A., Unger, E. L., Yartsev, A. & Scheblykin, I. G. Defect-induced local variation of crystal phase transition temperature in metal-halide perovskites. *Nat Commun* **8**, 34 (2017).

20. Wright, A. D. *et al.* Electron–phonon coupling in hybrid lead halide perovskites. *Nat Commun* **7**, 11755 (2016).

21. Stranks, S. D. *et al.* Recombination Kinetics in Organic-Inorganic Perovskites: Excitons, Free Charge, and Subgap States. *Phys Rev Appl* **2**, 34007 (2014).

22. Johnston, M. B. & Herz, L. M. Hybrid Perovskites for Photovoltaics: Charge-Carrier Recombination, Diffusion, and Radiative Efficiencies. *Acc Chem Res* **49**, 146–154 (2016).

23. Manger, L. H. *et al.* Global Analysis of Perovskite Photophysics Reveals Importance of Geminate Pathways. *The Journal of Physical Chemistry C* **121**, 1062–1071 (2017).

24. Stolterfoht, M. *et al.* Voltage-Dependent Photoluminescence and How It Correlates with the Fill Factor and Open-Circuit Voltage in Perovskite Solar Cells. *ACS Energy Lett* **4**, 2887–2892 (2019).

25. Seth, S. *et al.* Presence of Maximal Characteristic Time in Photoluminescence Blinking of MAPbI3 Perovskite. *Adv Energy Mater* **11**, 2102449 (2021).

26. Motti, S. G. *et al.* Controlling competing photochemical reactions stabilizes perovskite solar cells. *Nat Photonics* **13**, 532–539 (2019).

27. Motti, S. G. *et al.* Defect Activity in Lead Halide Perovskites. *Advanced Materials* **31**, 1901183 (2019).

28. Galle, M. H. J. J., Li, J., Frantsuzov, P. A., Basché, T. & Scheblykin, I. G. Self-Healing Ability of Perovskites Observed via Photoluminescence Response on Nanoscale Local Forces and Mechanical Damage. *Advanced Science* **10**, 2204393 (2023).

29. Merdasa, A. *et al.* "Supertrap" at Work: Extremely Efficient Nonradiative Recombination Channels in MAPbI3 Perovskites Revealed by Luminescence Super-Resolution Imaging and Spectroscopy. *ACS Nano* **11**, 5391–5404 (2017).

30. Domanski, K. *et al.* Migration of cations induces reversible performance losses over day/night cycling in perovskite solar cells. *Energy Environ Sci* **10**, 604–613 (2017).

31. Ceratti, D. R. *et al.* Self-Healing and Light-Soaking in MAPbI3: The Effect of H2O. *Advanced Materials* **34**, 2110239 (2022).

32. Cahen, D. & Lubomirsky, I. Self-Repairing Energy Materials: Sine Qua Non for a Sustainable Future. *Acc Chem Res* **50**, 573–576 (2017).

33. Misra, R. K. *et al.* Temperature- and Component-Dependent Degradation of Perovskite Photovoltaic Materials under Concentrated Sunlight. *J Phys Chem Lett* **6**, 326–330 (2015).

34. Yang, J., Siempelkamp, B. D., Liu, D. & Kelly, T. L. Investigation of CH3NH3PbI3 Degradation Rates and Mechanisms in Controlled Humidity Environments Using in Situ Techniques. *ACS Nano* **9**, 1955–1963 (2015).

35. Purev-Ochir, B. *et al.* Oxygen-Induced Reversible Degradation of Perovskite Solar Cells. *Solar RRL* **7**, 2300127 (2023).

36. Senocrate, A. *et al.* Interaction of oxygen with halide perovskites. *J Mater Chem A Mater* **6**, 10847–10855 (2018).

37. Zheng, D. G. & Kim, D. H. Degradation mechanisms of perovskite light-emitting diodes under electrical bias. **12**, 451–476 (2023).

38. Sassoli de Bianchi, M. The Observer Effect. *Found Sci* **18**, 213–243 (2013).

39. Baclawski, K. The Observer Effect. in *2018 IEEE Conference on Cognitive and Computational Aspects of Situation Management (CogSIMA)* 83–89 (2018). doi:10.1109/COGSIMA.2018.8423983.

40. Young, T. II. The Bakerian Lecture. On the theory of light and colours. *Philos Trans R Soc Lond* **92**, 12–48 (1997).

41. Howie, A., Ffowcs Williams, J. E., Howie, A. & Ffowcs Williams, J. E. Preface. *Philosophical Transactions of the Royal Society of London. Series A: Mathematical, Physical and Engineering Sciences* **360**, 805–806 (2002).

42. Shi, J. *et al.* All-optical fluorescence blinking control in quantum dots with ultrafast mid-infrared pulses. *Nat Nanotechnol* **16**, 1355–1361 (2021).

43. Galland, C. *et al.* Two types of luminescence blinking revealed by spectroelectrochemistry of single quantum dots. *Nature* **479**, 203–207 (2011).

44. Frantsuzov, P. A. & Marcus, R. A. Explanation of quantum dot blinking without the long-lived trap hypothesis. *Phys Rev B* **72**, 155321 (2005).

45. Lelek, M. *et al.* Single-molecule localization microscopy. *Nature Reviews Methods Primers* **1**, 39 (2021).

46. Chien, F.-C., Lin, C.-Y. & Abrigo, G. Single-Molecule Blinking Fluorescence Enhancement by Surface Plasmon-Coupled Emission-Based Substrates for Single-Molecule Localization Imaging. *Anal Chem* **93**, 15401–15411 (2021).

47. Püntener, S. & Rivera-Fuentes, P. Single-Molecule Peptide Identification Using Fluorescence Blinking Fingerprints. *J Am Chem Soc* **145**, 1441–1447 (2023).

48. Gerhard, M. *et al.* Heterogeneities and Emissive Defects in MAPbI3 Perovskite Revealed by Spectrally Resolved Luminescence Blinking. *Adv Opt Mater* **9**, 2001380 (2021).

49. Pathoor, N. *et al.* Fluorescence Blinking Beyond Nanoconfinement: Spatially Synchronous Intermittency of Entire Perovskite Microcrystals. *Angewandte Chemie International Edition* **57**, 11603–11607 (2018).

50. Pathoor, N. & Chowdhury, A. Spatially Correlated Blinking of Perovskite Micro-crystals: Deciphering Effective Modes of Communication between Distal Photoexcited Carriers. *ACS Photonics* **10**, (2022).

51. Halder, A., Pathoor, N., Chowdhury, A. & Sarkar, S. Photoluminescence Flickering of Micron Sized Crystals of Methylammonium Lead Bromide:

Effect of Ambience and Light Exposure. *The Journal of Physical Chemistry C* **122**, (2018).

52. Eremchev, I. Yu., Tarasevich, A. O., Li, J., Naumov, A. V & Scheblykin, I. G. Lack of Photon Antibunching Supports Supertrap Model of Photoluminescence Blinking in Perovskite Sub-Micrometer Crystals. *Adv Opt Mater* **9**, 2001596 (2021).

53. Saba, M. *et al.* Correlated electron-hole plasma in organometal perovskites. *Nat Commun* **5**, (2014).

54. Trimpl, M. J. *et al.* Charge-Carrier Trapping and Radiative Recombination in Metal Halide Perovskite Semiconductors. *Adv Funct Mater* **30**, (2020).

55. Goetz, K. P. & Vaynzof, Y. The Challenge of Making the Same Device Twice in Perovskite Photovoltaics. *ACS Energy Lett* **7**, 1750–1757 (2022).

56. Merdasa, A. *et al.* Impact of Excess Lead Iodide on the Recombination Kinetics in Metal Halide Perovskites. *ACS Energy Lett* **4**, 1370-1378 (2019).

57. Yang, J., Siempelkamp, B. D., Liu, D. & Kelly, T. L. Investigation of CH3NH3PbI3 Degradation Rates and Mechanisms in Controlled Humidity Environments Using in Situ Techniques. *ACS Nano* **9**, 1955–1963 (2015).

58. Melvin, A. A. *et al.* Lead iodide as a buffer layer in UV-induced degradation of CH3NH3PbI3 films. *Solar Energy* **159**, 794–799 (2018).

59. Feldmann, S. *et al.* Photodoping through local charge carrier accumulation in alloyed hybrid perovskites for highly efficient luminescence. *Nat Photonics* **14**, 123–128 (2020).

60. DeQuilettes, D. W. *et al.* Tracking Photoexcited Carriers in Hybrid Perovskite Semiconductors: Trap-Dominated Spatial Heterogeneity and Diffusion. *ACS Nano* **11**, 11488–11496 (2017).

61. Kang, G. *et al.* Electron trapping and extraction kinetics on carrier diffusion in metal halide perovskite thin films. *J Mater Chem A Mater* **7**, 25838–25844 (2019).

62. Tian, Y. *et al.* Mechanistic insights into perovskite photoluminescence enhancement: Light curing with oxygen can boost yield thousandfold. *Physical Chemistry Chemical Physics* **17**, 24978–24987 (2015).

63. Andaji-Garmaroudi, Z., Anaya, M., Pearson, A. J. & Stranks, S. D. Photobrightening in Lead Halide Perovskites: Observations, Mechanisms, and Future Potential. *Adv Energy Mater* **10**, (2020).

64. Fassl, P. *et al.* Fractional deviations in precursor stoichiometry dictate the properties, performance and stability of perovskite photovoltaic devices. *Energy Environ Sci* **11**, 3380–3391 (2018).

65. Reichert, S. *et al.* Probing the ionic defect landscape in halide perovskite solar cells. *Nat Commun* **11**, (2020).

66. Yang, M. *et al.* Do grain boundaries dominate non-radiative recombination in CH3NH3PbI3 perovskite thin films? *Physical Chemistry Chemical Physics* **19**, 5043–5050 (2017).

67. Yin, W. J., Shi, T. & Yan, Y. Unique properties of halide perovskites as possible origins of the superior solar cell performance. *Advanced Materials* **26**, 4653–4658 (2014).

68. Xu, W. *et al.* Precisely Controlling the Grain Sizes with an Ammonium Hypophosphite Additive for High-Performance Perovskite Solar Cells. *Adv Funct Mater* **28**, (2018).

69. Ren, X. *et al.* Modulating crystal grain size and optoelectronic properties of perovskite films for solar cells by reaction temperature. *Nanoscale* **8**, 3816–3822 (2016).

70. Taylor, A. D. *et al.* A general approach to high-efficiency perovskite solar cells by any antisolvent. *Nat Commun* **12**, 1878 (2021).

71. Odabaşı, Ç. & Yıldırım, R. Assessment of Reproducibility, Hysteresis, and Stability Relations in Perovskite Solar Cells Using Machine Learning. *Energy Technology* **8**, 1901449 (2020).

72. Jamal, M. S. *et al.* Fabrication techniques and morphological analysis of perovskite absorber layer for high-efficiency perovskite solar cell: A review. *Renewable and Sustainable Energy Reviews* **98**, 469–488 (2018).

73. Chen, Z. *et al.* Processing and Preparation Method for High-Quality Opto-Electronic Perovskite Film. *Front Mater* **8**, (2021).

74. Goetz, K. P. *et al.* Remarkable performance recovery in highly defective perovskite solar cells by photo-oxidation. *J Mater Chem C Mater* **11**, 8007–8017 (2023).

75. DeQuilettes, D. W. *et al.* Photo-induced halide redistribution in organic-inorganic perovskite films. *Nat Commun* **7**, (2016).

76. Fassl, P. *et al.* Effect of density of surface defects on photoluminescence properties in MAPbI3 perovskite films. *J Mater Chem C Mater* **7**, 5285–5292 (2019).

Paper I

Journal of Luminescence 222 (2020) 117129

Contents lists available at ScienceDirect

Journal of Luminescence

journal homepage: http://www.elsevier.com/locate/jlumin

Excitation wavelength dependence of photoluminescence flickering in degraded $MAPbI_3$ perovskite and its connection to lead iodide formation

Alexander Kiligaridis [a], Aboma Merdasa [b], Carolin Rehermann [b], Eva L. Unger [a,b], Ivan G. Scheblykin [a,*]

[a] Chemical Physics and NanoLund, Lund University, P.O. Box 124, 22100, Lund, Sweden
[b] Young Investigator Group Hybrid Materials Formation and Scaling, Helmholtz-Zentrum Berlin für Materialen und Energie GmbH, Albert-Einstein Strasse 16, 12489, Berlin, Germany

ARTICLE INFO

Keywords:
Perovskite
Photoluminescence
Blinking
Degradation
Lead iodide
Luminescence excitation spectrum

ABSTRACT

Metal halide perovskite semiconductors often exhibit photoluminescence blinking and flickering when luminescence of individual small nano- or even microcrystals is monitored. The nature of these fluctuations is not well understood but must be related to the presence of metastable non-radiative recombination channels and efficient charge migration in these materials. Here we report on the excitation wavelength dependence of photoluminescence flickering effect in degraded methylammonium lead iodide ($MAPbI_3$) thin films. While the luminescence intensity is temporary stable when excited in the blue region with wavelength shorter than 530 nm, excitation with red light (wavelength longer than 530 nm) results in luminescence flickering. It is hypothesised that the wavelength dependence reflects the excitation energy dependence of the photochemical mechanism that switches non-radiative recombination channels on and off. The effect can also be related to hindered charge carrier diffusion due to their localization in the interfacial layer between $MAPbI_3$ and PbI_2 which is formed in the course of degradation.

1. Introduction

Metal Halide Perovskite (MHPs) semiconductors of impressive crystallinity and opto-electronic quality can be obtained by solution processing at low temperature. This feature has enabled swift progress in obtained performance in opto-electronic devices as deposition processes are easy to implement and many groups world-wide are involved [1]. Despite very impressive efficiencies of perovskite solar cells exceeding 20%, understanding of many optical and electronic properties of these materials is still elusive and often speculative [2,3]. Rationalization of this new class of semiconductors by developing predictive physical models has been proven challenging because of the material itself often exhibiting low stability. Opto-electronic properties have been demonstrated to change due to exposure to light or heat, sensitivity to ambient species such as moisture and oxygen, and the co-existence of crystalline impurity phases and degradation products. A growing body of literature shows that defects and their time dependent evolution on scales from microseconds to hours play a key role in these instabilities [4–10].

Several light-induced transient phenomena have been reported affecting the photoluminescence (PL). PL enhancement was observed to occur upon prolonged light exposure when PL yield of a sample can grow several orders of magnitude under 1 Sun (0.1 W/cm^2) light irradiation [4,11,12]. The PL has also been found to decline under light exposure [13,14] indicating photo-degradative phenomena. In addition, blinking or rather flickering of the PL intensity of individual crystalline objects of sizes beyond quantum confinement (50–1000 nm) has been observed [15–19] which has been hypothesised to originate from a reversible on/off switching of a strong non-radiative centre (a super-trap) [16]. All these phenomena show that concentration of non-radiative recombination centres or rather the balance between radiative and non-radiative charge recombination can change over time. It steadily decreases/increases in the case of PL enhancement/degradation while it randomly fluctuates in the case of PL blinking/flickering. Note that the explanation of the origin of the PL fluctuations based on the idea of a super-trap is conceptually the same as the so-called multiple recombination centres (MRC) model[20] suggested for quantum dots. Currently both MRC model and the Auger recombination mechanism are used for explanation of blinking of semiconductor

* Corresponding author.
E-mail address: ivan.scheblykin@chemphys.lu.se (I.G. Scheblykin).

https://doi.org/10.1016/j.jlumin.2020.117129
Received 30 August 2019; Received in revised form 1 February 2020; Accepted 14 February 2020
Available online 24 February 2020
0022-2313/© 2020 Elsevier B.V. All rights reserved.

(including perovskites) quantum dots [21–24]. However, we do not think that Auger recombination is responsible for the PL flickering of large perovskites crystals simply because of too low charge concentration reached under the excitation conditions when flickering is observed, as discussed elsewhere [16]. Note, however, that there might be no difference in the chemistry of the metastable non-radiative recombination centres for QDs and large crystals of the same material.

The dynamic nature of the defects in MHP has been linked to a relatively small activation energy for ion migration[25], redox chemistry of halogens [26], permittivity of the material to gases [4,27] and small molecules. The possibility of structural variations due to migrating ions and ion vacancies, as well as their interaction with gaseous species, are likely causes both for material degradation as well as "self-healing" phenomena [28]. Pinpointing exact nature and concentration of defects is intricate due to their transient nature [29].

The simplest view on degradation is that it occurs when something in the ABX3 perovskite structure is removed or replaced. Lead-based perovskites typically degrade via the decomposition into PbI_2. The first step in the structural degradation of ABX_3 perovskites is the loss or replacement of a constituent ion. In methylammonium-based perovskites, the loss of methylammonium or, after deprotonation[30], the loss of methylamine removes the central cation stabilizing the cubic perovskite structure which causes structural collapse. Lead iodide is often observed as the degradation product[31], often detected by its characteristic absorption onset around 2.4 eV or green PL emission. Using photoluminescence excitation (PLE) spectroscopy we recently reported the observation of a distinctive feature in the PLE spectrum evolving due to the formation of a PbI_2 layer on top of $MAPbI_3$ upon photo-degradation [32]. PLE and PL microscopy can further be used to study the spatial evolution of perovskite degradation to PbI_2.

PL blinking phenomenon has often been regarded as an indication of the first step of metal-halide perovskite degradation [33]. However, PL blinking is still a reversible process. In perovskites, it has been related to a reversible formation and annihilation of very efficient non-radiative recombination centres [15,19]. There is, however, an on-going debate on the origin of the "on-off" switching of these centres [19]. In spite of clear evidences that e.g. humidity induces PL blinking[33], blinking is also observed at high vacuum conditions and at low temperature [19]. This would suggest that these recombination centres are intrinsic to the material itself and can exhibit different characteristics depending on the particular sample under investigation and environment during experimentation.

In this work we employ PLE microscopy, exciting samples in the spectral range from 450 nm to 700 nm, to monitor the spatially resolved photo-degradation of methylammonium lead iodide ($MAPbI_3$) thin films. We find that grains having undergone partial degradation to PbI_2 possess a much more pronounced PL flickering than grains of non-degraded $MAPbI_3$. Moreover, we observe that PL flickering depends on the excitation wavelength becoming stronger for low energy ($\lambda >$ 530 nm) excitation. Possible origins of this effect will be discussed.

2. Experimental

All precursor materials were purchased from Sigma-Aldrich, TCI or Greatcell Solar Ltd and were used as received. All preparations were done under inert atmosphere. 1 M stock solutions of MAI and PbI_2 in pure N,N-dimethylformamide (DMF) were prepared and mixed in ratio 1:1.1 excess of PbI_2. The solution was spin-coated on top of a clean cover slip glass substrate at 4000 rpm for 30 s (accel. of 4000 rpm s^{-1}) and annealed at 100 °C for 15 min. Before deposition, the glass substrate was cleaned by sonication in mucasol, acetone and isopropanol successively and treated in O_3 plasma.

All measurements were carried out in a home-built PL excitation/emission microscopy setup (Fig. 1) [32]. A narrow (<1 nm) tuneable excitation beam is obtained by combining a supercontinuum laser (SuperK Extreme, NKT Photonics) and a mechanically rotating diffraction grating. The selected excitation wavelength illuminates the sample through an objective lens (Olympus LUCPlanFL 40×, NA = 0.6) and the PL emitted by the sample is collected by the same objective and detected by a CCD camera (Princeton ProEM 512B). The result is a wide-field PL image with diffraction limited resolution. Tuneable long-pass and short-pass filters (3G LVLWP/LVSWP, Delta Optical Thin Film) operate

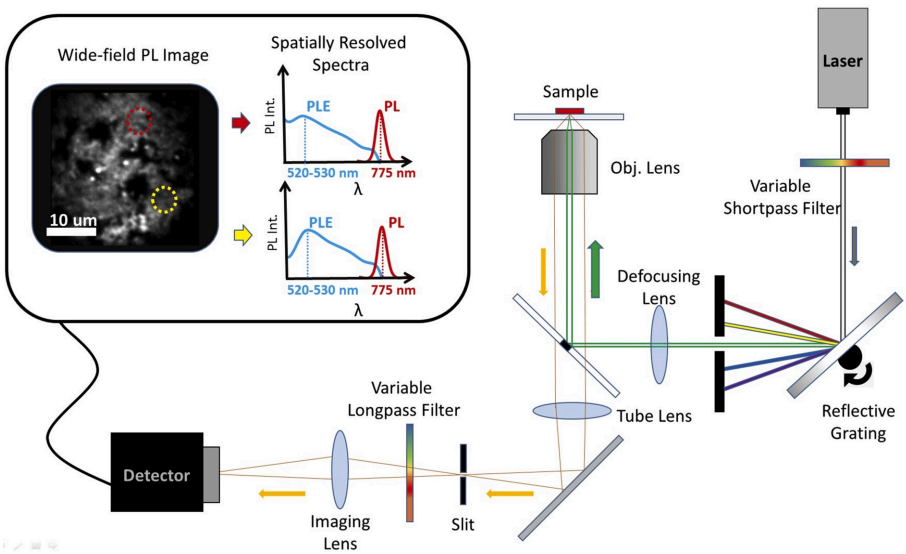

Fig. 1. Schematic of photoluminescence excitation/emission microscopy setup. Inserts illustrate $MAPbI_3$ photoluminescence excitation and emission spectra.

in conjunction to greatly supress (OD > 5) the excitation light before detection and provide single molecule/nanocrystal sensitivity. Illuminating the sample over a range of excitation wavelengths, following the necessary excitation power calibration, a series of PL images are obtained containing all required data to construct spatially resolved excitation spectra of different regions of the sample.

In these measurements we exposed the $MAPbI_3$ film to local illumination (approximately Gaussian spot profile with diameter ca. 30 μm) with a quasi CW light (pulsed at 78 MHz) of about 1 Sun power density which was continuously scanned from 450 to 700 nm at steps of 5 nm for 1.5 h (total of 90 scans) at ambient conditions. The same excitation light acted as a tool to probe the PL while simultaneously inducing photo degradation, thus allowing for in-situ monitoring of any changes to the PL excitation spectrum that could indicate degradation onset. PL intensity transients after photodegradation were obtained by CCD camera with exposure time of 50 ms per frame while keeping the excitation wavelength constant for 400 frames.

3. Results

Fig. 2a–c shows the evolution of the PL image upon photo degradation. Due to the power density distribution within the laser spot, the degradation was faster in the central region and much slower at the edges (region 2 in Fig. 2c, also see the video in SI). After 1.5 h of illumination most of the film close to the centre of the excitation spot lost its PL and was to a large extent converted to PbI_2. The presence of PbI_2 was also verified by its characteristic yellow colouring in transmission. Furthermore, the regions which still possessed strong PL (region 3 in Fig. 2c) showed a characteristic PLE spectrum (Fig. 2d) previously assigned to formation of PbI_2 on the top of $MAPbI_3$ [32].

Supplementary video related to this article can be found at https://doi.org/10.1016/j.jlumin.2020.117129.

The most interesting observation was that, the regions of the sample which were visibly affected by photodegradation but still showed luminescence typical for $MAPbI_3$ (partial degradation, region 3), exhibited a significantly stronger PL intensity flickering than less degraded regions of the film (region 2), compare Fig. 3b and Fig. 3d. In addition, we found that the PL flickering effect is excitation wavelength dependent. Namely, much stronger fluctuations were observed for $\lambda_{exc} > 530$ nm as can be seen by comparing the different panels in Fig. 3d and in the video in SI. Note that no enhanced PL flickering under low-energy excitation was observed in region 2 which was only slightly affected by photodegradation (Fig. 3b).

4. Discussion

The general increase of PL fluctuations upon degradation shows that formation of switchable super-traps is related to degradation of the material [33]. This is not too surprising since degradation is an accumulation of different defects in the material and the PL flickering phenomenon is related to this process.

The current model of the PL blinking effect in MHP semiconductors is

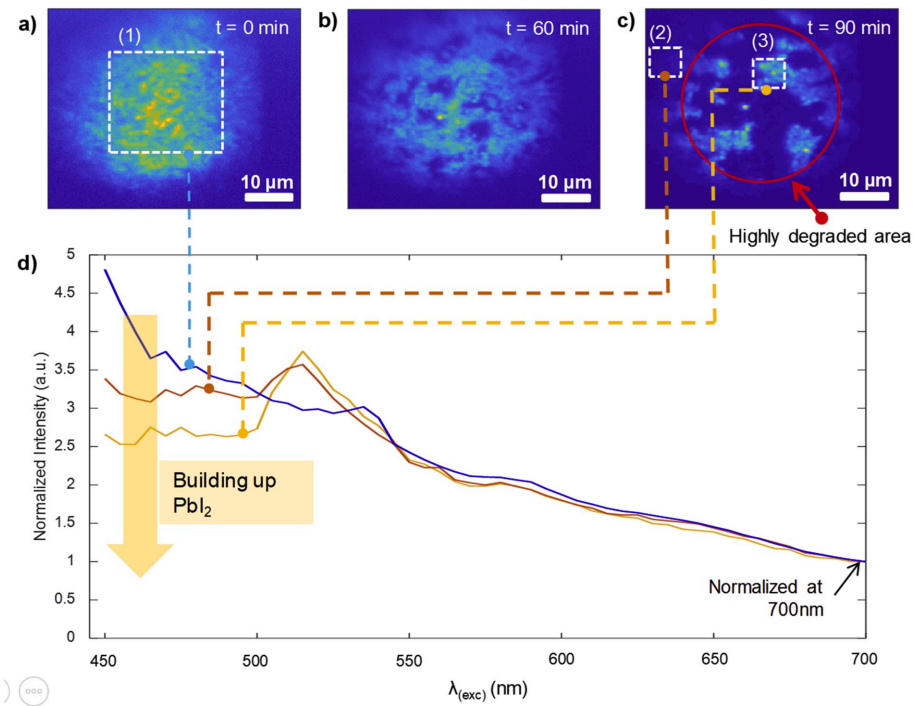

Fig. 2. Wide-field photoluminescence images of the same area of a $MAPbI_3$ film after (a) t = 0 (fresh film), (b) t = 60 min and (c) t = 90 min of 1 Sun illumination at ambient conditions. The PL intensity distribution in the fresh film reflects the laser excitation spot profile. (d) Photoluminescence excitation (PLE) spectra at different conditions: blue line - PLE of the fresh film, collected from region (1), orange line – PLE of a slightly degraded region (2), yellow line – PLE of the luminescence coming from region (3) in the highly degraded area. All PLE spectra are normalized at 700 nm.

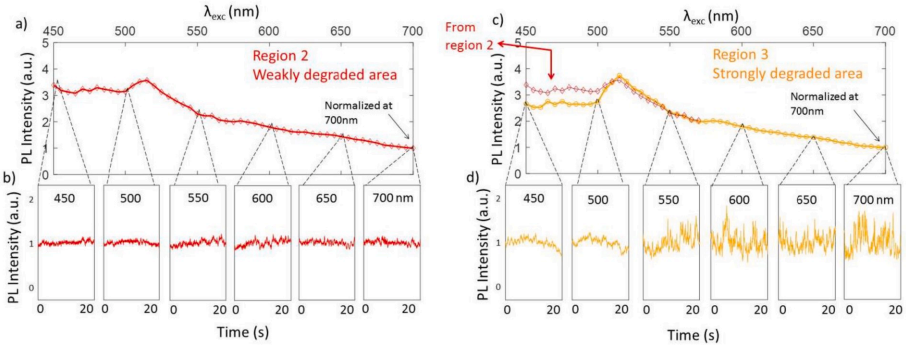

Fig. 3. Photoluminescence excitation spectra of regions 2 (panel a)) and 3 (panel c)), see Fig. 2c for the PL image. b), d) - photoluminescence intensity time traces of regions 2 and 3 measured under different excitation wavelengths from 450 to 700 nm with steps of 50 nm. The excitation wavelength is indicated on each graph. Graphs in d) for $\lambda_{exc} \geq 550$ nm show strong PL intensity flickering. Also, see the video in SI for clarity.

based on the idea that the PL intensity of a micro/nano crystal or a small local region of a MHP film can be changed substantially by activation/deactivation of just one very efficient non-radiative (NR) recombination centre, which we previously referred to as "super-trap" [15,16,19]. The ability of one super-trap to quench PL of a crystal as large as hundreds of nm in size (or, in other words, very large charge recombination cross section of the super trap) originates from a long charge carriers diffusion length (»100 nm) [34] and the fast (<10 ns) recombination of an electron and a hole via the super-trap [16]. The experimentally observed relative PL blinking amplitude (the ratio between the PL intensity jump size and the average intensity) is dependent on the ratio of the recombination rate via the super-trap to all other recombination rates existing in the system [19,20]. The recombination rate via the super-trap for large crystals with sizes more than several hundreds of nanometres can be diffusion limited [15,16]. Therefore, we consider the following two possibilities when searching for the origin of the excitation wavelength dependence of PL flickering: idea-1) activation/deactivation of the super trap (and/or NR centres in general) is excitation wavelength dependent; idea-2) the diffusion of length the charge carriers is somehow dependent on the excitation wavelength. Let us consider these two ideas in detail below.

If the activation/de-activation of NR centres is wavelength dependent (idea-1), this dependence should reflect the excitation spectrum of the activation/deactivation process. We are not aware of any study where this possibility has been discussed for perovskites. Organic dye molecules, however, which fluorescence can be switched on and off by changing the colour of the light are well-known and used as labels for super-resolution imaging [35]. In perovskites, the wavelength dependent flickering can hypothetically be related to the absorption spectrum of the super trap or the species which can be converted to the NR centre by light. According to Quitsch et al. [13], irradiation by blue light ($\lambda <$ 530 nm) leads to decreasing of the PL intensity (which can be explained by increasing of the number of NR channels per crystal) while red illumination leads to PL enhancement (which can be explained by decreasing of the number of NR channels per crystal). If we assume that some of the NR channels are associated with the switchable super-traps, changing the concentration of the super-traps and their switching rate can change the PL flickering pattern. Increasing the contribution of the super trap to the total non-radiative recombination should increase the relative blinking amplitude. Admittedly, there is not enough experimental data to allow proposing any particular mechanism at the moment, but we believe that this hypothesis needs further attention and may be confirmed in the future.

Several literature reports indicate that the wavelength region around 500–530 nm is special in a sense that the behaviour of $MAPbI_3$ perovskite in terms of its PL and stability can be different when excited above and below this energetic border [13,32]. These studies suggest that the observed effects originate with formation of PbI_2 which has its bandgap in the discussed wavelength region. Can the observed effect of the excitation wavelength of PL flickering also have something to do with the formation of PbI_2 upon degradation?

In strongly degraded films like the one shown in Fig. 2c, photodegradation induces formation of PbI_2 around the remaining $MAPbI_3$ crystallites [30,36,37]. PbI_2 layer absorbs photons with $\lambda < 520$ nm but does not absorb "red" photons. The fate of the charge carriers generated in PbI_2 may be different. They either recombine inside PbI_2 itself, or diffuse to the interface between PbI_2 and $MAPbI_3$. Due to a smaller bandgap of $MAPbI_3$ and their band alignment[38], charge transfer from PbI_2 to $MAPbI_3$ is favourable. One would expect the charge carriers to enter $MAPbI_3$ and then behave the same as any other charge carriers generated in $MAPbI_3$ at the first place. However, recent work showed otherwise [32]. There it was demonstrated that carriers accumulate at the interfacial layer between PbI_2 and $MAPbI_3$, where they are able to recombine radiatively leading to PL spectrum resembling that of $MAPbI_3$, however with the PL decay kinetics drastically different from that of the PL generated by charge recombination in the bulk of $MAPbI_3$ by light with $\lambda > 530$ nm. This effectively inhibits charge carriers generated directly in PbI_2 diffuse further to the bulk $MAPbI_3$. Since the blinking of a large crystal requires charge diffusion over the whole volume to a single super trap, suppressing of the diffusion by localizing charge carriers in a spatially confined layer would supress PL blinking (idea 2). When the excitation wavelength is longer than 530 nm, charge carries are generated and stay in $MAPbI_3$ where the charge transport is very efficient and thus allowing for PL flickering to be observed.

5. Conclusions

We report a clear excitation wavelength dependence of PL blinking/flickering effect in degraded $MAPbI_3$ films. While blue excitation (wavelengths shorter than 530 nm) generated stable non-flickering PL, excitation with red light (wavelengths longer than 530 nm) lead to blinking and flickering of the PL intensity. We propose that the wavelength dependence might be related to the excitation wavelength dependence of the photochemical reactions in the material leading to generation/annihilation of the switchable non-radiative centres in $MAPbI_3$. Another idea is that PL flickering is supressed due to reduced charge carrier diffusion due to their localization in the interfacial layer between $MAPbI_3$ and PbI_2. At the moment we are not able to neither

reject nor support the presented ideas merely with the available experimental data and emphasize that more studies are needed. However, our discussion highlights the direction where the explanation of the phenomenon may be found.

Declaration of competing interest

The authors declare no conflict of interests.

Acknowledgements

This work was supported by the Swedish Research Council (2016–04433) and Knut and Alice Wallenberg foundation. E.L.U and A. M acknowledge funding from the German Ministry of Education and Research (BMBF) for the Young Investigator Group Hybrid Materials Formation and Scaling (HyPerFORME) within the program "NanoMatFutur" (grant no. 03XP0091) and the "SNaPSHoTs" project (grant no. 01IO1806).

Appendix A. Supplementary data

Supplementary data to this article can be found online at https://doi.org/10.1016/j.jlumin.2020.117129.

Authors statement

Alexander Kiligaridis: Methodology, Investigation, Writing- Original draft preparation, Writing- Reviewing and Editing, Aboma Merdasa: Investigation, Supervision, Methodology, Writing- Reviewing and Editing, Carolin Reherman: Investigation, Writing- Reviewing and Editing, Eva Unger: Conceptualization, Supervision, Writing- Reviewing and Editing, Ivan Scheblykin: Conceptualization, Supervision, Writing- Original draft preparation, Writing- Reviewing and Editing.

References

[1] Y. Fu, H. Zhu, J. Chen, M.P. Hautzinger, X.Y. Zhu, S. Jin, Metal halide perovskite nanostructures for optoelectronic applications and the study of physical properties, Nat. Rev. Mater. 4 (2019) 169–188, https://doi.org/10.1038/s41578-019-0080-9.
[2] E.M. Tennyson, T.A.S. Doherty, S.D. Stranks, Heterogeneity at multiple length scales in halide perovskite semiconductors, Nat. Rev. Mater. 4 (2019) 573–587, https://doi.org/10.1038/s41578-019-0125-0.
[3] D.A. Egger, A. Bera, D. Cahen, G. Hodes, T. Kirchartz, L. Kronik, R. Lovrincic, A. M. Rappe, D.R. Reichman, O. Yaffe, What remains unexplained about the properties of halide perovskites? Adv. Mater. 1800691 (2018) 1800691, https://doi.org/10.1002/adma.201800691.
[4] Y. Tian, M. Peter, E. Unger, M. Abdellah, K. Zheng, T. Pullerits, A. Yartsev, V. Sundström, I.G. Scheblykin, Mechanistic insights into perovskite photoluminescence enhancement: light curing with oxygen can boost yield thousandfold, Phys. Chem. Chem. Phys. 17 (2015) 24978–24987, https://doi.org/10.1039/C5CP04410C.
[5] F. De Angelis, A. Petrozza, Clues from defect photochemistry, Nat. Mater. 17 (2018) 383–384, https://doi.org/10.1038/s41563-018-0069-6.
[6] D. Meggiolaro, E. Mosconi, F. De Angelis, Mechanism of reversible trap passivation by molecular oxygen in lead-halide perovskites, ACS Energy Lett 2 (2017) 2794–2798, https://doi.org/10.1021/acsenergylett.7b00955.
[7] S.D. Stranks, Nonradiative losses in metal halide perovskites, ACS Energy Lett 2 (2017) 1515–1525, https://doi.org/10.1021/acsenergylett.7b00239.
[8] J.W. Lee, S.G. Kim, J.M. Yang, Y. Yang, N.G. Park, Verification and mitigation of ion migration in perovskite solar cells, Apl. Mater. 7 (2019), https://doi.org/10.1063/1.5085643.
[9] P. Fassl, V. Lami, A. Bausch, Z. Wang, M.T. Klug, H.J. Snaith, Y. Vaynzof, Fractional deviations in precursor stoichiometry dictate the properties, performance and stability of perovskite photovoltaic devices, Energy Environ. Sci. 11 (2018) 3380–3391, https://doi.org/10.1039/C8EE01136B.
[10] E. Mosconi, D. Meggiolaro, H.J. Snaith, S.D. Stranks, F. De Angelis, Light-induced annihilation of Frenkel defects in organo-lead halide perovskites, Energy Environ. Sci. 9 (2016) 3180–3187, https://doi.org/10.1039/c6ee01504b.
[11] J.F. Galisteo-López, M. Anaya, M.E. Calvo, H. Míguez, Environmental effects on the photophysics of organic–inorganic halide perovskites, J. Phys. Chem. Lett. 6 (2015) 2200–2205, https://doi.org/10.1021/acs.jpclett.5b00785.
[12] D.W. DeQuilettes, W. Zhang, V.M. Burlakov, D.J. Graham, T. Leijtens, A. Osherov, H.J. Snaith, D.S. Ginger, S.D. Stranks, Photo-induced Halide Redistribution in Organic–Inorganic Perovskite Films. https://doi.org/10.1038/ncomms11683, 2016.
[13] W.A. Quitsch, D.W. Dequilettes, O. Pfingsten, A. Schmitz, S. Ognjanovic, S. Jariwala, S. Koch, M. Winterer, D.S. Ginger, G. Bacher, The role of excitation energy in photobrightening and photodegradation of halide perovskite thin films, J. Phys. Chem. Lett. 9 (2018) 2062–2069, https://doi.org/10.1021/acs.jpclett.8b00212.
[14] D. Hong, Y. Zhou, S. Wan, X. Hu, D. Xie, Y. Tian, Nature of photoinduced quenching traps in methylammonium lead triiodide perovskite revealed by reversible photoluminescence decline, ACS Photonics 5 (2018) 2034–2043, https://doi.org/10.1021/acsphotonics.7b01537.
[15] Y. Tian, A. Merdasa, M. Peter, M. Abdellah, K. Zheng, C.S. Ponseca, T. Pullerits, A. Yartsev, V. Sundström, I.G. Scheblykin, Giant photoluminescence blinking of perovskite nanocrystals reveals single-trap control of luminescence, Nano Lett. 15 (2015) 1603–1608, https://doi.org/10.1021/nl5041397.
[16] A. Merdasa, Y. Tian, R. Camacho, A. Dobrovolsky, E. Debroye, E.L. Unger, J. Hofkens, V. Sundström, I.G. Scheblykin, "Supertrap" at work: extremely efficient nonradiative recombination channels in MAPbI 3 perovskites revealed by luminescence super-resolution imaging and spectroscopy, ACS Nano 11 (2017) 5391–5404, https://doi.org/10.1021/acsnano.6b07407.
[17] N. Pathoor, A. Halder, A. Mukherjee, J. Mahato, S.K. Sarkar, A. Chowdhury, Fluorescence blinking beyond nanoconfinement: spatially synchronous intermittency of entire perovskite microcrystals, Angew. Chem. Int. Ed. 57 (2018) 11603–11607, https://doi.org/10.1002/anie.201804852.
[18] C. Li, Y. Zhong, C.A.M. Luna, T. Unger, K. Deichsel, A. Gräser, J. Köhler, A. Köhler, R. Hildner, S. Huettner, Emission enhancement and intermittency in polycrystalline organolead halide perovskite films, Molecules 21 (2016) 1081, https://doi.org/10.3390/molecules21081081.
[19] M. Gerhard, B. Louis, R. Camacho, A. Merdasa, J. Li, A. Kiligaridis, A. Dobrovolsky, J. Hofkens, I.G. Scheblykin, Microscopic insight into non-radiative decay in perovskite semiconductors from temperature-dependent luminescence blinking, Nat. Commun. 10 (2019) 1698, https://doi.org/10.1038/s41467-019-09640-w.
[20] P.A. Frantsuzov, S. Volkán-Kacsó, B. Jankó, Model of fluorescence intermittency of single colloidal semiconductor quantum dots using multiple recombination centers, Phys. Rev. Lett. 103 (2009) 207402, https://doi.org/10.1103/PhysRevLett.103.207402.
[21] P.A. Frantsuzov, S. Volkán-Kacsó, B. Jankó, Universality of the fluorescence intermittency in nanoscale systems: experiment and theory, Nano Lett. 13 (2013) 402–408, https://doi.org/10.1021/nl3035674.
[22] N. Yarita, T. Aharen, H. Tahara, M. Saruyama, T. Kawawaki, R. Sato, T. Teranishi, Y. Kanemitsu, Observation of positive and negative trions in organic-inorganic hybrid perovskite nanocrystals, Phys. Rev. Mater. 2 (2018) 116003, https://doi.org/10.1103/PhysRevMaterials.2.116003.
[23] Y.S. Park, S. Guo, N.S. Makarov, V.I. Klimov, Room temperature single-photon emission from individual perovskite quantum dots, ACS Nano 9 (2015) 10386–10393, https://doi.org/10.1021/acsnano.5b04584.
[24] D.K. Sharma, S. Hirata, V. Biju, M. Vacha, Stark effect and environment-induced modulation of emission in single halide perovskite nanocrystals, ACS Nano 13 (2019) 624–632, https://doi.org/10.1021/acsnano.8b07677.
[25] J.M. Frost, A. Walsh, What is moving in hybrid halide perovskite solar cells? Acc. Chem. Res. 49 (2016) 528–535, https://doi.org/10.1021/acs.accounts.5b00431.
[26] D. Meggiolaro, S.G. Motti, E. Mosconi, A.J. Barker, J. Ball, C. Andrea Riccardo Perini, F. Deschler, A. Petrozza, F. De Angelis, Iodine chemistry determines the defect tolerance of lead-halide perovskites, Energy Environ. Sci. 11 (2018) 702–713, https://doi.org/10.1039/c8ee00124c.
[27] M. Anaya, J.F. Galisteo-López, M.E. Calvo, J.P. Espinós, H. Míguez, Origin of light-induced photophysical effects in organic metal halide perovskites in the presence of oxygen, J. Phys. Chem. Lett. 9 (2018) 3891–3896, https://doi.org/10.1021/acs.jpclett.8b01830.
[28] D.R. Ceratti, Y. Rakita, L. Cremonesi, R. Tenne, V. Kalchenko, M. Elbaum, D. Oron, M.A.C. Potenza, G. Hodes, D. Cahen, Self-healing inside APbBr3Halide perovskite crystals, Adv. Mater. 30 (2018) 1–7, https://doi.org/10.1002/adma.201706273.
[29] T. Kirchartz, L. Krückemeier, E.L. Unger, Research Update: recombination and open-circuit voltage in lead-halide perovskites, Apl. Mater. 6 (2018) 100702, https://doi.org/10.1063/1.5052164.
[30] N.H. Nickel, F. Lang, V.V. Brus, O. Shargaieva, J. Rappich, Unraveling the light-induced degradation mechanisms of CH 3 NH 3 PbI 3 perovskite films, Adv. Electron. Mater. 3 (2017) 1700158, https://doi.org/10.1002/aelm.201700158.
[31] A.F. Akbulatov, S.Y. Luchkin, L.A. Frolova, N.N. Dremova, K.L. Gerasimov, I. S. Zhidkov, D.V. Anokhin, E.Z. Kurmaev, K.J. Stevenson, P.A. Troshin, Probing the intrinsic thermal and photochemical stability of hybrid and inorganic lead halide perovskites, J. Phys. Chem. Lett. 8 (2017) 1211–1218, https://doi.org/10.1021/acs.jpclett.6b03026.
[32] A. Merdasa, A. Kiligaridis, C. Rehermann, M. Abdi-Jalebi, J. Stöber, B. Louis, M. Gerhard, S.D. Stranks, E.L. Unger, I.G. Scheblykin, Impact of excess lead iodide on the recombination kinetics in metal halide perovskites, ACS Energy Lett 4 (2019) 1370–1378, https://doi.org/10.1021/acsenergylett.9b00774.
[33] A. Halder, N. Pathoor, A. Chowdhury, S.K. Sarkar, Photoluminescence flickering of micron-sized crystals of methylammonium lead bromide: effect of ambience and light exposure, J. Phys. Chem. C 122 (2018) 15133–15139, https://doi.org/10.1021/acs.jpcc.8b03862.
[34] S.D. Stranks, G.E. Eperon, G. Grancini, C. Menelaou, M.J.P. Alcocer, T. Leijtens, L. M. Herz, A. Petrozza, H.J. Snaith, Electron-hole diffusion lengths exceeding 1 micrometer in an organometal trihalide perovskite absorber, Science 342 (2013) 341–344, https://doi.org/10.1126/science.1243982.
[35] D. Wöll, C. Flors, Super-resolution fluorescence imaging for materials science, Small Methods 1700191 (2017) 1700191, https://doi.org/10.1002/smtd.201700191.

[36] J. Yang, B.D. Siempelkamp, D. Liu, T.L. Kelly, Investigation of CH 3 NH 3 PbI 3 degradation rates and mechanisms in controlled humidity environments using in situ techniques, ACS Nano 9 (2015) 1955, https://doi.org/10.1021/nn506864k. –1963.

[37] A. Merdasa, M. Bag, Y. Tian, E. Källman, A. Dobrovolsky, I.G. Scheblykin, Super-resolution luminescence microspectroscopy reveals the mechanism of photoinduced degradation in CH 3 NH 3 PbI 3 perovskite nanocrystals, J. Phys. Chem. C 120 (2016) 10711–10719, https://doi.org/10.1021/acs.jpcc.6b03512.

[38] D.H. Cao, C.C. Stoumpos, C.D. Malliakas, M.J. Katz, O.K. Farha, J.T. Hupp, M. G. Kanatzidis, Remnant PbI2, an unforeseen necessity in high-efficiency hybrid perovskite-based solar cells? Apl. Mater. 2 (2014), 091101 https://doi.org/10.1063/1.4895038.

Paper II

ACS Energy Letters

Cite This: ACS Energy Lett. 2019, 4, 1370−1378

http://pubs.acs.org/journal/aelccp

LETTER

Impact of Excess Lead Iodide on the Recombination Kinetics in Metal Halide Perovskites

Aboma Merdasa,*,† Alexander Kiligaridis,‡ Carolin Rehermann,† Mojtaba Abdi-Jalebi,§ Jonas Stöber,‡ Boris Louis,‡ Marina Gerhard,‡ Samuel D. Stranks,§ Eva L. Unger,*,†,‡ and Ivan G. Scheblykin*,‡

†Young Investigator Group Hybrid Materials Formation and Scaling, Helmholtz-Zentrum Berlin für Materialen und Energie GmbH, Albert-Einstein Strasse 16, 12489 Berlin, Germany

‡Chemical Physics and NanoLund, Lund University, P.O. Box 124, 22100 Lund, Sweden

§Cavendish Laboratory, Department of Physics, University of Cambridge, JJ Thomson Avenue, Cambridge CB3 0HE, United Kingdom

Supporting Information

ABSTRACT: Fundmental comprehension of light-induced processes in perovskites are still scarce. One active debate surrounds the influence of excess lead iodide (PbI_2) on device performance, as well as optoelectronic properties, where both beneficial and detrimental traits have been reported. Here, we study its impact on charge carrier recombination kinetics by simultaneously acquiring the photoluminescence quantum yield and time-resolved photoluminescence as a function of excitation wavelength (450−780 nm). The presence of PbI_2 in the perovskite film is identified via a unique spectroscopic signature in the PLQY spectrum. Probing the recombination in the presence and absence of this signature, we detect a radiative bimolecular recombination mechanism induced by PbI_2. Spatially resolving the photoluminescence, we determine that this radiative process occurs in a small volume at the PbI_2/perovskite interface, which is only active when charge carriers are generated in PbI_2, and therefore provide deeper insight into how excess PbI_2 may improve the properties of perovskite-based devices.

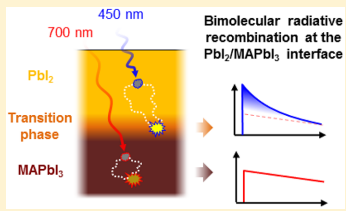

Metal halide perovskites have in merely a decade become strong contenders for absorber materials in commercially competitive solar cells, where recent advances are yielding power conversion efficiencies approaching that of silicon-based devices.[1−3] One limiting factor has long been the issue of poor stability under operational conditions, which for some time seemed an unfeasible hurdle to overcome. However, recent progress in compositional engineering of metal halide perovskite absorbers demonstrates that this is becoming less of an obstacle,[4,5] resulting in improved efficiency and stability under concentrated illumination.[6] Investigating the effect of long-term light exposure is of crucial importance to predict the intrinsic material stability and design more stable alternatives.

It is known that lead iodide-based metal halide perovskite semiconductors decompose into lead iodide (PbI_2) when exposed to a range of external stimuli, of which photons are highly relevant.[7−14] While decomposition of the perovskite absorber is clearly an undesirable effect, reports emerged early hinting toward beneficial aspects with perovskites containing an excess of PbI_2.[15−17] This sparked a debate around the role that residual PbI_2 actually plays, generating a number of publications dealing with the impact on material[18−20] and device properties,[21−23] which is nicely summarized by Jacobsson and co-workers.[24] Today, the general consensus seems to be that a slight excess of PbI_2 improves key device parameters, such as the open-circuit voltage (V_{OC}), short-circuit current, and the overall power conversion efficiency, but suffers the cost of reduced long-term stability.[25,26]

From a more fundamental perspective, it has been demonstrated that recombination between charge carriers in the absorber and transport layers has been suppressed due to a thin interfacial layer of PbI_2.[27−29] In regard to charge carriers that form in the perovskite absorber, both a reduction of nonradiative recombination and accelerated recombination with an excess of PbI_2 have been postulated.[30−32] These reports do not necessarily contradict one another but may rather reflect a dependence on where and how PbI_2 has been introduced in the perovskite. So far, investigations have focused on charge carriers formed in the perovskite layer

Received: April 10, 2019
Accepted: May 17, 2019
Published: May 22, 2019

ACS Publications © 2019 American Chemical Society

DOI: 10.1021/acsenergylett.9b00774
ACS Energy Lett. 2019, 4, 1370−1378

only, while those that form in PbI_2 are assumed parasitically lost and therefore not considered to partake in subsequent recombination mechanisms.

Recombination of charge carriers is an important factor dictating the performance of a solar cell device, where nonradiative recombination should ideally be eliminated.[33] This aspect is of key relevance when examining the properties of the absorber material without transport layers or contacts. Photoluminescence quantum yield (PLQY) measurements become important as they provide a qualitative measure of the competition between radiative and nonradiative processes. While both steady-state and time-resolved photoluminescence (PL) experiments are used as standard methods to characterize the optoelectronic properties of perovskite absorbers, as well as predict device performance,[34−36] a few considerations must be made. Steady-state PL alone cannot provide information on the recombination dynamics of photogenerated charge carriers and should hence be complemented with time-resolved PL (TRPL) measurements. At the same time, a long carrier lifetime can be obtained even if the PLQY is low, which may therefore by itself be a misleading figure of merit when assessing potential device performance, unless accompanied by extensive modeling.[37] Thus, in order to better characterize the light conversion properties of a material and also describe the underlying recombination processes via optical probes, TRPL and PLQY should be, where possible, performed in a complementary manner.[38]

Herein, we present a study on the recombination kinetics in methylammonium lead triiodide ($MAPbI_3$) films and the impact caused by PbI_2 when formed as a photoinduced degradation product over several hours, as well as via vapor-assisted deposition. Extracting the PLQY as a function of wavelength (450−780 nm) during light-soaking, we find a unique spectral signature related to the PbI_2 absorption onset, allowing us monitor its formation in time. By simultaneously acquiring the TRPL at excitation wavelengths between 450 and 700 nm, we identify a change in the charge carrier recombination mechanism occurring in $MAPbI_3$ facilitated by PbI_2. Employing fluence-dependent TRPL and spatially resolved spectroscopic measurements, we determine that charge carriers generated in PbI_2 funnel to a transition phase interlinking PbI_2 and $MAPbI_3$ where they undergo radiative bimolecular recombination with a blue-shifted PL emission in relation to typical $MAPbI_3$ emission (775 nm). Our observations therefore provide necessary insight into how the overall recombination kinetics in $MAPbI_3$ may be altered by PbI_2, which may further resolve some of the ambiguity surrounding the role of PbI_2 in regard to both material and device properties.

Spectrally Resolved PL Quantum Yield. $MAPbI_3$ thin films were prepared inside of a glovebox on thin glass substrates according to the methods outlined in the Supporting Information, where the structure and morphology of the films were characterized by SEM and XRD (see SI Note 1). Optical characterization was made in a novel microscope developed to simultaneously measure PL excitation (PLE) spectra together with absorptance in the wavelength range of 450−780 nm. For excitation, we employed a tunable pulsed laser source, allowing us to also acquire the TRPL (see the SI for further details). PLE spectra were acquired by scanning the excitation from 450 to 780 nm while integrating PL from the tail of the emission band above 790 nm (Figure 1a). Calibrating the excitation density to 0.1 W/cm^2 (1 Sun), we

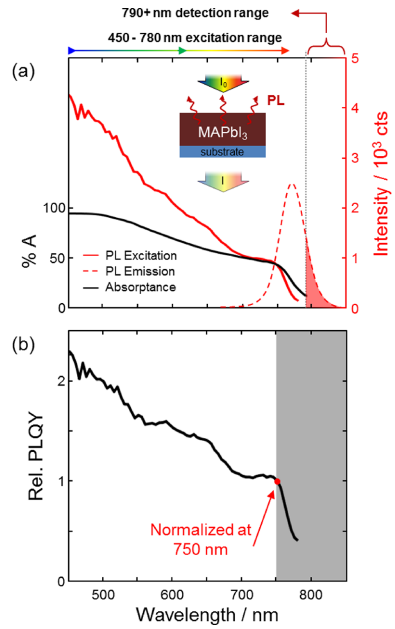

Figure 1. (a) Absorptance (%*A*, black trace), PLE (red/solid trace), and PL emission (red/dashed trace) spectra. The red shaded region indicates which part of the PL emission band is integrated for the PLE signal. The inset schematic demonstrates the measurement geometry where PL is detected in the same direction of the incoming light where %$A = (1 - (I/I_0) \times 100$. (b) Relative PLQY spectrum acquired by dividing the PLE spectrum by the absorptance spectrum. The PLQY spectrum is normalized at 750 nm. The gray shaded region indicates the spectral range (>750 nm) where uncertainty is high due to a low PLE signal.

simultaneously light-soaked the sample while also probing the optoelectronic properties (see SI Note 2 for details). Unless otherwise noted, measurements were conducted such that the excitation impinged on the material side of the sample, where PL also was collected (see the inset in Figure 1a).

Figure 1a shows the PLE and the absorptance (%*A*) spectra of a $MAPbI_3$ film prior to extensive light-soaking. We can quantify the difference by extracting the relative PL quantum yield spectrum (henceforth just PLQY), which we acquire by dividing the PLE spectrum by the absorptance spectrum (Figure 1b), and observe that the yield is twice as high at 450 nm compared to that at 750 nm. We have indications that this may be related to the amount of excess/lack of PbI_2 formed in the perovskite, which is obtained by varying the PbI_2/MAI precursor molar ratios (see Figure S4), although more extensive measurements are required to verify this with better certainty.

Spectral Fingerprint of PbI_2. We performed simultaneous PLE/absorptance measurements for 120 consecutive excitation scans, extracting PLQY spectra in each round. We measured in ambient air with a relative humidity around 40%, which are conditions typical for PbI_2 formation under light exposure[8] (see Figure S5 for measurements in dry nitrogen). The 2D maps in Figure 2a,b show the evolution of the absorptance and

DOI: 10.1021/acsenergylett.9b00774
ACS Energy Lett. 2019, 4, 1370−1378

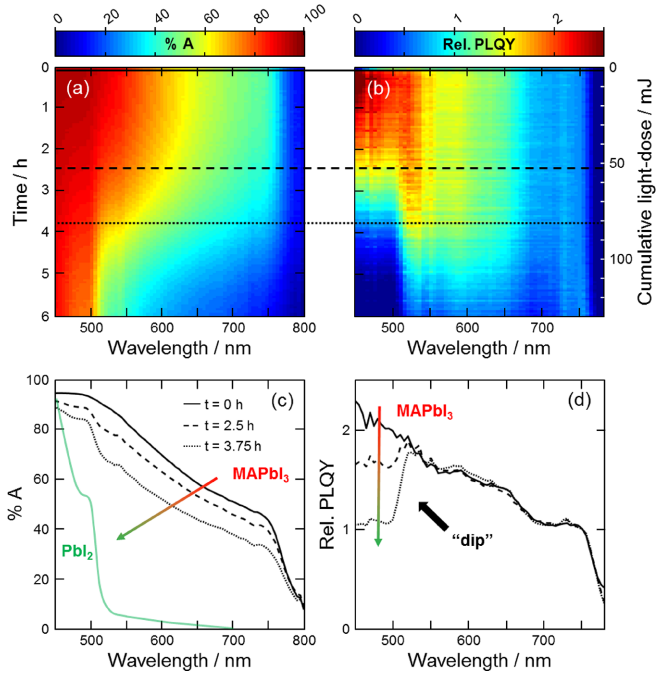

Figure 2. 2D maps showing the temporal evolution of (a) absorptance and (b) normalized PLQY spectra during 6 h of light-soaking. PLQY spectra are normalized at 750 nm. The right vertical axis shows the cumulative light dose throughout the experiment. (c,d) Selected spectra from the two maps at three points in time, t = 0 (solid), 2.5 (dashed), and 3.75 h (dotted). The PbI_2 absorption spectrum in (c) is adapted with permission from ref 45. The "dip" in (d) is the indicator of PbI_2 formation.

normalized PLQY spectra during the 6 h measurement, with selected spectra from three instances plotted in Figure 2c,d. From the absorptance, we verify that $MAPbI_3$ decomposes into PbI_2. After 2.5 h, we find that the PLQY starts to drop off for a very distinct spectral range (between 450 and 520 nm), forming what we will refer to as a "dip" in the PLQY spectrum, which coincides with the absorption of PbI_2. We explain this as photons that are absorbed in PbI_2 and generate charge carriers are parasitically lost (filter effect),[39] even if they recombine radiatively because PbI_2 emission (~520 nm) is filtered out in our detection scheme (see Figure 1a).

Figure 2b shows that the normalized PLQY spectrum remains unchanged for the first few hours, although the non-normalized spectra (Figure S6) demonstrate that there is significant PL enhancement prior to any degradation. The general consensus in the community is that an increase in the PLQY during light-soaking is related to passivation/annihilation of defects, although it is still debated whether this is mediated by atmospheric species (O_2, H_2O),[40−42] migrating ions,[43] and/or PbI_2 itself.[16] Quitsch and co-workers recently demonstrated a strong dependence of photoinduced PL enhancement/degradation on excitation wavelength, where enhancement (photobrightening) was exclusively reported for excitation wavelengths longer than 520 nm.[44] Because we here focus on the photoinduced formation of PbI_2 (degradation), normalizing the PLQY spectra at 750 nm removes the spectral signature of photobrightening (observed for longer wavelengths), which isolates the signature of PbI_2 formation, as shown in Figure 2d.

Spectrally and Temporally Resolved PL. We acquire PLQY spectra (Figure 3a) with intermittent measurements of the PL decay kinetics using 450 and 700 nm excitation wavelengths (Figure 3b) during 600 min of light-soaking. We employ the time-correlated single-photon counting (TCSPC) method and fit the PL decays with a stretched exponential function from which we extract the average lifetimes (Figure 3c), as detailed in SI Note 2 (measurement) and SI Note 3 (fitting). Prior to any extensive light-soaking, the average lifetimes are similar for both excitation wavelengths. The monoexponential nature of the decays points to the dominant recombination mechanism being trap-assisted,[46] which is consistent with the estimated photogenerated carrier density ($\Delta n \approx 10^{15}$ cm^{-3}; see SI Note 2) being an order of magnitude lower than the trap density ($N_t \approx 10^{16}$ cm^{-3}) that is typically reported for solution-processed $MAPbI_3$ films.[43,47] Even if the photon flux is kept constant, the carrier generation toward the excited surface (where we also detect PL) is expected to be slightly higher for 450 nm excitation because the absorption coefficient is higher, which is reflected in the marginally higher initial amplitude of the decay. However, we establish that at t = 0 min this difference in generation is not sufficient to induce a different recombination mechanism.

During the first few hours, the lifetimes of both decays increase in a similar fashion and maintain their monoexpo-

DOI: 10.1021/acsenergylett.9b00774
ACS Energy Lett. 2019, 4, 1370−1378

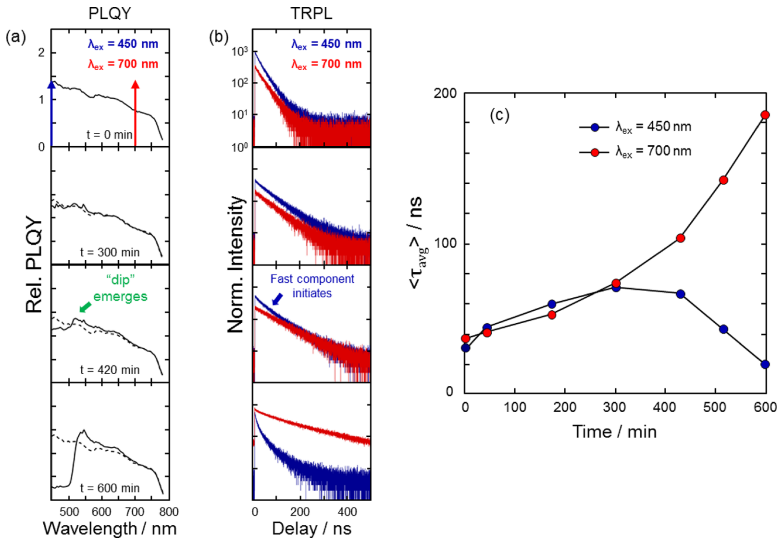

Figure 3. (a) PLQY spectra at four instances throughout the 10 h light-soaking experiment. The dashed traces in the bottom three panels represent the PLQY at t = 0 min. The vertical scale is the same for all panels. (b) PL decays generated with 450 (blue traces) and 700 nm (red traces) excitation energies at the same time instances as those shown in (a). The vertical scale is the same for all panels. The two excitation wavelengths generating the PL decays in (b) are indicated by blue (450 nm) and red (700 nm) arrows in the top panel of (a). (c) Average lifetimes extracted using stretched exponential fits for both excitation wavelengths (see Figure S8 for the complete data set and fit parameters).

nential shape while the PLQY also increases, which are both commonly reported signatures of photoinduced defect passivation[40] (see Figure S7 for non-normalized PLQY spectra). However, once the PbI_2-related dip emerges in the PLQY spectrum (t = 420 min), an additional fast component in the PL decay evolves only for 450 nm excitation. With further light-soaking, the PbI_2-related PLQY dip increases while the discrepancy between the two PL decays becomes even more pronounced, which is demonstrated in Figure 3c.

In Figure 3b, we can see two distinct features in the PL kinetics evolve: (i) increasing of the slow decay component, which is observed as soon as light-soaking initiates, and (ii) increasing of the fast decay component, which has an onset after a few hours. Process (i) occurs for both excitation wavelengths, while process (ii) occurs exclusively for 450 nm. Regardless of the underpinning mechanism, we conclude that (i) appears as a result of passivation of nonradiative recombination channels, as previously reported.[40] Process (ii) appears when a substantial dip in the PLQY spectrum (t = 420 min) emerges, which, interestingly, only seems to be present when exciting in the spectral range of PbI_2 absorption (450−520 nm). As the detection excludes emission from PbI_2, we conclude that the carrier recombination kinetics can be altered in the perovskite by the mere presence of PbI_2, as long as photons are absorbed by it.

Probing the Recombination Mechanism. Having indications of a different recombination mechanism in the perovskite that is active only when charge carriers are generated in PbI_2, we investigate the effect of a 130 nm thick PbI_2 layer evaporated on top of a 400 nm thick $MAPbI_3$ thin film (see cross-section SEM in Figure 4a) and compare the PL kinetics to a reference sample without any evaporated PbI_2. Assuming similar absorption coefficients for PbI_2 and $MAPbI_3$,[48] the 130 nm PbI_2 layer should absorb approximately 75−80% of photons for excitation wavelengths between 450 and 520 nm. The non-normalized PLQY spectrum in comparison to the reference sample (without a PbI_2 layer) not only verifies that the so-called "dip" is related to PbI_2 but also shows that there is a 2-fold increase of the PLQY for wavelengths longer than 520 nm (Figure 4b). This observation supports the notion that PbI_2 passivates the $MAPbI_3$ surface,[16,30] although our results suggests that it is only visible when probed with excitation wavelengths longer than 520 nm.

The PLQY of the sample containing a layer of PbI_2 is approximately 80% lower in the range of the dip compared to the reference sample, which is similar to the percentage of expected photon absorption in PbI_2. From the PLQY alone, it would therefore seem that the detected emission comes from charge carriers that are directly generated in $MAPbI_3$ via absorption of photons that manage to penetrate through the PbI_2 layer (for λ_{ex} = 450−520 nm). However, when comparing the PL decays at 450 and 700 nm, we see the same discrepancy as previously observed (Figure 4c). We cannot rationalize why such different PL kinetics are observed between the two excitation wavelengths with only a marginal difference in the charge carrier concentration directly generated in $MAPbI_3$ (depth-resolved carrier generation profiles schematically drawn in Figure 4a are estimated from α in ref 48). Furthermore, such a scenario would require a 100% radiative yield of the carriers generated in the $MAPbI_3$ layer for 450 nm excitation in order to explain the matching PLQY reduction and estimated parasitic losses, which finds no support in the

DOI: 10.1021/acsenergylett.9b00774
ACS Energy Lett. 2019, 4, 1370−1378

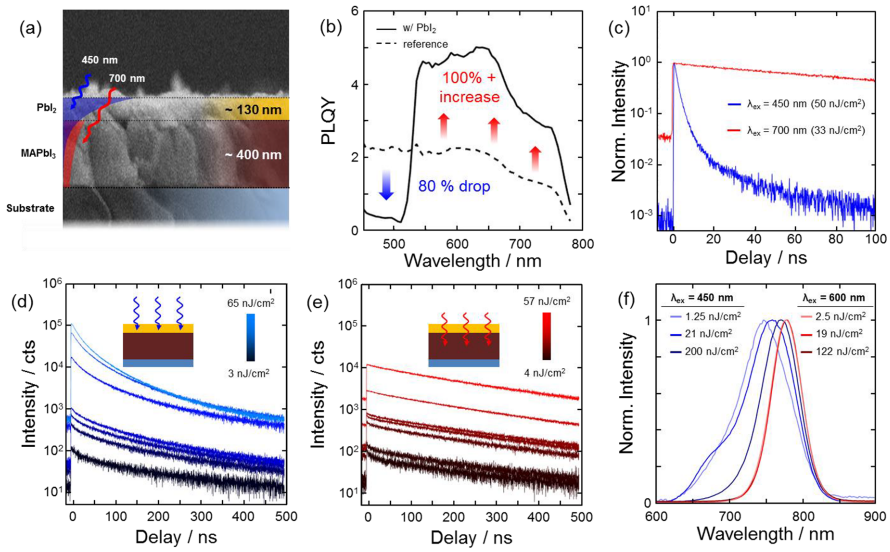

Figure 4. (a) Cross-section SEM micrograph showing the thickness of the evaporated PbI_2 layer (~130 nm) as well as the $MAPbI_3$ layer (~400 nm). Blue and red shaded regions show the carrier generation profiles with 450 and 700 nm excitation wavelengths, respectively, when exciting with the same photon flux. (b) PLQY of the PbI_2-evaporated sample (solid) in comparison to a reference film without a PbI_2 layer (dashed). The blue arrow indicates the "dip" (reduction of PLQY) due to PbI_2, and the red arrow indicates the subsequent 2-fold PL enhancement. (c) PL decays acquired for λ_{ex} = 450 nm (blue) and λ_{ex} = 700 nm (red). Fluence-dependent PL decay curves for (d) 450 nm (black/blue traces) and (e) 700 nm (black/red traces). The schematics show from which direction the sample is excited, where PL is collected from the same side. (f) Fluence-dependent PL spectra acquired with 450 nm excitation (blue traces) and 600 nm excitation (red traces) with a long-pass emission filter at 610 nm.

literature for the films investigated here. We therefore conclude that there must be a radiative component that is missing in our analysis.

We measure PL decays at various pulse fluences with the two excitation wavelengths (450 and 700 nm). When exciting through the PbI_2 layer first, it becomes evident that there is a carrier density-dependent recombination mechanism present for only 450 nm excitation (Figure 4d, λ_{ex} = 450 nm; Figure 4e, λ_{ex} = 700 nm). Measuring through the substrate side of the sample, thus absorbing directly into $MAPbI_3$, both excitation wavelengths generate similar monoexponential PL decays (Figure S8). We therefore relate the emerging fast component to a higher-order bimolecular recombination process, which is enabled by the presence of PbI_2.

The pulse fluences where bimolecular recombination becomes dominant are relatively low (a few nJ/cm^2) compared to other reports on similarly prepared perovskite thin films.[47] Furthermore, we demonstrated in the light-soaking experiment (Figure 3) that the PL decay for λ_{ex} = 450 nm changes without altering the pulse fluence. This suggests that the predominant recombination mechanism transitions from monomolecular to bimolecular recombination with the formation of PbI_2 alone. Indeed, we have indications that photoinduced passivation of defects is at play (photobrightening), but if N_t were to reduce to a point where bimolecular recombination becomes relevant ($\Delta n \approx N_t$), we should see this expressed in the PL decays generated with all excitation wavelengths. Because this is not the case (see Figure S8), we find the most logical explanation to be that the actual volume into which charge carriers accumulate and recombine is much smaller than that previously estimated for the entire film with thickness d = 400 nm. This consequently yields an effective carrier density (Δn_e) that could be orders of magnitude larger than Δn. Therefore, if charge carriers become confined by some mechanism induced by PbI_2, bimolecular recombination could indeed become the predominant recombination mechanism, even with a rather low incident flux.

We measure the PL spectra with 450 nm excitation as a function of excitation density (exciting through the PbI_2 layer) using a long-pass filter at 610 nm. At the lowest fluence, we observe that there is a strong blue-shift and broadening of the PL band. In fact, rather than a single emission band, the irregular shape of the blue-shifted PL spectra is indicative of a collection of overlapping bands. With higher fluence, the PL spectrum red-shifts and becomes more narrow. With λ_{ex} = 600 nm, we excite $MAPbI_3$ directly and not via PbI_2, and the PL emission peak remains at 775 nm and exhibits no shift or broadening/narrowing when changing excitation density (Figure 4f). Measuring through the substrate side first (direct absorption by $MAPbI_3$), we see a steady, nonshifting nor broadening PL spectrum centered at 775 nm (Figure S9) for both excitation wavelengths. We therefore conclude that the blue-shifted emission is caused by direct excitation into PbI_2 and consequently relate the blue-shifted emission to the PbI_2-enabled bimolecular recombination.

We acquire PL images generated with excitation wavelengths ranging from 450 to 700 nm (see SI Note 2 for details). Figure 5a shows two PL images of the same region generated with 450

DOI: 10.1021/acsenergylett.9b00774
ACS Energy Lett. 2019, 4, 1370−1378

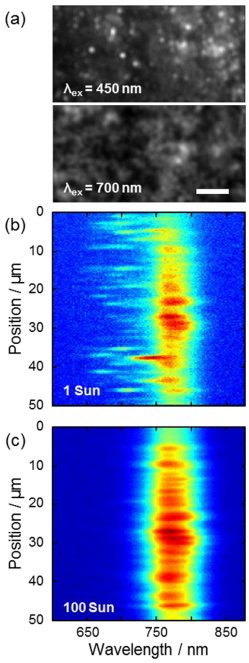

Figure 5. (a) PL images of the same region measured with λ_{ex} = 450 (top) and 700 nm (bottom), showing bright emissive domains with the former. The scale bar represents 5 μm. (b) Spatially resolved PL spectra identifying a distribution of blue-shifted PL peaks related to the emissive domains observed in (a) for an excitation density of 1 Sun. (c) Spatially resolved spectra from same region with the excitation density increased to 100 Sun, where the blue-shifted peaks disappear. The excitation wavelength in (b) and (c) is 450 nm.

and 700 nm excitation, where bright domains are only observed for the former. These domains disappear once the excitation wavelength is longer than 520 nm (see Figures S10 and S11 for PL images with excitation wavelengths between 450 and 600 nm). This points to the PL emission related to the PbI_2-enabled recombination mechanism coming from localized domains, which also supports the notion that the recombination mechanism is induced by charge carriers becoming confined when generated in PbI_2.

We also extract spatially resolved spectra from a ~2 μm wide vertical segment of the image and capture the PL spectra of these bright domains when exciting with 450 nm. Each horizontal line in Figures 5b,c represents the spectrum from a point in the vertical segment from the image (see SI Note 2 for details). It becomes evident that not only do the bright domains exhibit blue-shifted emission but also that there is a distribution of how large the shift is (Figure 5b), which explains the irregular shape of the spatially averaged PL spectra in Figure 4f. Moreover, as the fluence is increased by 2 orders of magnitude, the blue-shifted localized emission disappears, showing only the expected emission from $MAPbI_3$ at 775 nm (Figure 5c).

PbI_2/$MAPbI_3$ Interface-Assisted Recombination. Because we observe a red shift of the emission toward that of pristine $MAPbI_3$ with increasing power (Figure 5c), we rule out the Burstein–Moss effect (band-filling)[49] as the mechanism giving rise to the spectral shifts. We previously reported blue-shifted PL in $MAPbI_3$ single crystals and films arising from intermediate phases between the $MAPbI_3$ and PbI_2 structure exhibiting distortions and differences in connectivity between lead halide octahedra due to the loss of structure-stabilizing methylammonium cations.[11,50] This spatial gradient of lattice distortion consequently gives rise to a band gap gradient, increasing in energy from $MAPbI_3$ toward PbI_2 regions. We therefore propose that as PbI_2 forms in the perovskite, whether via a photoinduced process or evaporation, it gives rise to a transition phase at the PbI_2/$MAPbI_3$ interface comprising a small volume that alters the recombination kinetics. Our observations suggest that the Δn_e giving rise to the higher-order recombination mechanism arises due to the confinement of charge carriers, from which we find it likely that charge carriers generated in PbI_2 funnel into the relatively small volume of the disordered interface.

Supasai and co-workers demonstrated quite early that PbI_2 induces defects at the interface to $MAPbI_3$, which could certainly trap charge carriers funneled from PbI_2.[15] Once trapped, carriers may recombine and yield emission with higher energy than the $MAPbI_3$ band gap. It is also reported that carrier mobility is reduced in a disordered energy landscape, which also, according to Langevin theory, should increase the rate of free electron/hole recombination.[51] Regardless of the mechanism via which charge carriers accumulate, we conclude that radiative recombination must occur with a transition energy higher than the $MAPbI_3$ band gap. Figure 5b shows that a low fluence yields a broad emission, which arises from both the PbI_2/$MAPbI_3$ interface and bulk $MAPbI_3$. As the fluence increases, the interface saturates due to its relatively small volume, which leads to more carriers transferring to the $MAPbI_3$ bulk, where emission at 775 nm becomes dominant. Therefore, increasing the fluence manifests as a red shift and narrowing of the PL emission.

Direct absorption into the transition phase with excitation wavelengths longer than 520 nm should also occur, but because this phase comprises such a small volume in the film the majority of photons are absorbed in the $MAPbI_3$ bulk, yielding emission at 775 nm, with the predominant recombination mechanism being monomolecular (judging from the decays in Figures 3 and 4 for λ_{ex} > 520 nm). Thus, the population of the transition phase with charge carriers is most effective when injecting them via PbI_2. We summarize the proposed recombination mechanism occurring at the PbI_2/$MAPbI_3$ interface in Figure 6.

In summary, we have presented an in-depth spectroscopic study on the role of PbI_2 in $MAPbI_3$ thin films when it has been formed as a photoinduced degradation product and via vapor-assisted deposition. Combining measurements of PLQY and TRPL, we identify three optical signatures that can be used to detect the presence of PbI_2 in $MAPbI_3$ thin films: (i) parasitic absorption, (ii) a fast recombination component in the PL decay, and (iii) a blue shift of PL emission. Each of these phenomena exhibits a dependence on excitation wavelength and the geometry in which the sample is excited when PbI_2 is present. Furthermore, these signatures are only present when charge carriers are generated in PbI_2 directly.

DOI: 10.1021/acsenergylett.9b00774
ACS Energy Lett. 2019, 4, 1370−1378

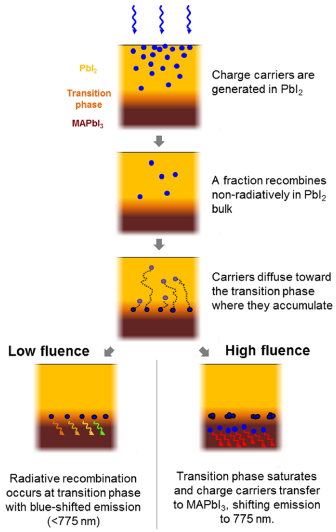

Figure 6. Schematic demonstrating the recombination mechanism via PbI_2 with an excitation wavelength within the range of PbI_2 absorption (450−520 nm) at low vs high fluence. Charge carriers are first generated by direct absorption in PbI_2 (top), after which a fraction recombines nonradiatively in the PbI_2 bulk. Remaining charge carriers diffuse to the transition phase where they accumulate and effectively yield a high carrier density. This subsequently leads to an increased rate of radiative recombination having blue-shifted PL emission. As the fluence increases, the transition phase saturates and recombination in the $MAPbI_3$ bulk becomes successively more dominant, causing the PL emission to shift toward 775 nm while also becoming narrower.

Thus, depending on the configuration in which the measurement is made, one can acquire some information in regard to where in the perovskite (sample) PbI_2 is predominantly present or starts forming (i.e., toward the top or the bottom surface of the film).

We also characterize the underpinning mechanism giving rise to phenomena (ii) and (iii) as a radiative bimolecular recombination mechanism occurring in a confined volume at the $PbI_2/MAPbI_3$ interface. Because charge carriers accumulate in a small volume, bimolecular recombination may still occur despite a relatively low incident photon flux. Thus, as PbI_2 induces parasitic losses for photons in the range between 450 and 520 nm, our results imply that a relevant portion of these charge carriers may in fact contribute to the V_{OC} of the perovskite. We therefore provide insight into the open debate regarding the beneficial/detrimental aspect of excess PbI_2 with a simple picture where we assume that the interface between PbI_2 and $MAPbI_3$ contributes to the beneficial aspect (radiative recombination) and the bulk PbI_2 contributes to the detrimental aspect (nonradiative recombination). Thus, the surface-to-volume ratio of PbI_2 domains within the perovskite bulk, and also where in relation to the incoming light they form, may affect the overall recombination kinetics. Finally, the notion of PbI_2 acting as a funnel for charge carriers to a defined disordered region at the interface between $MAPbI_3$ and PbI_2 could certainly inspire new designs for device applications, not only for perovskite photovoltaics but also for materials science in general.

■ ASSOCIATED CONTENT

Supporting Information

The Supporting Information is available free of charge on the ACS Publications website at DOI: 10.1021/acsenergylett.9b00774.

Sample preparation with XRD and SEM characterization, experimental setup and measurement procedures, stretched exponential fitting, measurements on precursor-modified non-stoichiometric $MAPbI_3$, measurements in N_2 vs humid air, PLQY data without normalization, TRPL of all excitation wavelengths and analysis, fluence-dependent TRPL and PL spectra, and PL images with different excitation wavelengths (PDF)

■ AUTHOR INFORMATION

Corresponding Authors

*E-mail: aboma.merdasa@helmholtz-berlin.de.
*E-mail: eva.unger@helmholtz-berlin.de.
*E-mail: ivan.scheblykin@chemphys.lu.se.

ORCID

Aboma Merdasa: 0000-0002-6298-5672
Mojtaba Abdi-Jalebi: 0000-0002-9430-6371
Boris Louis: 0000-0003-2882-6907
Marina Gerhard: 0000-0002-6539-4675
Samuel D. Stranks: 0000-0002-8303-7292
Eva L. Unger: 0000-0002-3343-867X
Ivan G. Scheblykin: 0000-0001-6059-4777

Notes

The authors declare no competing financial interest.

■ ACKNOWLEDGMENTS

A.M. would like to acknowledge Dr. Charles Hages, Prof. Thomas Unold, and Dr. Thomas Dittrich for fruitful discussions in regard to the TRPL data and the model. Thanks to Katrin Hirselandt, Carola Klimm, Marcel Roβ, and Zarha Andaji-Garmaroudi for assisting in sample preparation/transport and SEM characterization. E.L.U. and A.M. acknowledge funding from the German Ministry of Education and Research (BMBF) for the Young Investigator Group Hybrid Materials Formation and Scaling (HyPerFORME) within the program "NanoMatFutur" (Grant No. 03XP0091) and the "SNaPSHoTs" project (Grant No. 01IO1806). M.A.-J. thanks Cambridge Materials Limited and EPSRC (Grant Number: EP/M005143/1) for their funding and technical support. J.S. thanks Erasmus for a mobility grant. M.G. thanks the Wenner-Gren Foundation for a postdoctoral scholarship. S.D.S. acknowledges support from the Royal Society and Tata Group (UF150033). I.G.S. acknowledges support from the Swedish Research Council (2016-04433)

■ REFERENCES

(1) Kojima, A.; Teshima, K.; Shirai, Y.; Miyasaka, T. Organometal Halide Perovskites as Visible-Light Sensitizers for Photovoltaic Cells. *J. Am. Chem. Soc.* **2009**, *131* (17), 6050−6051.

(2) Lee, M. M.; Teuscher, J.; Miyasaka, T.; Murakami, T. N.; Snaith, H. J. Efficient Hybrid Solar Cells Based on Meso-Superstructured Organometal Halide Perovskites. *Science* **2012**, *338* (6107), 643−647.

(3) Jeon, N. J.; Na, H.; Jung, E. H.; Yang, T. Y.; Lee, Y. G.; Kim, G.; Shin, H. W.; Il Seok, S.; Lee, J.; Seo, J. A Fluorene-Terminated Hole-

DOI: 10.1021/acsenergylett.9b00774
ACS Energy Lett. 2019, 4, 1370−1378

Transporting Material for Highly Efficient and Stable Perovskite Solar Cells. *Nat. Energy* **2018**, *3*, 682−689.
(4) Abdi-Jalebi, M.; Andaji-Garmaroudi, Z.; Cacovich, S.; Stavrakas, C.; Philippe, B.; Richter, J. M.; Alsari, M.; Booker, E. P.; Hutter, E. M.; Pearson, A. J.; et al. Maximizing and Stabilizing Luminescence from Halide Perovskites with Potassium Passivation. *Nature* **2018**, *555* (7697), 497−501.
(5) Sanchez, S.; Christoph, N.; Grobety, B.; Phung, N.; Steiner, U.; Saliba, M.; Abate, A. Efficient and Stable Inorganic Perovskite Solar Cells Manufactured by Pulsed Flash Infrared Annealing. *Adv. Energy Mater.* **2018**, *8*, 1802060.
(6) Wang, Z.; Lin, Q.; Wenger, B.; Christoforo, M. G.; Lin, Y. H.; Klug, M. T.; Johnston, M. B.; Herz, L. M.; Snaith, H. J. Publisher Correction: High Irradiance Performance of Metal Halide Perovskites for Concentrator Photovoltaics. *Nat. Energy* **2018**, *3*, 1013.
(7) Misra, R. K.; Aharon, S.; Li, B.; Mogilyansky, D.; Visoly-Fisher, I.; Etgar, L.; Katz, E. a. Temperature- and Component-Dependent Degradation of Perovskite Photovoltaic Materials under Concentrated Sunlight. *J. Phys. Chem. Lett.* **2015**, *6*, 326−330.
(8) Yang, J.; Siempelkamp, B. D.; Liu, D.; Kelly, T. L. Investigation of $CH_3NH_3PbI_3$ degradation Rates and Mechanisms in Controlled Humidity Environments Using in Situ Techniques. *ACS Nano* **2015**, *9* (2), 1955−1963.
(9) Niu, G.; Li, W.; Meng, F.; Wang, L.; Dong, H.; Qiu, Y. Study on the Stability of $CH_3NH_3PbI_3$ Films and the Effect of Post-Modification by Aluminum Oxide in All-Solid-State Hybrid Solar Cells. *J. Mater. Chem. A* **2014**, *2* (3), 705−710.
(10) Nickel, N. H.; Lang, F.; Brus, V. V.; Shargaieva, O.; Rappich, J. Unraveling the Light-Induced Degradation Mechanisms of $CH_3NH_3PbI_3$ Perovskite Films. *Adv. Electron. Mater.* **2017**, *3*, 1700158.
(11) Merdasa, A.; Bag, M.; Tian, Y.; Källman, E.; Dobrovolsky, A.; Scheblykin, I. G. Super-Resolution Luminescence Micro-Spectroscopy Reveals Mechanism of Photo-Induced Degradation in $CH_3NH_3PbI_3$ Perovskite Nano-Crystals. *J. Phys. Chem. C* **2016**, *120*, 10711−10719.
(12) Khenkin, M. V.; K. M., A.; Visoly-Fisher, I.; Kolusheva, S.; Galagan, Y.; Di Giacomo, F.; Vukovic, O.; Patil, B. R.; Sherafatipour, G.; Turkovic, V.; et al. Dynamics of Photoinduced Degradation of Perovskite Photovoltaics: From Reversible to Irreversible Processes. *ACS Appl. Energy Mater.* **2018**, *1*, 799−806.
(13) Yuan, H.; Debroye, E.; Janssen, K.; Naiki, H.; Steuwe, C.; Lu, G.; Moris, M.; Orgiu, E.; Uji-I, H.; De Schryver, F.; et al. Degradation of Methylammonium Lead Iodide Perovskite Structures through Light and Electron Beam Driven Ion Migration. *J. Phys. Chem. Lett.* **2016**, *7* (3), 561−566.
(14) Motoki, K.; Miyazawa, Y.; Kobayashi, D.; Ikegami, M.; Miyasaka, T.; Yamamoto, T.; Hirose, K. Degradation of $CH_3NH_3PbI_3$ perovskite Due to Soft X-Ray Irradiation as Analyzed by an X-Ray Photoelectron Spectroscopy Time-Dependent Measurement Method. *J. Appl. Phys.* **2017**, *121* (8), 085501.
(15) Supasai, T.; Rujisamphan, N.; Ullrich, K.; Chemseddine, A.; Dittrich, T. Formation of a Passivating $CH_3NH_3PbI_3/PbI_2$ Interface during Moderate Heating of $CH_3NH_3PbI_3$ Layers. *Appl. Phys. Lett.* **2013**, *103*, 183906.
(16) Chen, Q.; Zhou, H.; Song, T.-B.; Luo, S.; Hong, Z.; Duan, H. S.; Dou, L.; Liu, Y.; Yang, Y. Controllable Self-Induced Passivation of Hybrid Lead Iodide Perovskites toward High Performance Solar Cells. *Nano Lett.* **2014**, *14* (7), 4158−4163.
(17) Cao, D. H.; Stoumpos, C. C.; Malliakas, C. D.; Katz, M. J.; Farha, O. K.; Hupp, J. T.; Kanatzidis, M. G. Remnant PbI_2, an Unforeseen Necessity in High-Efficiency Hybrid Perovskite-Based Solar Cells? *APL Mater.* **2014**, *2* (9), No. 091101.
(18) Somsongkul, V.; Lang, F.; Jeong, A. R.; Rusu, M.; Arunchaiya, M.; Dittrich, T. Hole Blocking $PbI_2/CH_3NH_3PbI_3$ Interface. *Phys. Status Solidi RRL* **2014**, *08* (09), 763−766.
(19) Calloni, A.; Abate, A.; Bussetti, G.; Berti, G.; Yivlialin, R.; Ciccacci, F.; Duò, L. Stability of Organic Cations in Solution-Processed $CH_3NH_3PbI_3$ Perovskites: Formation of Modified Surface Layers. *J. Phys. Chem. C* **2015**, *119* (37), 21329−21335.
(20) Park, B.-w.; Kedem, N.; Kulbak, M.; Lee, D. Y.; Yang, W. S.; Jeon, N. J.; Seo, J.; Kim, G.; Kim, K. J.; Shin, T. J.; et al. Understanding How Excess Lead Iodide Precursor Improves Halide Perovskite Solar Cell Performance. *Nat. Commun.* **2018**, *9*, 3301.
(21) Kim, Y. C.; Jeon, N. J.; Noh, J. H.; Yang, W. S.; Seo, J.; Yun, J. S.; Ho-baillie, A.; Huang, S.; Green, M. A.; Seidel, J.; et al. Beneficial Effects of PbI_2 Incorporated in Organo-Lead Halide Perovskite Solar Cells. *Adv. Energy Mater.* **2016**, *6*, 1502104.
(22) Roldán-Carmona, C.; Gratia, P.; Zimmermann, I.; Grancini, G.; Gao, P.; Graetzel, M.; Nazeeruddin, M. K. High Efficiency Methylammonium Lead Triiodide Perovskite Solar Cells: The Relevance of Non-Stoichiometric Precursors. *Energy Environ. Sci.* **2015**, *8* (12), 3550−3556.
(23) Lee, Y. H.; Luo, J.; Humphry-Baker, R.; Gao, P.; Grätzel, M.; Nazeeruddin, M. K. Unraveling the Reasons for Efficiency Loss in Perovskite Solar Cells. *Adv. Funct. Mater.* **2015**, *25* (25), 3925−3933.
(24) Jacobsson, T. J.; Correa-Baena, J. P.; Halvani Anaraki, E.; Philippe, B.; Stranks, S. D.; Bouduban, M. E. F.; Tress, W.; Schenk, K.; Teuscher, J.; Moser, J. E.; et al. Unreacted PbI_2 as a Double-Edged Sword for Enhancing the Performance of Perovskite Solar Cells. *J. Am. Chem. Soc.* **2016**, *138* (32), 10331−10343.
(25) Hsu, H. Y.; Ji, L.; Du, M.; Zhao, J.; Yu, E. T.; Bard, A. J. Optimization of $PbI_2/MAPbI_3$ Perovskite Composites by Scanning Electrochemical Microscopy. *J. Phys. Chem. C* **2016**, *120* (35), 19890−19895.
(26) Gujar, T. P.; Unger, T.; Schönleber, A.; Fried, M.; Panzer, F.; van Smaalen, S.; Köhler, A.; Thelakkat, M. The Role of PbI_2 on $CH_3NH_3PbI_3$ Perovskite Stability, Solar Cell Parameters and Device Degradation. *Phys. Chem. Chem. Phys.* **2018**, *20*, 605−614.
(27) Adhikari, N.; Dubey, A.; Khatiwada, D.; Mitul, A. F.; Wang, Q.; Venkatesan, S.; Iefanova, A.; Zai, J.; Qian, X.; Kumar, M.; et al. Interfacial Study to Suppress Charge Carrier Recombination for High Efficiency Perovskite Solar Cells. *ACS Appl. Mater. Interfaces* **2015**, *7* (48), 26445−26454.
(28) Wang, S.; Dong, W.; Fang, X.; Zhang, Q.; Zhou, S.; Deng, Z.; Tao, R.; Shao, J.; Xia, R.; Song, C.; et al. Credible Evidence for the Passivation Effect of Remnant PbI_2 in $CH_3NH_3PbI_3$ Films in Improving the Performance of Perovskite Solar Cells. *Nanoscale* **2016**, *8* (12), 6600−6608.
(29) Ma, Y.; Vashishtha, P.; Chen, K.; Peach, E. L.; Ohayon, D.; Hodgkiss, J. M.; Halpert, J. E. Controlled Growth of $CH_3NH_3PbI_3$ Using a Dynamically Dispensed Spin-Coating Method: Improving Efficiency with a Reproducible PbI_2 Blocking Layer. *ChemSusChem* **2017**, *10* (12), 2677−2684.
(30) Kheraj, V.; Simonds, B. J.; Toshniwal, A.; Misra, S.; Peroncik, P.; Zhang, C.; Vardeny, Z. V.; Scarpulla, M. A. Using Photoluminescence to Monitor the Optoelectronic Properties of Methylammonium Lead Halide Perovskites in Light and Dark over Periods of Days. *J. Lumin.* **2018**, *194*, 353−358.
(31) Chen, S.; Wen, X.; Yun, J. S.; Huang, S.; Green, M.; Jeon, N. J.; Yang, W. S.; Noh, J. H.; Seo, J.; Seok, S. Il; et al. Spatial Distribution of Lead Iodide and Local Passivation on Organo-Lead Halide Perovskite. *ACS Appl. Mater. Interfaces* **2017**, *9* (7), 6072−6078.
(32) Wang, H.; Hao, M.; Han, J.; Yu, M.; Qin, Y.; Zhang, P.; Guo, Z.; Ai, X.-C.; Zhang, J.-P. The Adverse Effects of Excessively Remained PbI_2 on Photovoltaic Performance, Charge Separation and Trap State Properties in Mesoporous Structured Perovskite Solar Cells. *Chem. - Eur. J.* **2017**, *23*, 3986−3992.
(33) Kirchartz, T.; Krückemeier, L.; Unger, E. L. Research Update: Recombination and Open-Circuit Voltage in Lead-Halide Perovskites. *APL Mater.* **2018**, *6* (10), 100702.
(34) Stolterfoht, M.; Wolff, C. M.; Márquez, J. A.; Zhang, S.; Hages, C. J.; Rothhardt, D.; Albrecht, S.; Burn, P. L.; Meredith, P.; Unold, T.; et al. Visualization and Suppression of Interfacial Recombination for High-Efficiency Large-Area Pin Perovskite Solar Cells. *Nat. Energy* **2018**, *3*, 847−854.
(35) Tress, W.; Marinova, N.; Inganäs, O.; Nazeeruddin, M. K.; Zakeeruddin, S. M.; Graetzel, M. Predicting the Open-Circuit Voltage of $CH_3NH_3PbI_3$ Perovskite Solar Cells Using Electroluminescence

DOI: 10.1021/acsenergylett.9b00774
ACS Energy Lett. 2019, 4, 1370−1378

and Photovoltaic Quantum Efficiency Spectra: The Role of Radiative and Non-Radiative Recombination. *Adv. Energy Mater.* **2015**, *5*, 1400812.
(36) Kirchartz, T.; Rau, U. What Makes a Good Solar Cell? *Adv. Energy Mater.* **2018**, *8*, 1703385.
(37) Stranks, S. D.; Burlakov, V. M.; Leijtens, T.; Ball, J. M.; Goriely, A.; Snaith, H. J. Recombination Kinetics in Organic-Inorganic Perovskites: Excitons, Free Charge, and Subgap States. *Phys. Rev. Appl.* **2014**, *2* (3), 1−8.
(38) Stranks, S. D.; Petrozza, A. Revisiting Photocarrier Lifetimes in Photovoltaics. *Nat. Photonics* **2016**, *10* (9), 562.
(39) Melvin, A. A.; Stoichkov, V. D.; Kettle, J.; Mogilyansky, D.; Katz, E. A.; Visoly-Fisher, I. Lead Iodide as a Buffer Layer in UV-Induced Degradation of $CH_3NH_3PbI_3$ films. *Sol. Energy* **2018**, *159*, 794−799.
(40) Tian, Y.; Peter, M.; Unger, E.; Abdellah, M.; Zheng, K.; Pullerits, T.; Yartsev, A.; Sundström, V.; Scheblykin, I. G. Mechanistic Insights into Perovskite Photoluminescence Enhancement: Light Curing with Oxygen Can Boost Yield Thousandfold. *Phys. Chem. Chem. Phys.* **2015**, *17*, 24978−24987.
(41) Brenes, R.; Eames, C.; Bulović, V.; Islam, M. S.; Stranks, S. D. The Impact of Atmosphere on the Local Luminescence Properties of Metal Halide Perovskite Grains. *Adv. Mater.* **2018**, *30* (15), 1706208.
(42) Fang, H. H.; Wang, F.; Adjokatse, S.; Zhao, N.; Loi, M. A. Photoluminescence Enhancement in Formamidinium Lead Iodide Thin Films. *Adv. Funct. Mater.* **2016**, *26* (26), 4653−4659.
(43) DeQuilettes, D. W.; Zhang, W.; Burlakov, V. M.; Graham, D. J.; Leijtens, T.; Osherov, A.; Snaith, H. J.; Ginger, D. S.; Stranks, S. D.; et al. Photo-Induced Halide Redistribution in Organic−inorganic Perovskite Films. *Nat. Commun.* **2016**, *7*, 11683.
(44) Quitsch, W.-A.; deQuilettes, D. W.; Pfingsten, O.; Schmitz, A.; Ognjanovic, S.; Jariwala, S.; Koch, S.; Winterer, M.; Ginger, D. S.; Bacher, G. The Role of Excitation Energy in Photobrightening and Photodegradation of Halide Perovskite Thin Films. *J. Phys. Chem. Lett.* **2018**, *9*, 2062−2069.
(45) Wu, Y.; Islam, A.; Yang, X.; Qin, C.; Liu, J.; Zhang, K.; Peng, W.; Han, L. Retarding the Crystallization of PbI_2 for Highly Reproducible Planar-Structured Perovskite Solar Cells via Sequential Deposition. *Energy Environ. Sci.* **2014**, *7* (9), 2934−2938.
(46) Herz, L. M. Charge-Carrier Dynamics in Organic-Inorganic Metal Halide Perovskites. *Annu. Rev. Phys. Chem.* **2016**, *67* (1), 65−89.
(47) Johnston, M. B.; Herz, L. M. Hybrid Perovskites for Photovoltaics: Charge-Carrier Recombination, Diffusion, and Radiative Efficiencies. *Acc. Chem. Res.* **2016**, *49* (1), 146−154.
(48) Green, M. A.; Jiang, Y.; Soufiani, A. M.; Ho-Baillie, A. Optical Properties of Photovoltaic Organic-Inorganic Lead Halide Perovskites. *J. Phys. Chem. Lett.* **2015**, *6* (23), 4774−4785.
(49) Manser, J. S.; Kamat, P. V. Band Filling with Free Charge Carriers in Organometal Halide Perovskites. *Nat. Photonics* **2014**, *8*, 737−743.
(50) Filip, M. R.; Eperon, G. E.; Snaith, H. J.; Giustino, F. Steric Engineering of Metal-Halide Perovskites with Tunable Optical Band Gaps. *Nat. Commun.* **2014**, *5*, 5757.
(51) Herz, L. M. Charge-Carrier Mobilities in Metal Halide Perovskites: Fundamental Mechanisms and Limits. *ACS Energy Lett.* **2017**, *2* (7), 1539−1548.

DOI: 10.1021/acsenergylett.9b00774
ACS Energy Lett. 2019, 4, 1370−1378

Paper III

nature COMMUNICATIONS

ARTICLE

https://doi.org/10.1038/s41467-021-23275-w OPEN

Are Shockley-Read-Hall and ABC models valid for lead halide perovskites?

Alexander Kiligaridis[1], Pavel A. Frantsuzov[2✉], Aymen Yangui[1], Sudipta Seth[1], Jun Li[1], Qingzhi An[3], Yana Vaynzof[3✉] & Ivan G. Scheblykin[1✉]

Metal halide perovskites are an important class of emerging semiconductors. Their charge carrier dynamics is poorly understood due to limited knowledge of defect physics and charge carrier recombination mechanisms. Nevertheless, classical ABC and Shockley-Read-Hall (SRH) models are ubiquitously applied to perovskites without considering their validity. Herein, an advanced technique mapping photoluminescence quantum yield (PLQY) as a function of both the excitation pulse energy and repetition frequency is developed and employed to examine the validity of these models. While ABC and SRH fail to explain the charge dynamics in a broad range of conditions, the addition of Auger recombination and trapping to the SRH model enables a quantitative fitting of PLQY maps and low-power PL decay kinetics, and extracting trap concentrations and efficacies. However, PL kinetics at high power are too fast and cannot be explained. The proposed PLQY mapping technique is ideal for a comprehensive testing of theories and applicable to any semiconductor.

[1] Chemical Physics and NanoLund, Lund University, P.O. Box 118, Lund 22100, Sweden. [2] Voevodsky Institute of Chemical Kinetics and Combustion, Siberian Brunch of the Russian Academy of Science, Institutskaya 3, Novosibirsk 630090, Russia. [3] Integrated Center for Applied Physics and Photonic Materials (IAPP) and Centre for Advancing Electronics Dresden (CFAED), Technical University of Dresden, Dresden, Germany. ✉email: pavel.frantsuzov@gmail.com; yana.vaynzof@tu-dresden.de; ivan.scheblykin@chemphys.lu.se

Semiconducting materials often exhibit complex charge dynamics, which strongly depends on the concentration of charge carriers due to the co-existence of both linear and non-linear charge recombination mechanisms[1,2]. The emergence of novel semiconductors like metal halide perovskites (MHPs), exhibiting intriguing and often unexpected electronic properties[3–10], triggered a renewed interest in revisiting the classical textbook theories of charge recombination and the development of more complete, accurate models[11–17]. Moreover, modern technical advances in experimental and computational capabilities[4,18–21] allow for a detailed quantitative comparison between experiment and theory, far beyond what was once possible.

MHP are a novel solution-processable material class with enormous promise for application in a broad range of optoelectronic devices[22–24]. Driven in particular by their remarkable performance in photovoltaics, with power conversion efficiencies surpassing 25% demonstrated to date[25], significant research efforts have been devoted to study the fundamental electronic properties of these materials[4,5,7,13,15,18,26–30]. It was established that for many MHP compositions—with the most notable example being the methylammonium lead triiodide ($MA = CH_3NH_3^+$, also referred to as $MAPbI_3$ or MAPI)—they can be considered as classical crystalline semiconductors at room temperature, in which photoexcitation leads to the formation of charge carriers that exist independently from each other due to the low exciton binding energy[30]. Consequently, conventional models that describe the charge carrier dynamics are ubiquitously used to describe the dynamics of charge carriers in MHPs[11,13–15,31–39].

Historically, the first model describing the kinetics of charge carrier concentrations in a semiconductor was proposed by Shockley and Read[40] and independently by Hall[41], and is known as the Shockley–Read–Hall (SRH) model. This model considers only the first-order process (trapping of electrons or holes) and the second-order kinetic processes (radiative electron–hole recombination and non-radiative (NR) recombination of the trapped electrons and free holes). It is noteworthy that the SRH model allows the concentrations of free charge carriers to differ due to the presence of trapping. In an intrinsic semiconductor, trapping of, for example, electrons generated by photoexcitation creates an excess of free holes at the valence band. This effect is often referred to as photodoping, in analogy with chemical doping, with the important difference, however, that the material becomes doped only under light irradiation and the degree of doping depends on the light irradiation intensity.

Third-order processes, such as NR Auger recombination, via which two charge carriers recombine in the presence of a third charge that uptakes the released energy, have been recognized as particularly important at a high charge carrier concentration regime. To account for this process, Shen et al., instead of adding the Auger recombination term into the SRH model, proposed a simplified ABC model named after the coefficients A, B and C for the first-order (monomolecular), second-order (bi-molecular) and third-order Auger recombination, respectively[42]. These coefficients are also sometimes referred to as k_1, k_2 and k_3. Importantly, the concentrations of free electrons and holes in the ABC model are assumed to be equal, thus neglecting the possible influences of chemical and photodoping effects. The ABC model is widely applied in a broad range of semiconductors and in particular, is commonly used to rationalize properties and efficiency limits of LEDs[42,43]. The simplicity of the ABC model led to its extreme popularity also for MHPs (see e.g. ref. [15] and references therein) with fewer reports employing SRH or its modifications[13,14,16,17,31,36,39,44,45].

The ABC and SRH kinetic models are typically employed to describe experimentally acquired data such as the excitation power density dependence of photoluminescence (PL) quantum yield (PLQY) measured upon continuous wave (CW) or pulsed excitation, time-resolved PL decay kinetics and kinetics of the transient absorption signal. These models are applied to semi-quantitatively explain the experimental results and extract different rate constants[13–15,20,31–34,46,47], often without necessarily considering the models' limitations. Despite the very large number of published studies describing electronic processes in MHPs using the terminology of classical semiconductor physics, to the best of our knowledge, there have been only very few attempts to fit both PL decay and PLQY dependencies of excitation power using ABC/SRH-based models or at least compare the experimental data with theory[14,16,17,31,39]. These attempts, however, were of limited success because large discrepancies between the experimental results and the theoretical fits were often permitted.

These observations raise fundamental questions concerning the general validity of the SRH and ABC models to MHPs and the existence of a straightforward experimental method to evaluate this validity. To address these concerns, it is necessary to characterize experimentally the PLQY and PL decay dynamics not only across a large range of excitation power densities, but also simultaneously over a large range of the repetition rates of the laser pulses. We note that PL is sensitive not only to the concentrations of free charge carriers but also, indirectly, to the concentration of trapped charge carriers, as the latter influence the former via charge neutrality. Such trapped carriers may also lead to other non-linear processes, for example, between free and trapped charge carriers (Auger trapping[2]), which should also be considered, but are excluded from both the ABC and classical SRH models. To expose and probe these processes, it is most crucial to scan the laser repetition rate frequency in the PLQY measurements, with such measurements, to the best of our knowledge, have not been reported to date.

In this work, we developed a new experimental methodology that maps the external PLQY in two-dimensional space as a function of both the excitation pulse fluence (P, in photons/cm^2) and excitation pulse frequency (f, in Hz). Due to scanning of the excitation pulse frequency over a very broad range, this novel technique allows to unambiguously determine the excitation regime of the sample (single pulse vs. quasi-CW), which is critically important for data interpretation and modelling. Obtaining a two-dimensional PLQY(f,P) map complemented with PL decays provides a clear and unambiguous criterion to test kinetic models: a model is valid if the entire multi-parameter data set can be fitted with fixed model parameters.

By applying this method to a series of high-quality $MAPbI_3$ thin film samples, which when integrated in photovoltaic devices reach power conversion efficiencies of >20% (Supplementary Note 5), we demonstrate that despite $MAPbI_3$ being extensively studied in numerous publications before, neither ABC nor classical SRH model can fit the acquired PLQY maps across the entire excitation parameter space. To tackle this issue, we develop an enhanced SRH model (in the following, the SRH+ model), which accounts for Auger recombination and Auger trapping processes and demonstrates that SRH+ is able to describe and quantitatively fit the PLQY(f,P) maps over the entire range of excitation conditions with excellent accuracy. PL decays can be also fitted, albeit, with more moderate accuracy. The application of the SRH+ model allowed us to extract the concentration of dominant traps in high electronic quality $MAPbI_3$ films to be of the order of 10^{15} cm^3 and to demonstrate that surface treatments can create a different type of trapping states of much higher concentration. Beyond the quantitative success of the extended SRH+ model, we reveal that even this model is not capable to describe the PL decay at high charge carrier concentrations. This means that there must be

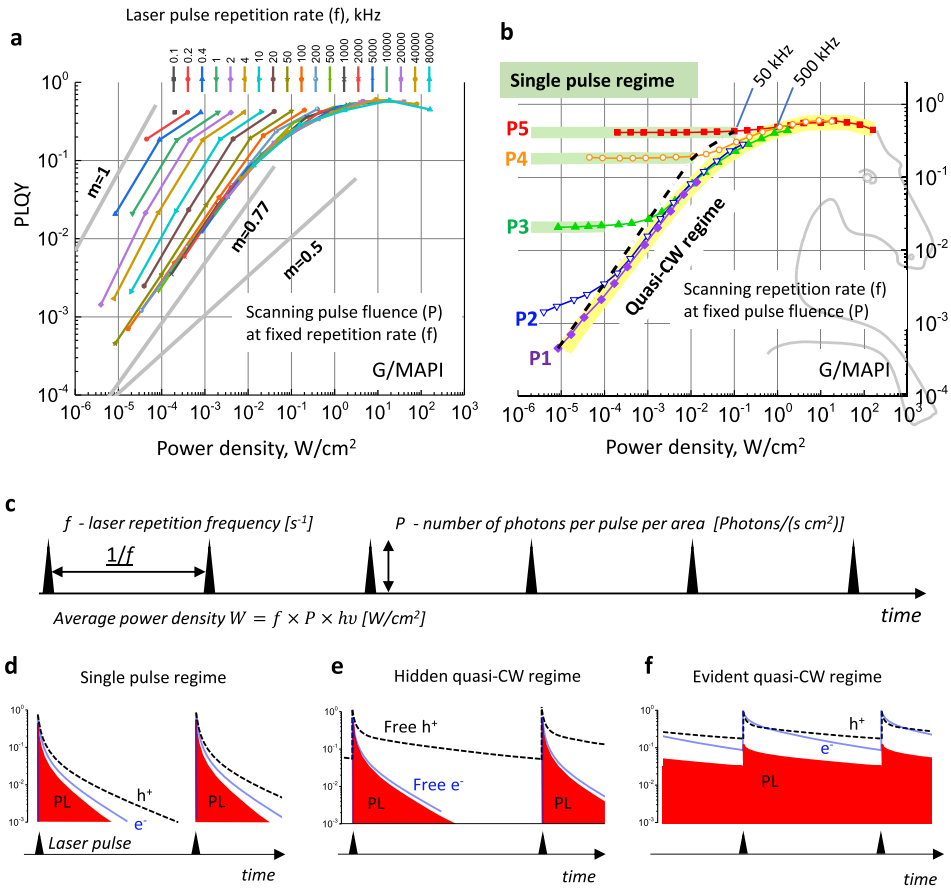

Fig. 1 PLQY(*f*,*P*) map and illustration of the difference between scanning the pulse repetition rate (*f*) and scanning of the pulse fluence (*P*). **a** PLQY (W) dependence plotted in the traditional way (*P*-scanning) for 19 different pulse repetition rates. The datapoints measured at the same frequency are connected by lines, the sample is $MAPbI_3$ film grown on glass (G/MAPI). The apparent slope of these dependencies (*m*, PLQY ~ W^m) depends on the range of *W* and the value of *f* and can be anything from 1 to 0.77 for this particular sample. **b** The same data plotted in the form of a PLQY(*f*,*P*) map where data points measured at the same pulse energy (*P*1, *P*2, ..., *P*5) are connected by lines (*f*-scanning). Data points measured at 50 kHz frequencies are connected by a dashed-dotted line. **c** The excitation scheme. Illustrations of PL decays in the single pulse (**d**) and quasi-CW (**e**, **f**) excitation regimes. Here e^- trapping is assumed leading to h^+ photodoping.

further non-linear mechanisms that influence charge dynamics at high charge carrier concentrations in $MAPbI_3$. Therefore, further theoretical work is necessary to identify the additional physical process or processes which must be considered in order to completely elucidate the charge dynamics in $MAPbI_3$.

Results

PLQY(*f*,*P*) mapping and elucidation of the excitation regime. The acquisition of a PLQY(*f*,*P*) map occurs by measuring the intensity of PL as a function of pulse repetition rate (f, s^{-1}) for a series of fixed pulse fluences (P, photons/cm^2). PL intensity is then plotted as a function of the time-averaged excitation power density $W = fPh\nu$ (W/cm^2), where $h\nu$ is the excitation photon energy, see further details in Supplementary Notes 1–3. Figure 1b presents PLQY(*f*,*P*) map for a bare $MAPbI_3$ film, while Fig. 1a presents the same data in the traditional way as a series of PLQY (*W*) dependencies for different frequencies. We use 19 frequencies ranging from 100 Hz to 80 MHz, which corresponds to a lag between pulses varying from 10 ms to 12.5 ns. In our experiments after scanning the frequency for a certain value of *P*, it is then changed to the next value and the scanning procedure is repeated. The pulse fluence ranges over four orders of magnitude ($P1 = 4.1 \times 10^8$, $P2 = 4.9 \times 10^9$, $P3 = 5.1 \times 10^{10}$, $P4 = 5.5 \times 10^{11}$ and $P5 = 4.9 \times 10^{12}$ photons/cm^2). Such fluences, in the single-pulse excitation regime (see below), correspond to charge carrier densities of 1.04×10^{13}, 1.24×10^{14}, 1.3×10^{15}, 1.37×10^{16} and 1.24×10^{17} cm^{-3}, respectively. For clarity, in Fig. 1 and in all the

following figures in the manuscript, the data points measured at the same pulse fluence P are shown by the same colour: $P1$—violet, $P2$—blue, $P3$—green, $P4$—orange, $P5$—red. The family of lines connecting points with $P =$ constant and f scanned make together a pattern that resembles "a horse neck with mane" as illustrated in Fig. 1b.

The acquisition of a PLQY(f,P) map is fully automated (Supplementary Note 2) and includes precaution measures that minimize the exposure of the sample to light, while controlling for photo-brightening or darkening of the samples (Supplementary Note 4). Such measures ensure that PLQY maps are fully reproducible when re-measured again on the same spot (see Supplementary Fig. 4.2). These precautions were absolutely necessary for obtaining a consistent data set, because light-assisted transformation of defect states due to ion migration may significantly influence the photophysics of perovskite materials[10,48,49] making any theoretical analysis unfeasible. We also note that the high degree of uniformity of our samples leads to very similar PLQY maps being measured on different areas of the sample (see Supplementary Notes 2 and 4).

PLQY(f,P) map for bare $MAPbI_3$ samples (G/MAPI) is presented in Fig. 1. A traditional representation of these data is shown in Fig. 1a, which displays a series of PLQY(W) curves—each for one of the 19 different repetition rates used in our experiment. Overall, such representation shows only minor differences between the curves, in terms of their slope and curvatures, apart from a noticeable horizontal shift at sufficiently low frequencies. By approximating the PLQY to vary as W^m over a limited power interval, we observe that the slope m varies between 0.77 at high repetition rates to approximately 1 at low repetition rates for this sample. Traditional representations of PLQY(W) plots for the other samples investigated in our study are shown in Supplementary Note 8, where, for example, a PMMA coated $MAPbI_3$ sample shows the slope m ranging from 0.5 to 1 (see Supplementary Fig. 8.1c). Such a traditional representation of the PLQY(f,P) map does not offer a clear interpretation of the data, making it difficult to elucidate the charge carrier dynamics.

An alternative representation of the PLQY(f,P) map is shown in Fig. 1b, in which the data points for each laser fluence P are presented as a single curve. Interestingly, the data points for each value of P follow a characteristic line with a specific shape. At low frequencies, and especially at high fluences, the curves are rather horizontal, yet once the frequency f exceeds a certain value, all data points start to follow a certain common dependency, at which the PLQY depends solely on the averaged power density $W = fPh\nu$. The frequency at which this happens depends on P, such that, for example, the data obtained at pulse fluence P5 joins at ca. 500 kHz, while the data collected at P1 joins at below 50 kHz (see Fig. 1b).

Critically, such presentation of the PLQY(f,P) map allows us to immediately distinguish between two principally different excitation regimes for a semiconductor:

1. *Single-pulse regime*: In this regime the repetition rate of the laser is so low, that PLQY values and PL decays do not depend on the lag between consecutive laser pulses. In other words, the excited state population created by one pulse had enough time to decay to such a low level, that it does not influence the decay of the population generated by the next pulse (Fig. 1d). In this case, PLQY does not depend on the lag between pulses (i.e. the pulse frequency). This regime is observed when PLQY follows the horizontal lines upon frequency scanning (highlighted in green in Fig. 1b).
2. *Quasi-continuous wave (quasi-CW) regime*: In this regime, the decay of the population generated by one pulse is dependent on the history of the excitations by previous pulses. This happens when some essential excited species did not decay completely during the lag time between the laser pulses (Fig. 1e, f). In this regime, the data points follow the same trend and fall on the line highlighted in yellow in Fig. 1b. The transition between the two regimes occurs when the data points at fixed values of P start to match with each other upon increasing the f.

Examining the vast literature of MHPs reveals that, to the best of our knowledge, no study has utilized such a broad range of pulse repetition rates f when measuring PLQY(W). Without scanning of f over a significant range of values, a distinction between the single pulse and quasi-CW regimes is not possible, and this reflects the current situation in the literature where the standard scanning over P is implemented with, at best, a few different repetition rates of a pulsed laser, which is sometimes complemented by excitation by a CW laser[16,17,39]. For example, Trimpl et al.[39] studied $FA_{0.95}Cs_{0.05}PbI_3$ with the focus on temperature-dependent PL decay kinetics measured at three repetition rates (61.5, 250, and 1000 kHz) and PLQY at one repetition rate and three pulse fluences approximately corresponding to P2, P3 and P4 in our experiments. A qualitative similarity between PLQY predicted from PL decay kinetics and experiments data was obtained and temperature dependence of the model parameters was extracted. The condition for charge accumulation (photodoping) in this work was addressed solely using PL decays where an initial fast drop at the ns time scale clearly visible at low temperature was assigned to trapping[39]. In another example, Kudriashova et al. studied PL decay over a quite broad pulse repetition rate range (10 kHz–10 MHz) in order to distinguish between surface and bulk charge recombination in $MAPbI_3$ films with charge transport layers, however, PLQY was not measured in this study[34]. In general, these studies addressed the important question of the excitation regime within the limits of their experimental approaches, however, the only robust way to clarify the excitation condition for a given pulse fluence is to explicitly scan f while detecting PLQY. One may assume that choosing a low repetition rate guarantees that the excitation is in the single-pulse regime. However, this is not true. As Fig. 1a and b show, if the system is at the single-pulse regime at a high pulse fluence at a given repetition rate, there is always such low pulse energy that the excitation regime becomes quasi-CW. The cause for this effect is the presence of a non-exponential decay of the excited state population as will be discussed later. Thus, at a very low repetition rate, the excitation may still be in a quasi-CW regime so long as the pulse fluence is low enough. Without scanning the pulse frequency, this cannot be disentangled. To illustrate this, the data points measured at 50 Hz were connected by a dash-dot line in the PLQY(f,P) map in Fig. 1b. For a pulse fluence $P1$ (i.e. the lowest fluence), the excitation regime is quasi-CW. Increasing the pulse fluence by an order of magnitude ($P2$) brings the system close to the single-pulse regime, with further increase of the pulse fluence ($P3$, $P4$ and $P5$) making the excitation fall purely in the single-pulse regime. We highlight the existence of a rather extended intermediate region, at which the regime is neither a single pulse nor quasi-CW. For example, for the pulse fluence $P2$ (charge carrier concentration $\approx 10^{14}\,cm^{-3}$), this intermediate region starts at 50 kHz and continues down to at least 2 kHz. We underscore that in order to identify the excitation regime without any additional assumptions, one must scan the pulse frequency and measure PLQY. As a result, the PLQY(f,P) mapping technique described here allows for an unambiguous and very easy discernment between the single pulse and quasi-CW excitation regimes.

PLQY(f,P) maps and PL decays(f,P) of polycrystalline $MAPbI_3$. Figure 2 compares the PLQY(f,P) maps measured for $MAPbI_3$

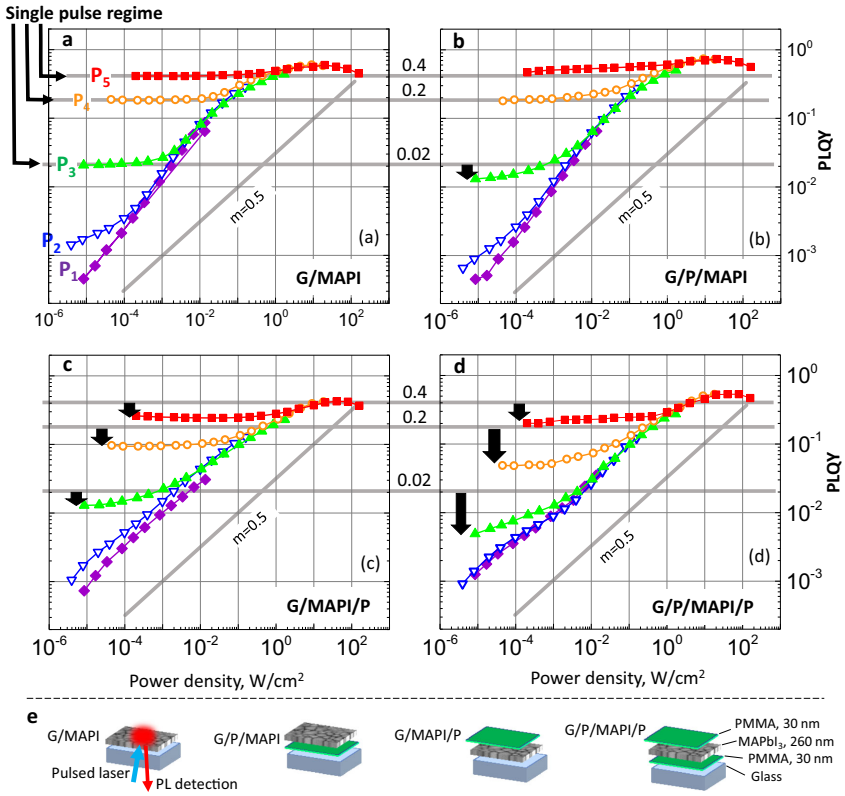

Fig. 2 PLQY maps of the samples under study plotted in the same scale for comparison. **a** Glass/MAPI, **b** glass/PMMA/MAPI, **c** glass/MAPI/PMMA, and **d** glass/PMMA/MAPI/PMMA. The horizontal grey lines show the values of PLQY (0.4, 0.2 and 0.02) in the single-pulse regime for the glass/MAPI sample (**a**) to set the benchmarks. Deviations from these values for other samples are shown by black arrows. The tilted grey line is the $W^{0.5}$ dependence as predicted by the SRH model. It is shown to see better the difference in the quasi-CW regime from sample to sample. The pulse fluence (*P*1–*P*5) is indicated by the same colour code (shown in **a**) for all PLQY maps. Panel **e** shows the structure of the samples and geometry of the measurements.

films prepared with four different combinations of the interfaces (Fig. 2e and Supplementary Note 5): $MAPbI_3$ deposited on glass (G/MAPI), $MAPbI_3$ deposited on PMMA-coated glass (G/P/MAPI), $MAPbI_3$ deposited on glass and coated with PMMA (G/MAPI/P) and $MAPbI_3$ deposited on PMMA/glass and then coated by PMMA (G/P/MAPI/P). All samples exhibit the same PL and absorption spectra (Supplementary Note 6). Scanning electron microscopy (SEM) images show that all samples exhibit a very similar microstructure, which is not affected by the presence of PMMA layers (Supplementary Note 6). Despite all these similarities, the PLQY(*f*,*P*) maps are clearly different. To emphasize the differences, we added three horizontal lines that mark the PLQY at the single pulse regimes for the pulse fluences P3, P4, and P5 for the G/MAPI sample in Fig. 1a. Black arrows highlight the reduction in PLQY in the single pulse regimes when compared with G/MAPI sample.

The decrease of PLQY upon the addition of PMMA differs for different values of *P*. Moreover, when comparing the slope *m* of the quasi-CW region in (a) and (b) with that of (c) and (d), it is evident that it is strongly influenced by the exact sample stack. To visualize this difference, a line with the slope of $m = 0.5$ (i.e. PLQY ~ $W^{0.5}$) is shown in each plot. The PLQY(*f*,*P*) map is most affected when $MAPbI_3$ film is coated by PMMA, while its presence at the interface with the glass substrate has only a minor effect.

Similar to the PLQY maps, PL decay kinetics also depends on the pulse fluence and excitation regime (single pulse vs. quasi-CW). Such kinetics should be considered together with PLQY(*f*,*P*) map to complete the physical picture of charge recombination. Figure 3 shows PL decays measured at $f = 100$ kHz and pulse fluences P2 (low) and P5 (high). $MAPbI_3$ films deposited on glass (G/MAPI) exhibit the slowest of all PL decay kinetics both at a low and a high pulse fluences. The addition of PMMA to the sample stack accelerates the PL decay with the shortest decays observed for G/P/MAPI/P samples.

The observation that modification of the sample interfaces by PMMA results in a faster PL decay not only for the low, but also for the high (*P*5) pulse fluence is particularly interesting. While the influence of surface modification on NR recombination at low charge carrier concentrations is expected due to the changes in trapping, the same is not expected to occur at high pulse fluences. It is generally considered that at such fluences, the decays will be

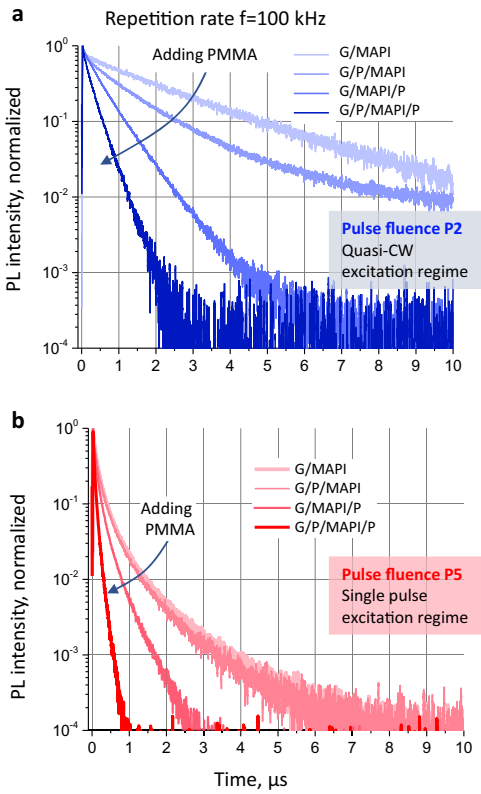

Fig. 3 PL decays of all samples at 100 kHz repetition rate (10 µs distance between the laser pulses). a Low pulse fluence (P2). **b** High pulse fluence (P5). Note that all decays in **a** are in the quasi-CW excitation regime, while all decays in **b** are in the single-pulse excitation regime. Adding PMMA accelerates the PL decay.

solely determined by non-linear processes such as Auger recombination and are thus not influenced by surface treatments. However, the change in decay dynamics in PMMA interfaced $MAPbI_3$ serves as the first indication that additional non-linear processes that involve trap states must be at play.

The second interesting observation is that according to the PLQY(*f*,*P*) map, the repetition frequency 100 kHz used for the PL decay measurements falls in the quasi-CW excitation regime for the low pulse fluence *P*2, but in the single-pulse excitation regime for high pulse fluence P5. It is remarkable, however, that the PL intensity in the quasi-CW regime (Fig. 3a) decays until the next laser pulse by almost two orders of magnitude for $MAPbI_3$ without PMMA and by four orders of magnitude for the sample coated with PMMA. This is an excellent example for the inability to correctly assign the excitation with *P*2 fluence to the quasi-CW excitation regime without the knowledge gained from the PLQY (*f*,*P*) map, considering the population observed in the PL kinetics decays completely prior to the arrival of the next pulse. The cause for the quasi-CW regime, in this case, is the presence of a population of trapped carriers which lives much longer than 10 microseconds and that influences the dynamics via photodoping[9,13,14]. This example illustrates the 'hidden quasi-CW regime' shown schematically in Fig. 1e (see also Supplementary Note 7). These effects will be quantitatively explained by the theory detailed in the next section.

Theory and modelling

Kinetic models: from ABC and SRH to SRH+. Figure 4a schematically illustrates the key processes included in the ABC, SRH and extended SRH (SRH+) kinetic models. The SRH+ model contains terms for radiative (second-order $k_r np$) and NR (all other terms) recombination of charge carriers. Note, that the processes included in the SRH+ model also naturally include photon re-absorption and recycling as discussed in detail in Supplementary Note 9.1 and Supplementary Note 10 leading to effective renormalization of k_r and k_E rate constants. NR recombination occurs via a trap state or due to Auger recombination. The trapping process can be linear and quadratic (Auger trapping). We note that we consider only one type of band-gap states. It is assumed that these states are placed above the Fermi level (electron traps), but that they are deep enough to make thermally activated de-trapping negligible. Similarly, one could consider hole traps instead under the same conditions—the equations are symmetric in this regard. Auger trapping refers to the process by which the trapping of a photoexcited electron provides excess energy to an adjacent photoexcited hole[2]. The possible importance of this process in perovskites has been suggested in a few publications[46,50]. The complete set of equations and additional description is provided in Supplementary Note 9. We note that in the SRH and SRH+ models, the complete set of equations for free and trapped charged carriers is solved, contrary to the studies where equations for only one of the charge carriers (e.g. electrons) are used (see ref. [44]). The latter simplification can work only if the concentration of holes is very large and constant (for example, in the case of chemical doping) which is not applicable for intrinsic $MAPbI_3$ and other perovskites, see also below. Due to the inclusion of Auger trapping in the SRH+ model, setting the parameter k_n to infinity reduces it to the ABC model (see Supplementary Note 9.6), where the coefficient *B* contains both radiative and NR contributions. Finally, the SRH+ model reduces to the SRH model by ignoring all Auger processes.

In the considered models the origin of the difference in the concentration of free electrons and holes is the trapping of one of the charge carriers, i.e. photodoping. We do not assume any unintentional chemical doping[45], and this assumption is supported by solid experimental evidence. Indeed, in the case of chemical doping and the presence of electron traps, the PLQY(*W*) in the quasi-CW regime should change from its square root dependence on *W* to either linear (n-doping) or become independent of *W* (p-doping) upon further decreasing of *W* (see Supplementary Note 8). Note also that the situation is symmetrical relative to the type of traps in the material. This behaviour, however, was never observed in our samples where PLQY $\propto W^m$ at low excitation power with the slope *m* being either 0.5 or 0.77, depending on the sample, without changing upon decreasing of *W* (Figs. 1 and 2). This means, that even if there was unintentional doping in our samples, its level was so low, that we do not observe any of its effects in the PLQY(*f*,*P*) maps (Supplementary Note 9.7).

Photon reabsorption and recycling are considered to be important processes influencing the charge dynamics in MHPs[11,46]. In our experimental study, we compare samples of very similar geometries and microstructure ensuring that the effects of photon reabsorption/recycling remain similar, such that they cannot serve as the reasons for the differences between PLQY(*f*,*P*) maps and PL decay kinetics amongst the different samples. As we discuss in detail

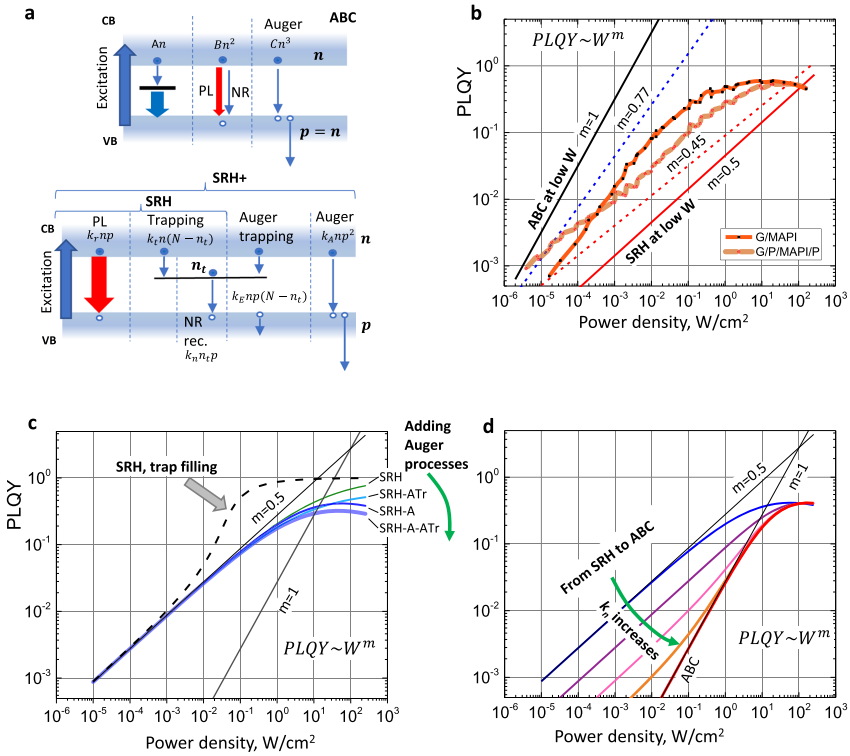

Fig. 4 CW regimes of the ABC, SRH and SRH+ models and their comparison with the experiment. a The energy level scheme, the processes and parameters of all models (see the text and Supplementary Note 9 for details). **b** The experimental dependence (G/MAPI and G/P/MAPI/P samples) of PLQY on the excitation power density W in the quasi-CW excitation regime, m is the exponent in the dependence W^m. **c** PLQY(W) in the CW regime for different models and trap feeling conditions. "-A"— adding Auger recombination, "-ATr"—adding Auger trapping (Supplementary Note 11). **d** Evolution of the PLQY(W) upon the transformation of the SRH model with Auger recombination to the ABC model with increasing of the parameter k_n (see Supplementary Note 11 for the model parameters).

in Supplementary Note 10, effects on the charge dynamics related to photon recycling in broad terms (both far-field (photon reabsorption in the perovskite) and near field (energy transfer) effects), are included in our models via renormalized radiative rate k_r and the Auger trapping coefficient k_E, respectively. We also do not explicitly include charge diffusion in the model. The rationale here is that charge carrier diffusion in $MAPbI_3$ occurs so fast that equilibrated homogeneous distribution of charge carriers over the thickness of the film can be assumed at a time scale of 10 ns and longer (Supplementary Note 9.1).

Applying the ABC, SRH and SRH+ models to the quasi-CW excitation regime. We first consider the CW excitation regime at low power densities. In this regime, the SRH and SRH+ models are identical since the contribution of Auger processes is largely negligible. Figure 4b shows the experimental dependencies of PLQY on the power density (W) for G/MAPI and G/P/MAPI/P samples and Fig. 4c and d show the dependence calculated based on the three different models.

At low power densities, the concentration n is small and PLQY is low. In the ABC model, the main contribution to the recombination rate comes from the first-order term, which is equal to the photogeneration rate. Thus, $An \propto W$ and consequently $n \propto W$. Therefore, we can write:

$$\mathrm{PLQY} = \frac{\text{flux of emitted photons}}{\text{flux of absorbed photons}} = \frac{k_r n^2}{Bn^2 + An} \approx \frac{k_r n^2}{An} = \frac{k_r n}{A} \propto W$$

In the SRH model, at a very low excitation power density the fastest process is that of trapping of electrons. With most of the electrons trapped and $n_t \approx p$, the trapping rate is equal to the photogeneration rate $k_t nN \propto W$, and the remaining electron density $n \propto W$. The limiting step in the charge carrier kinetics is the NR recombination of the trapped electrons and holes. The rate of this process is equal to the generation rate, therefore $k_n n_t p = k_n p^2 \propto W$, and $p \propto \sqrt{W}$. Thus

$$\mathrm{PLQY} = \frac{\text{flux of emitted photons}}{\text{flux of absorbed photons}} = \frac{k_r np}{k_r np + k_n n_t p}$$
$$\approx \frac{k_r np}{k_n n_t p} = \frac{k_r n}{k_n n_t} \approx \frac{k_r n}{k_n p} \propto \sqrt{W}$$

We refer the reader to the Supplementary Note 9.6 for the detailed derivation of these equations and their applicability conditions. To summarize, at low power densities when PLQY $\ll 1$,

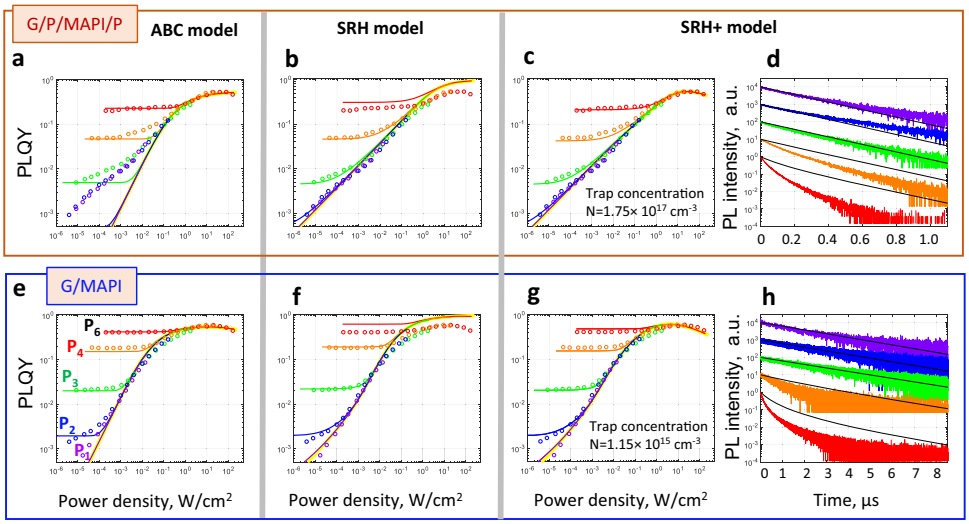

Fig. 5 Fitting of the PLQY(*f*,*P*) maps and PL decays by all models. a ABC, **b** SRH, **c** SRH+ models applied to the $MAPbI_3$ film and **e** ABC, **f** SRH, **g** SRH+ models applied to the $MAPbI_3$ film with PMMA interfaces. In PLQY maps the symbols are experimental points, the lines of the same colour are the theoretical curves. **d** and **h** show experimental and theoretical (black lines) PL decays according to the SRH+ model for both samples, laser repetition rate —100 kHz. The pulse fluences are indicated according to the colour scheme shown in **e** in the whole figure. Theoretical CW regime is shown by the yellow lines in all PLQY maps. The model parameters can be found in Supplementary Note 13.

PLQY(W) is a straight line in the double logarithmic scale (PLQY $\propto W^m$) with the slope $m = 0.5$ for the SRH and SRH+ models with no trap filling effect (see below) and $m = 1$ for the ABC model[1].

Experimentally, we observe $m \approx 0.45$ for those perovskite samples which are coated with PMMA (e.g. G/MAPI/P is shown in Fig. 4b). This value is in a good agreement to the $m = 0.5$ predicted by the SRH/SRH+ models in the case of the absence of trap filling. However, the other two samples, in which the $MAPbI_3$ surface is not coated with PMMA, exhibit $m \approx 0.77$ (e.g. G/MAPI sample is shown in Fig. 4b), which lies between the values of 1 and 0.5 predicted by the ABC and SRH/SRH+ models, respectively. These slopes are observed over at least four orders of magnitude in the excitation power density. Based on these results, we must conclude that $MAPbI_3$ samples with and without PMMA coating behave very differently in the quasi-CW regime.

In the framework of the SRH/SRH+ models, there are two possibilities that would lead to an increase in the coefficient m: (i) transformation toward the ABC model and (ii) trap filling effect in the SRH model. Figure 4d shows the transformation of the SRH model, which includes Auger recombination to the ABC model by increasing the parameter k_n. At the condition $k_n \gg k_r, k_t$ there is a limited range of excitation power where one can obtain an intermediate slope m laying between 0.5 and 1 for a limited range of W (Supplementary Notes 9.6 and 11).

The second possibility is to allow for the trap filling effect to occur at the excitation power densities which are below the saturation of the PLQY due to the radiative recombination and Auger processes. The effect of trap filling is caused when the number of available traps starts to decrease with increasing W. Consequently, the PLQY increases not only because the radiative process becomes faster (quadratic term), but also because the NR recombination (trapping and further recombination) becomes smaller. As the result, PLQY grows faster than $W^{0.5}$ over a certain range of W. The effect is not trivial, because it is not the concentration of traps N as one would think, but rather the relation of k_t to k_r and k_n (the necessary condition is $k_t \gg k_r, k_n$), which determines if the trap-filling effect is observed in PLQY maps or not (Supplementary Notes 9.6, 9.8 and 11).

The trap filling effect is illustrated in Fig. 4c, in which the parameter k_t is increased whilst maintaining all other parameters fixed. Obviously, the resulting dependence is too strong and occurs over a too narrow range of excitation power densities (one order of magnitude) to fit the experimental data directly. Nevertheless, as will be shown below, such processes are present in $MAPbI_3$ samples which are not coated with PMMA, where PLQY(W) in the quasi-CW regime deviates from the straight line bending upwards before reaching saturation at high power.

At high excitation densities, non-linear recombination processes begin to be particularly important. Since Auger processes are NR, with further increase of W the PLQY cannot reach unity and instead decreases after reaching a certain maximum. SRH cannot account for this effect considering it does not include any NR non-linear terms and leads to PLQY = 1 at high W. The ABC and SRH+ models can potentially describe this regime since they contain Auger recombination terms (Fig. 4c and d).

Fitting of the PLQY(f,P) maps and PL decays kinetics by ABC, SRH and SRH+ models. To examine the validity of the three theories, we attempt to fit the experimental PLQY(f,P) plots and PL decays using all models and the results are shown in Fig. 5. Before we discuss the fitting results, it is important to stress that each simulated value of PLQY(f,P) at the PLQY maps and each PL decay curve shown in Fig. 5 are obtained from a periodic solution of the kinetic equations of the corresponding model under pulsed excitation with the required pulse fluence P and repetition frequency f. In practice it means that we excited the system again and again until the solution PL(t) stabilizes and begins to repeat

Table 1 Comparison of the ability of the three models to describe the PLQY(*f*,*P*) maps and PL decays.

Observables/regimes	Low and medium excitation pulse fluence power density (*W* < 0.1 Sun)	High excitation power density (1-300 Sun), high pulse fluence
ABC model		
PLQY(*f*,*P*)	Quasi-CW regime—poor or very poor fit strongly depending on the sample. Good fit in the single pulse regime	Very good fit in all regimes
PL decays for given PLQY(*f*,*P*)	**Cannot predict the PL decays**	**Cannot predict the PL decays**
SRH model		
PLQY(*W*,*f*)	Very good fit in all regimes	**Discrepancy due to exclusion of high order processes**
PL decays for given PLQY(*f*,*P*)	Very good match	**Underestimation of the initial decay**
SRH+ model		
PLQY(*f*,*P*)	Very good fit in both the quasi-CW and single pulse excitation regimes	Very good fit in both the quasi-CW and single pulse excitation regimes
PL decays for given PLQY(*f*,P)	Very good match	**Underestimation of the initial decay**

Bold font emphasizes serious deficiencies of the fitting.

itself after each pulse. Details of the simulations are provided in Supplementary Note 12.

When fitting experimental data, it is important to minimize the number of fitting parameters and maximize the number of parameters explicitly calculated from the experimental data. We exploit the experimental data to extract several parameters. First, considering that in all three models, the decay of PL at low pulse fluences is determined exclusively by linear trapping and is thus mono-exponential, we can extract the parameter k_tN of the SRH and SRH+ models. Indeed, such behaviour is observed experimentally for the studied samples (see Fig. 3a) allowing us to use the decays at low pulse energies (*P*1–P3) to directly determine the trapping rates k_tN. We note, however, to obtain the best fit using the ABC model, the PL decays were not used to fix the parameter A. Secondly, in a single pulse excitation regime (i.e. the horizontal lines in the PLQY map), the magnitudes of PLQY at pulse fluence *P*3 and *P*4 allow to determine the ratio $\frac{k_r}{k_tN}$ in the SRH/SRH+ models and the ratio $\frac{k_r}{A}$ for the ABC model. Detailed block schemes of the fitting procedures are provided in Supplementary Note 12.

As has been discussed above, $MAPbI_3$ samples coated with PMMA cannot be described using the ABC model due to mismatch of the slope within the quasi-CW regime (Fig. 5a), while both SRH and SRH+ models are well-suitable in this case (Fig. 5b, c). However, at a high excitation regime (i.e. the saturated region of the quasi-CW and the single pulse regime at *P*5 pulse fluence) SRH+ works much better, highlighting the limitations of the SRH model on its own. Consequently, the entire PLQY(*f*,*P*) map of the PMMA-coated films can be fitted using the SRH+ model with excellent agreement between the theoretical and experimental data (Fig. 5c).

The behaviour of $MAPbI_3$ samples whose surface is left bare (where the PLQY(*W*) dependence in quasi-CW shows extra up-bending before reaching saturation) can be approximated using the ABC model (Fig. 5e) and well-fitted by the SRH+ (Fig. 5g) model. ABC indeed works quite well with, however, an obvious discrepancy in the tilt of the quasi-CW regime. Very good fit can be obtained by the SRH/SRH+ models by adjusting of the k_t, k_n and *N* to allow for the trap filling effect to occur in the medium excitation power range and, at the same time, making the dynamics closer to that in the ABC model by a relative increase of the recombination coefficient k_n (see the section above and Fig. 5g).

As was mentioned above, the PL decay rate at low power densities (*P*1–P3) was used to extract the product k_tN. This is the only occasion for which the PL decays are used in the fitting procedure of the SRH and SRH+ models. In the fitting procedure for the ABC model the PL decays are not used at all. Upon determining the fit parameters for each of the models, it is possible to calculate the PL decays at each condition and compare them with those decays measured experimentally. Importantly, PL decay rates calculated using the ABC model significantly underestimate the measured decay dynamics at all fluencies (Supplementary Note 13). On the other hand, as is shown in Fig. 5d and h, the SRH+ model (as well as SRH, Supplementary Note 13) fit well the low fluence decay dynamics, but systematically underestimate the decay rate at high power fluences. It is noteworthy that the mismatch of the initial decay rate at the highest pulse fluence reaches a factor ranging from three to five depending on the sample, still significantly outperforming the fit using the ABC model. Insights regarding the applicability of the ABC, SRH and SRH+ models to the PLQY maps and PL decays are summarized in Table 1, see also Supplementary Fig. 13.3.

Discussion

Scanning the excitation pulse repetition rate as proposed herein represents a novel experimental approach that transforms routine power-dependent PLQY measurements to a universal methodology for elucidating charge carrier dynamics in semiconductors. Adding the second dimension of pulse repetition rate to the standard PLQY(*W*) experiment is not just an update, it is a principle, qualitative change of the information content of the experiment. The difference between PLQY(*f*,*P*) mapping and the standard PLQY(*W*) experiment in the CW regime or at some fixed pulse repetition rate is analogous to the difference between the standard NMR spectrum and 2D NMR spectrum. In our method, we monitor not only the concentrations of free charge carriers, but also the concentration of trapped charges due to the total electro-neutrality of the system. Therefore, together with the time-resolved PL decays, the PLQY map in the repetition frequency—pulse fluence 2D parameter space comprise an experimental series which contains all the information concerning the charge dynamics in a given sample.

We stress the absolute necessity of the unambiguous determination of the excitation regime of the experiment, which would

not be possible without scanning the pulse repetition rate. For example, PL intensity decay kinetic showing the signal decay by several orders of magnitude prior to the arrival of the next laser pulse (Fig. 3a) can still be in the quasi-CW regime due to presence of long-lived trapped charges ("dark" charges). Such trapped charges cause the so-called photodoping effect, which lingers until the millisecond timescale, and thus holds the "memory" of the previous laser pulse, leading to a stark influence on the PLQY map. While the importance of distinguishing between the single pulse and quasi-CW regimes has been noted in several publications before[9,31], it has never been accomplished for MHPs experimentally. Indeed, in none of the published works presenting theoretical fits of experimental PLQY(W) dependencies was this determination possible simply because either only CW excitation[14,44] or pulse excitation with only one[17,31,39] or two (20 MHz and 250 kHz)[16] repetition rates of the laser pulses were employed.

Understanding the excitation conditions is also critically important for interpretation of the classical experiments in which the PL intensity (or PLQY) is measured as a function of excitation power density (W) using a CW light source or a pulsed laser with a fixed repetition rate. Traditionally the intensity of PL is approximated using a W^{m+1} dependence or in case PLQY is measured, with W^m (because PLQY $\propto$ PL/W), with both leading to a straight line in the double logarithmic scale[1,13,31,33,47]. According to the SRH and ABC models, approximations like these can be valid for a large range of W at low excitation power density only, when there is no trap-filling effect, Auger processes can be neglected and PLQY is far from saturation. In all other cases, the dependence is not linear in the double logarithmic scale. As discussed above, SRH predicts $m = 0.5$ in the CW excitation regime while ABC always predicts $m = 1$. However, our experiments reveal that when the excitation is pulsed, one can obtain intermediate m values because upon increasing the power density, the experimental excitation regime is almost certainly switched from a quasi-CW to a single pulse. The change of the slope can be seen in Fig. 1a and in Supplementary Note 8. Consequently, the extracted m cannot be reliably used for interpretation of the photophysics of the sample since any value of m can be obtained depending on the conditions of the pulsed excitation.

The main message of our work is that any model of charge carrier dynamics which is considered to be correct should be able to fit not only standard one-dimensional PLQY(W) data, but also the full PLQY(f,P) map and PL decays at different powers and pulse repetition rates. This criterion is strict and universally applied. With standard one-dimensional PLQY(W) data—even upon the inclusion of the PL decay data—one can find several principally different models that are capable of fitting the data. However, when the multi-dimensional data space consisted of the PLQY(f,P) map and PL decays is available, this ambiguity becomes highly unlikely.

As we have shown above, neither the standard ABC nor the SRH model are capable of describing the complete PLQY maps and predicting PL decays of the investigated $MAPbI_3$ samples. On the other hand, the addition of Auger recombination and Auger trapping processes to the SRH model (SRH+ model) leads to an excellent fit of PLQY maps of all the studied samples. We emphasize that the (f,P) space used in this work is very large with f varying from 100 Hz to 80 MHz (6 orders of magnitude) and pulse fluence P changing over 4 orders of magnitude corresponding to charge carrier densities in the single-pulse excitation regime from ca. 10^{13} to 10^{17} cm^{-3}. SRH+ model also agrees well with the PL decay kinetics for low and medium pulse energies (charge carrier concentrations from 10^{13} to 10^{15} cm^{-3}). However, for high pulse fluences (10^{16}–10^{17} cm^{-3}) the model underestimates the initial decay rate by up to a factor of five for the higher pulse energies. The Auger rates obtained from the fittings (2.8×10^{-29} cm^6 s^{-1} for the PMMA-coated $MAPbI_3$ sample and 1.7×10^{-29} cm^6 s^{-1} for the bare $MAPbI_3$) are in a reasonable agreement with theoretical estimation 7.3×10^{-29} cm^6 s^{-1} for $MAPbI_3$ from ref. [51] which is at the low limit from 2×10^{-29} to 1×10^{-27} cm^6 s^{-1} range reported in literature[52]. Note that increasing of the Auger rate constant cannot help because a fit of PL decay will result in lower PLQY than experimentally observed. Therefore, we must conclude that the SRH+ model has limitations.

One possible explanation for the mismatch of decay rates at high excitation powers might be provided by considering experimental errors. It is well documented that the PL of perovskite samples is sensitive to both illumination and environmental conditions, which, may lead to both photodarkening or photobrightening of the sample[9,48,49,53]. To account for these effects, we paid a special attention to monitoring the evolution of the sample under light irradiation throughout the entire measurement sequence. As is shown in Supplementary Note 4, the maximum change in PL intensity during the entire measurement series is smaller than a factor of two. Taking this uncertainty together with other errors inherent to absolute PLQY and excitation power density measurements, missing the decay rates by several times at the highest pulse fluence is not impossible. However, there is strong indication that the discrepancy reflects a problem of the model rather than in the experiment: the deviation between the theoretical and experimental PL decays is systematic. Experimental PL decay rates at high charge carrier concentrations are faster than predicted for all samples despite of the excellent matching of the PLQY(f,P) maps.

In our future work we are going to test several additional concepts which might help to increase the PL decay rate without a strong effect on PLQY. One of them is based on the idea that at high charge carrier density, the time (few ns) required to reach an equilibration of the charge carrier concentration over the thickness of the sample (300 nm) becomes comparable with the initial fast PL decay induced by Auger. In other words, the diffusion length becomes smaller in the high excitation regime[54]. In this case, diffusion cannot be ignored and an additional PL decay should appear reflecting the decreasing charge carrier concentration due to their diffusion from the initially excited layer determined by the excitation light penetration depth (100 nm) towards the opposite surface of the 300 nm-thick film. This process is often discussed in the context of charge carrier dynamics in large single crystals regardless of the excitation conditions[12]. Supporting this notion is the fact that in order to model a $MAPbI_3$ solar cell under operation[55], a much lower charge carrier mobility (around 10^{-2} cm^2 V s^{-1}) than that obtained spectroscopically (1–30 cm^2 V s^{-1})[15] has to be assumed, which suggests that the actual diffusion coefficient might be smaller than expected.

Another possible contributing factor originates from a local charge carrier distribution inside the sample, caused by, for example, funnelling of charge carries due to the energy landscape or/and variations of charge mobilities[13]. Presence of a small fraction of charge carriers concentrated in local nano-scale regions can lead to an apparent fast PL decay at early times, accompanied by a relatively small effect on the total PLQY. In addition, high charge concentrations may cause carrier degeneracy effects. This happens because charge carriers occupy all the possible states with energies below kT (degenerated Fermi gas). Considering that the effective density of states in perovskite materials is relatively low[56], such degeneracy effects should be seriously examined. If present, all rate constants would depend on the charge concentration, which may lead to unexpected effects.

Further investigations will reveal which of these—or other—mechanisms can help in describing of the PLQY(*f*,*P*) and PL decay data space.

Despite of the moderate success at high charge concentration regime, the results of the SRH+ fitting still significantly outperform all previous attempts to explain charge carrier dynamics in $MAPbI_3$ samples and allow us to gain valuable insights concerning the photophysics of the samples investigated herein and the roles of traps within them. This is supported by the fact that the effect of charge trapping is the most crucial in the low and middle power ranges where the SRH+ model works very well for both the PLQY maps and PL decays. Note that with the current experimental accuracy we have no reason to complicate the SRH+ model by adding another type of traps and/or thermal detrapping.

The analysis of PLQY maps reveals that the concentration of dominant traps in high-quality $MAPbI_3$ films (without PMMA coating) is ~1.2×10^{15} cm^{-3}. Very recently, practically the same value for trap concentration was obtained using impedance spectroscopy and deep-level transient spectroscopy for $MAPbI_3$ samples prepared by exactly the same method[57]. This concentration is also in excellent agreement with the range of values previously proposed by Stranks et al.[14], where the trap concentration was estimated by assuming that PL decays become non-exponential exclusively due to the trap filling. We note, however, that trap filling is not a necessary condition to observe non-exponentiality in a PL decay. For that to occur, the non-linear recombination rate (radiative, Auger, etc.) should just be faster than the trapping rate, which is determined not only by the trap concentration, but also by the capture coefficient. All these and related effects are considered when the data is modelled by the SRH+ model developed and employed here, thus allowing the extraction of the trap concentrations without any special assumptions. Note, however, that for the bare $MAPbI_3$ sample the estimation of the trap concentration is reliable, because the influence of trap concentration alone is clearly decoupled from that of the trapping constant in the regime of trap filling and conversion from the SRH to ABC model as observed for the bare $MAPbI_3$ sample at a moderate excitation power.

Several studies have established the important role that surface defects play in determining the optoelectronic properties of perovskite thin films[58–60], yet traditional PLQY measurements do not offer a reliable method to extract the defect density in perovskite films and investigate how surface modifications influence this density of defects. Considering that a PLQY(*f*,*P*) mapping allowed us to extract the density of defects in bare $MAPbI_3$ films, we apply the same analysis to the PMMA-coated samples. We find that coating the top surface of $MAPbI_3$ with PMMA changes the picture drastically in terms of both the concentration and the nature of dominant traps. No indication of trap filling is observed in the PLQY(*f*,*P*) maps, which allows us to provide only the lower estimate for the trap density in these samples ($\approx 2 \times 10^{17}$ cm^{-3} s^{-1}). The only part of the PLQY(*f*,*P*) map where the trap concentration and the trapping rate are decoupled is the region in which PLQY saturates, so the estimation of the high-limit of the trap concentration is not reliable due to dependence of this region on parameters related to the Auger processes. The strong increase in the trap concentration is accompanied by a decrease of the trapping rate constant k_t and the nonradiative recombination rate constant k_n by at least one order of magnitude. This can be interpreted by considering the traps in the PMMA-coated sample to be more prevalent, yet "weaker" than those in the bare $MAPbI_3$ sample in terms of the trapping and recombination rate introduced by each of these traps. These results suggest that the addition of PMMA at the top surface leads to the creation of weak traps, which, however, due to their very large concentration override the effect of the stronger, yet less common, traps present in $MAPbI_3$ films that did not undergo the surface treatment.

We note that coating with polymers (including PMMA) and organic molecules in general is a common method employed in literature to protect $MAPbI_3$ samples from environmental effects when performing PL studies[61,62], and also to reduce NR recombination and improve PLQY of the material[63]. Yet our results, using PMMA as an example, reveal that such a treatment fundamentally modifies the photophysics in the perovskite layer. More importantly, the supreme sensitivity of PLQY(*f*,*P*) mapping method to the influences of interfacial modifications illustrates its efficacy for studying charge carrier dynamics not only in films, but also in multilayers and complete photovoltaic devices.

Another question that remains under debate in the perovskite community is the role of bulk defects on charge carrier dynamics in perovskite films. While some reports claim that such bulk defects, found for example at the grain boundaries, do not influence charge recombination[64,65] other reports suggest such defects influence the optoelectronic quality of the perovskite layer[66,67]. Considering these contradicting reports, it is clear that traditional PLQY measurements are not capable to idenitfy the role of bulk defects. We believe that PLQY(*f*,*P*) map is the best possible fingerprint of the sample in the context of its charge recombination pathways and may aid at resolving this and other open questions in the field. We predict that this non-invasive, simple and non-expensive method will find practical applications in controlling and optimizing semiconducting materials and the devices that are based on them.

Conclusions

To summarize, we examined the validity of the commonly employed ABC and SRH kinetic models in describing the charge dynamics of metal halide perovskite $MAPbI_3$ semiconductor. For this purpose, we developed a novel experimental methodology based on PL measurements (PLQY and time resolved decays) performed in the two-dimensional space of the excitation energy and the repetition frequency of the laser pulses. The measured PLQY maps allow for an unmistakable distinction between samples, and more importantly, between the single-pulse and quasi-continuous excitation regimes.

We found that neither the ABC nor the SRH model can explain the complete PLQY maps for $MAPbI_3$ samples and predict the PL decays at the same time. Each model is valid only in a limited range of parameters, which may strongly vary between different samples. On the other hand, we show that the extension of the SRH model by the addition of Auger recombination and Auger trapping (SRH+ model) results in an excellent fit of the complete PLQY maps for all the studied samples. Nevertheless, even this extended model systematically underestimate the PL decay rates at high pulse fluences pointing towards the existence of additional processes in $MAPbI_3$ which must be considered to fully explain the charge carrier dynamics.

Our study clearly shows that neither PL decay nor PLQY data alone are sufficient to elucidate the photophysical processes in perovskite semiconductors. Instead, a combined PLQY mapping and time-resolved PL decays should be used to elucidate the excitation dynamics and energy loss mechanisms in luminescent semiconductors. Our experimental approach provides a strict criteria for testing any theoretic model of charge dynamics which is the requirement to be able to fit PLQY(*f*,*P*) map and PL decays at different powers and pulse repetition rates.

Methods

Thin film preparation. All samples were prepared from same perovskite precursor which was prepared with 1:3 molar ratio of lead acetate trihydrate and methylammonium iodide dissolved in dimethylformamide (Supplementary Note 5). For the

samples with PMMA between the glass and perovskite layer, PMMA was spin-coated on the clean substrates at 3000 rpm for 30 s and annealed at 100 °C for 10 min. The perovskite precursor was spin-coated at 2000 rpm for 60 s on glass or glass/PMMA substrates, following by a 25 s dry air blowing, a 5 min room temperature drying and a 10 min 100 °C annealing. For the samples with PMMA on top of the perovskite layer, no further annealing was applied after the PMMA deposition.

PL measurements. Photoluminescence microscopy measurements were carried out using a home-built wide-field microscope based on an inverted fluorescence microscope (Olympus IX-71) (Supplementary Note 1). We used 485 nm pulsed laser (ca. 150 ps pulse duration) driven by Sepia PDL 808 controller (PicoQuant) for excitation with repetition rate tuned from 100 Hz to 80 MHz. The laser irradiated the sample through an objective lens (Olympus ×40, NA = 0.6) with ~30 μm excitation spot size. The emission of the sample was collected by the same objective and detected by an EMCCD camera (Princeton Instruments, ProEM 512B). Two motorized neutral optical density (OD) filter wheels were used: one in the excitation beam path in order to vary the excitation fluence over 4 orders of magnitude and one in the emission path to avoid saturation of the EMCCD camera. The whole measurement of a PLQY(f,P) map was fully automated and took ~3 h (see Supplementary Note 2 for details). Automation was crucial for avoiding human errors in the measurements of so many data points (about 100 data points per PLQY(f,P) map and to minimize light exposure of the sample.

Time-resolved photoluminescence (TRPL) measurements were carried out using the same microscope, by adding a beam splitter in front of the EMCCD and redirecting a part of the emission light to a single photon counting detector (Picoquant PMA Hybrid-42) connected to a TCSPC module (Picoharp 300).

Absolute PLQY measurements were performed using a 150 mm Spectralon Integrating Sphere (Quanta-φ, Horiba) coupled through an optical fibre to a compact spectrometer (Thorlabs CCS200). Sample PL was excited by the same laser with 80 MHz excitation repetition rate and 0.01 W/cm^2 excitation power density. This reference point was then used to calculate the absolute PLQY for all pulse fluences and frequency combinations (Supplementary Notes 2 and 3).

It is important to stress that the whole acquisition of PLQY(f,P) was fully automated and the sample was exposed to light only for the measurements. This led to a rather small total irradiation dose of about 200 J/cm^2 (equivalent to 2000 s of 1 Sun power) per one PLQY(f,P) map which accumulated over 85 acquisitions during about 4 h for one PLQY map. Note, that 90% of this doze was accumulated with the maximum power P5 which gives 1600 Sun when the highest frequency 80 MHz is used. This allowed us to have minimal effects of light induced PL enhancement/bleaching on the measurements.

Data availability

The data that support the findings of this study are available from the corresponding authors upon reasonable request.

Code availability

The codes and algorithms used for data fitting are available from the corresponding authors upon reasonable request.

Received: 5 February 2021; Accepted: 1 April 2021;
Published online: 07 June 2021

References

1. Pelant, I. & Valenta, J. *Luminescence Spectroscopy of Semiconductors* (Oxford University Press, 2012).
2. Abakumov, V. N., Perel, V. I. & Yassievich, I. N. *Nonradiative Recombination in Semiconductors* (North-Holland, 1991).
3. Chu, W., Zheng, Q., Prezhdo, O. V., Zhao, J. & Saidi, W. A. Low-frequency lattice phonons in halide perovskites explain high defect tolerance toward electron-hole recombination. *Sci. Adv.* **6**, eaaw7453 (2020).
4. Rakita, Y., Lubomirsky, I. & Cahen, D. When defects become 'dynamic': halide perovskites: a new window on materials? *Mater. Horizons* **6**, 1297–1305 (2019).
5. Stranks, S. D. Nonradiative losses in metal halide perovskites. *ACS Energy Lett.* **2**, 1515–1525 (2017).
6. Manser, J. S., Christians, J. A. & Kamat, P. V. Intriguing optoelectronic properties of metal halide perovskites. *Chem. Rev.* **116**, 12956–13008 (2016).
7. Guo, Y. et al. Dynamic emission Stokes shift and liquid-like dielectric solvation of band edge carriers in lead-halide perovskites. *Nat. Commun.* **10**, 1–8 (2019).
8. Egger, D. A. et al. What remains unexplained about the properties of halide perovskites? *Adv. Mater.* **30**, 1800691 (2018).
9. Motti, S. G. et al. Defect activity in metal-halide perovskites. *Adv. Mater.* **31**, 1901183 (2019).
10. Goetz, K. P., Taylor, A. D., Paulus, F. & Vaynzof, Y. Shining light on the photoluminescence properties of metal halide perovskites. *Adv. Funct. Mater.* **30**, 1910004 (2020).
11. Dequilettes, D. W. et al. Charge-carrier recombination in halide perovskites. *Chem. Rev.* **119**, 11007–11019 (2019).
12. Wenger, B. et al. Consolidation of the optoelectronic properties of CH3NH3PbBr3 perovskite single crystals. *Nat. Commun.* **8**, 590 (2017).
13. Feldmann, S. et al. Photodoping through local charge carrier accumulation in alloyed hybrid perovskites for highly efficient luminescence. *Nat. Photonics* **14**, 123–128 (2020).
14. Stranks, S. D. et al. Recombination kinetics in organic–inorganic Perovskites: excitons, free charge, and subgap states. *Phys. Rev. Appl.* **2**, 1–8 (2014).
15. Johnston, M. B. & Herz, L. M. Hybrid Perovskites for photovoltaics: charge-carrier recombination, diffusion, and radiative efficiencies. *Acc. Chem. Res.* **49**, 146–154 (2016).
16. Manger, L. H. et al. Global analysis of Perovskite photophysics reveals importance of geminate pathways. *J. Phys. Chem. C* **121**, 1062–1071 (2017).
17. Fu, X., Weber, K. J. & White, T. P. Characterization of trap states in perovskite films by simultaneous fitting of steady-state and transient photoluminescence measurements. *J. Appl. Phys.* **124**, 073102 (2018).
18. Delport, G., Macpherson, S. & Stranks, S. D. Imaging carrier transport properties in halide perovskites using time-resolved optical microscopy. *Adv. Energy Mater.* **10**, 1903814 (2020).
19. Meggiolaro, D., Ambrosio, F., Mosconi, E., Mahata, A., & De Angelis, F. Polarons in metal halide perovskites. *Adv. Energy Mater.* **10**, 1902748 (2020).
20. DeQuilettes, D. W. et al. Tracking photoexcited carriers in hybrid perovskite semiconductors: trap-dominated spatial heterogeneity and diffusion. *ACS Nano* **11**, 11488–11496 (2017).
21. Qiao, L., Fang, W., Long, R. & Prezhdo, O. V. Photoinduced dynamics of charge carriers in metal halide perovskites from an atomistic perspective. *J. Phys. Chem. Lett.* **11**, 7066–7082 (2020).
22. Jena, A. K., Kulkarni, A. & Miyasaka, T. Halide perovskite photovoltaics: background, status, and future prospects. *Chem. Rev.* **119**, 3036–3103 (2019).
23. Dong, H., Zhang, C., Liu, X., Yao, J. & Zhao, Y. S. Materials chemistry and engineering in metal halide perovskite lasers. *Chem. Soc. Rev.* **49**, 951–982 (2020).
24. Xie, C., Liu, C. K., Loi, H. L. & Yan, F. Perovskite-based phototransistors and hybrid photodetectors. *Adv. Funct. Mater.* **30**, 1903907 (2020).
25. Research Cell Efficiency Records. *Research Cell Efficiency Records*. https://www.nrel.gov/pv/cell-efficiency.html.
26. Jones, T. W. et al. Lattice strain causes non-radiative losses in halide perovskites. *Energy Environ. Sci.* **12**, 596–606 (2019).
27. Herz, L. M. Charge-carrier mobilities in metal halide perovskites: fundamental mechanisms and limits. *ACS Energy Lett.* **2**, 1539–1548 (2017).
28. Tennyson, E. M., Doherty, T. A. S. & Stranks, S. D. Heterogeneity at multiple length scales in halide perovskite semiconductors. *Nat. Rev. Mater.* **4**, 573–587 (2019).
29. Gerhard, M. et al. Microscopic insight into non-radiative decay in perovskite semiconductors from temperature-dependent luminescence blinking. *Nat. Commun.* **10**, 1698 (2019).
30. Baranowski, M. & Plochocka, P. Excitons in metal-halide perovskites. *Adv. Energy Mater.* **10**, 1903659 (2020).
31. Saba, M. et al. Correlated electron–hole plasma in organometal perovskites. *Nat. Commun.* **5**, 5049 (2014).
32. Kang, G. et al. Electron trapping and extraction kinetics on carrier diffusion in metal halide perovskite thin films. *J. Mater. Chem. A* **7**, 25838–25844 (2019).
33. Draguta, S. et al. Spatially non-uniform trap state densities in solution-processed hybrid perovskite thin films. *J. Phys. Chem. Lett.* **7**, 715–721 (2016).
34. Kudriashova, L. G. et al. Impact of interfaces and laser repetition rate on photocarrier dynamics in lead halide perovskites. *J. Phys. Chem. Lett.* **8**, 4697–4703 (2017).
35. Srimath Kandada, A. R. et al. Nonlinear carrier interactions in lead halide perovskites and the role of defects. *J. Am. Chem. Soc.* **138**, 13604–13611 (2016).
36. Calado, P. et al. Identifying dominant recombination mechanisms in perovskite solar cells by measuring the transient ideality factor. *Phys. Rev. Appl.* **11**, 1 (2019).
37. Droseros, N. et al. Origin of the enhanced photoluminescence quantum yield in MAPbBr3 perovskite with reduced crystal size. *ACS Energy Lett.* **3**, 1458–1466 (2018).
38. Chirvony, V. S. et al. Short photoluminescence lifetimes in vacuum-deposited CH3NH3PbI3 perovskite thin films as a result of fast diffusion of photogenerated charge carriers. *J. Phys. Chem. Lett.* **10**, 5167–5172 (2019).
39. Trimpl, M. J. et al. Charge-carrier trapping and radiative recombination in metal halide perovskite semiconductors. *Adv. Funct. Mater.* **30**, 2004312 (2020).
40. Shockley, W. & Read, W. T. Statistics of the recombination of holes and electrons. *Phys. Rev.* **87**, 835 (1952).

41. Hall, R. N. Electron–hole recombination in germanium. *Phys. Rev.* **87**, 387–387 (1952).
42. Shen, Y. C. et al. Auger recombination in InGaN measured by photoluminescence. *Appl. Phys. Lett.* **91**, 141101 (2007).
43. Iwata, Y., Banal, R. G., Ichikawa, S., Funato, M. & Kawakami, Y. Emission mechanisms in Al-rich AlGaN/AlN quantum wells assessed by excitation power dependent photoluminescence spectroscopy. *J. Appl. Phys.* **117**, 075701 (2015).
44. Zhang, F. et al. Comparative studies of optoelectrical properties of prominent PV materials: halide perovskite, CdTe, and GaAs. *Mater. Today* **36**, 18–29 (2020).
45. Hutter, E. M., Eperon, G. E., Stranks, S. D. & Savenije, T. J. Charge carriers in planar and meso-structured organic–inorganic perovskites: mobilities, lifetimes, and concentrations of trap states. *J. Phys. Chem. Lett.* **6**, 3082–3090 (2015).
46. Richter, J. M. et al. Enhancing photoluminescence yields in lead halide perovskites by photon recycling and light out-coupling. *Nat. Commun.* **7**, 13941 (2016).
47. Wen, X. et al. Defect trapping states and charge carrier recombination in organic-inorganic halide perovskites. *J. Mater. Chem. C* **4**, 793–800 (2015).
48. Tian, Y. et al. Mechanistic insights into perovskite photoluminescence enhancement: light curing with oxygen can boost yield thousandfold. *Phys. Chem. Chem. Phys.* **17**, 24978–24987 (2015).
49. Andaji-Garmaroudi, Z., Anaya, M., Pearson, A. J. & Stranks, S. D. Photobrightening in lead halide perovskites: observations, mechanisms, and future potential. *Adv. Energy Mater.* **10**, 1903109 (2019).
50. Staub, F., Kirchartz, T., Bittkau, K. & Rau, U. Manipulating the net radiative recombination rate in lead halide perovskite films by modification of light outcoupling. *J. Phys. Chem. Lett.* **8**, 5084–5090 (2017).
51. Shen, J.-X., Zhang, X., Das, S., Kioupakis, E. & Van de Walle, C. G. Unexpectedly strong auger recombination in halide perovskites. *Adv. Energy Mater.* **8**, 1801027 (2018).
52. Herz, L. M. Charge-carrier dynamics in organic–inorganic metal halide perovskites. *Annu. Rev. Phys. Chem.* **67**, 65–89 (2016).
53. Fassl, P. et al. Fractional deviations in precursor stoichiometry dictate the properties, performance and stability of perovskite photweovoltaic devices. *Energy Environ. Sci.* **11**, 3380–3391 (2018).
54. Ščajev, P. et al. Two regimes of carrier diffusion in vapor-deposited lead-halide perovskites. *J. Phys. Chem. C* **121**, 21600–21609 (2017).
55. Sherkar, T. S., Momblona, C., Gil-Escrig, L., Bolink, H. J. & Koster, L. J. A. Improving perovskite solar cells: insights from a validated device model. *Adv. Energy Mater.* **7**, 1602432 (2017).
56. Tessler, N. & Vaynzof, Y. Insights from device modeling of perovskite solar cells. *ACS Energy Lett.* **5**, 1260–1270 (2020).
57. Reichert, S. et al. Probing the ionic defect landscape in halide perovskite solar cells. *Nat. Commun.* **11**, 6098 (2020).
58. Fassl, P. et al. Effect of density of surface defects on photoluminescence properties in MAPbI 3 perovskite films. *J. Mater. Chem. C* **7**, 5285–5292 (2019).
59. Yang, Y. et al. Top and bottom surfaces limit carrier lifetime in lead iodide perovskite films. *Nat. Energy* **2**, 16207 (2017).
60. Wolff, C. M., Caprioglio, P., Stolterfoht, M. & Neher, D. Nonradiative recombination in perovskite solar cells: the role of interfaces. *Adv. Mater.* **31**, 1902762 (2019).
61. Noel, N. K. et al. Enhanced photoluminescence and solar cell performance via Lewis base passivation of organic–inorganic lead halide perovskites. *ACS Nano* **8**, 9815–9821 (2014).
62. Chen, S. et al. Light illumination induced photoluminescence enhancement and quenching in lead halide perovskite. *Sol. RRL* **1**, 1600001 (2017).
63. Xu, W. et al. Rational molecular passivation for high-performance perovskite light-emitting diodes. *Nat. Photonics* **13**, 418–424 (2019).
64. Yang, M. et al. Do grain boundaries dominate non-radiative recombination in $CH_3NH_3PbI_3$ perovskite thin films? *Phys. Chem. Chem. Phys.* **19**, 5043–5050 (2017).
65. Yin, W. J., Shi, T. & Yan, Y. Unique properties of halide perovskites as possible origins of the superior solar cell performance. *Adv. Mater.* **26**, 4653–4658 (2014).
66. Xu, W. et al. Precisely controlling the grain sizes with an ammonium hypophosphite additive for high-performance perovskite solar cells. *Adv. Funct. Mater.* **28**, 1802320 (2018).
67. Ren, X. et al. Modulating crystal grain size and optoelectronic properties of perovskite films for solar cells by reaction temperature. *Nanoscale* **8**, 3816–3822 (2016).

Acknowledgements

This work was supported by the Swedish Research Council (2016-04433) and Knut and Alice Wallenberg foundation (2016.0059). J.L. thanks China Scholarship Council (CSC No. 201608530162) for a Ph.D. scholarship. Theoretical work was supported by the Russian Science foundation Project (20-12-00202). P.A.F. and S.S. thank the Wenner-Gren foundation for the visiting (GFOh2018-0020) and postdoctoral (UPD2019-0230) scholarships. This work was supported by the European Research Council (ERC) under the European Union's Horizon 2020 research and innovation programme (ERC Grant Agreement No. 714067, ENERGYMAPS). Y.V. and Q.A. also thank the Deutsche Forschungsgemeinschaft (DFG) for funding the <PERFECT PVs> project (Grant No. 424216076) in the framework of SPP 2196. We thank Dr. Fabian Paulus for performing and analysing the XRD measurements and Prof. Jana Zaumseil for providing access to the XRD facilities.

Author contributions

I.G.S. conceived and planned the experiments with input from P.A.F. and A.K., A.K. designed and built the automated PLQY mapping setup with contributions from I.G.S., A.K., and A.Y. performed PLQY mapping and PL decay measurements. Q.A., J.L., and S.S. prepared the samples and carried out sample characterization. Q.A. performed the UV–vis and SEM measurements. P.A.F. developed the theory, carried out the modelling and wrote the theoretical part of the manuscript. I.G.S., P.A.F. and Y.V. determined the main ideas of the study and supervised the project. I.S. wrote the manuscript with great contributions by Y.V. and P.A.F. All authors have discussed the results and commented on the final manuscript.

Funding

Open access funding provided by Lund University.

Competing interests

The authors declare no competing interests.

Additional information

Supplementary information The online version contains supplementary material available at https://doi.org/10.1038/s41467-021-23275-w.

Correspondence and requests for materials should be addressed to P.A.F., Y.V. or I.G.S.

Peer review information *Nature Communications* thanks Michele Saba and the other, anonymous, reviewer(s) for their contribution to the peer review of this work. Peer reviewer reports are available.

Reprints and permission information is available at http://www.nature.com/reprints

Publisher's note Springer Nature remains neutral with regard to jurisdictional claims in published maps and institutional affiliations.

Open Access This article is licensed under a Creative Commons Attribution 4.0 International License, which permits use, sharing, adaptation, distribution and reproduction in any medium or format, as long as you give appropriate credit to the original author(s) and the source, provide a link to the Creative Commons license, and indicate if changes were made. The images or other third party material in this article are included in the article's Creative Commons license, unless indicated otherwise in a credit line to the material. If material is not included in the article's Creative Commons license and your intended use is not permitted by statutory regulation or exceeds the permitted use, you will need to obtain permission directly from the copyright holder. To view a copy of this license, visit http://creativecommons.org/licenses/by/4.0/.

© The Author(s) 2021

Paper IV

RESEARCH ARTICLE

ADVANCED OPTICAL MATERIALS
www.advopticalmat.de

Photoluminescence Mapping over Laser Pulse Fluence and Repetition Rate as a Fingerprint of Charge and Defect Dynamics in Perovskites

*Shraddha M. Rao, Alexander Kiligaridis, Aymen Yangui, Qingzhi An, Yana Vaynzof, and Ivan G. Scheblykin**

Defects in metal halide perovskites (MHP) are photosensitive, making the observer effect unavoidable when laser spectroscopy methods are applied. Photoluminescence (PL) bleaching and enhancement under light soaking and recovery in dark are examples of the transient phenomena that are consequent to the creation and healing of defects. Depending on the initial sample composition, environment, and other factors, the defect nature and evolution can strongly vary, making spectroscopic data analysis prone to misinterpretations. Herein, the use of an automatically acquired dependence of PL quantum yield (PLQY) on the laser pulse repetition rate and pulse fluence as a unique fingerprint of both charge carrier dynamics and defect evolution is demonstrated. A simple visual comparison of such fingerprints allows for assessment of similarities and differences between MHP samples. The study illustrates this by examining methylammonium lead triiodide ($MAPbI_3$) films with altered stoichiometry that just after preparation showed very pronounced defect dynamics at time scale from milliseconds to seconds, clearly distorting the PLQY fingerprint. Upon weeks of storage, the sample fingerprints evolve toward the standard stoichiometric $MAPbI_3$ in terms of both charge carrier dynamics and defect stability. Automatic PLQY mapping can be used as a universal method for assessment of perovskite sample quality.

S. M. Rao, A. Kiligaridis, A. Yangui, I. G. Scheblykin
Chemical Physics and NanoLund
Lund University
P.O. Box 124, 22100 Lund, Sweden
E-mail: ivan.scheblykin@chemphys.lu.se
Q. An, Y. Vaynzof
Chair for Emerging Electronic Technologies
Technical University of Dresden
Nöthnitzer Str. 61, 01187 Dresden, Germany
Q. An, Y. Vaynzof
Leibniz-Institute for Solid State and Materials Research Dresden
Helmholtzstraße 20, 01069 Dresden, Germany

The ORCID identification number(s) for the author(s) of this article can be found under https://doi.org/10.1002/adom.202300996

© 2023 The Authors. Advanced Optical Materials published by Wiley-VCH GmbH. This is an open access article under the terms of the Creative Commons Attribution-NonCommercial License, which permits use, distribution and reproduction in any medium, provided the original work is properly cited and is not used for commercial purposes.

DOI: 10.1002/adom.202300996

1. Introduction

Metal halide perovskites (MHPs) are an important class of semiconductors, that received significant attention over the last decade due to their excellent optoelectronic properties and promising performance in various optoelectronic devices.[1–3] Methylammonium lead triiodide ($MAPbI_3$ or MAPI) has since proven to be an excellent representative of the versatility of perovskites and has emerged as a promising photovoltaic material. Understanding charge carrier dynamics and defect physics in these semiconductors is critically important for advancing the progress in making stable devices with reproducible properties for optoelectronic applications.[4–9] Despite extensive studies, many contradicting observations have been reported that continue to puzzle researchers. The main challenges of working with perovskites are: i) poor sample storage stability, ii) poor reproducibility in sample fabrication,[10,11] and iii) evolution of the material under light irradiation, current flow, and electric field[12–18] and material self-healing.[19–22] Most of these difficulties, as well as advantages like, e.g., self-healing originate from low energy of defect formation, easiness of material recrystallization,[5] the ionic nature of the defect states and their metastability[22–26] due to very efficient ion migration in MHPs.[15,27,28]

Unreliable performance of MHPs correlates with the extreme sensitivity on the specific details of the fabrication process,[10,29–32] one of them being stoichiometries of precursor solutions.[33,34] Previous studies have shown how unintentional and fractional discrepancies as low as 0.5–1% in precursor ratios lead to samples with very different surface energetics and emission properties,[11] even when their absorbance and film morphology remain unchanged.

Photoluminescence (PL) spectroscopy is a very powerful and popular tool to rationalize MHPs due to extreme sensitivity of PL properties to defect states.[8] Recently a unique 2D photoluminescence quantum yield mapping technique (PLQY(*f*,P) mapping, where *f*-pulse repetition rate and P-pulse fluence) to

characterize charge carrier dynamics in polycrystalline MAPI films was demonstrated.[35] This new technique provides extensive information to unravel the various photophysical processes that occur with charge carriers in luminescence semiconductors like radiative recombination, trapping, trap-assisted non-radiative recombination, Auger recombination. The amount of data is sufficient for extracting the rate constants and trap densities by applying appropriate theoretical models to fit the PLQY map and PL decay kinetics. However, it was shown that even for the classical, rather stable MAPI films it is not possible to fully explain the observed PLQY(*f*,P) maps and PL decay kinetics measured from the same sample using an extended Shockley-Read-Hall (SRH+) model of charge recombination, the reason for this is not yet known. It was proposed that the PLQY(*f*,P) map can be used as the sample fingerprint[16,35] because it reflects the peculiarities of charge carrier dynamics at very different excitation conditions in terms of charge carrier concentration created by one laser pulse (pulse fluence ranges over four orders of magnitude) and the time gap between laser pulses (ranges over six orders of magnitude from 10 ns to 10 ms).

In this work we concentrate on a very important aspect of MHPs that is, although known for practicing laser spectroscopists,[8] usually not in focus of publications discussing charge carrier dynamics extracted from laser spectroscopy experiments. We talk about defect state instability under light and defect state evolution over the sample age. This can lead to irreproducibility of experimental data and so-called "observer effect", which means that the experiment itself changes the sample. The latter also means that the apparent results of the experiment depend on the particular experimental details which at first glance should not matter, for example the order of measured data points, waiting time between consecutive measurements and other factors. The importance of the observer effect should not be overlooked because most probably it is present in all published data on MHPs to one extent or another and can lead to the proposition of various theories and explanations which in fact might be a consequence of measurement induced artefacts. Because the PLQY(*f*,P) mapping is fully automated, it is ideal for comparison of samples possessing the observer effect, because the experimental conditions can be kept absolutely identical for all samples.

We measured the PLQY(*f*,P) maps of $MAPbI_3$ films prepared with fractional variations in the precursor stoichiometry. We focus on exploring overstoichiometric films (iodide fraction higher than three) as those were shown to result in a superior photovoltaic performance.[11] The PLQY maps reveal sensitive changes in the sample PL and stability over time. We found the presence of reversible light-induced fast dynamics in the non-stoichiometric MAPI pointing to the dependence of the defect state concentration on the history of light exposure of the samples. These fast defect kinetics at times scales of seconds are easily hidden from conventional spectroscopic investigations. We also observe maturing/healing of the samples over their shelf storage time over weeks leading to a more stable PL response and PLQY maps close to that of the standard $MAPI_3$. The advantage of the PLQY mapping is such that all these features are easily detected by simple visual comparison of the PLQY maps making this technique highly useful for monitoring of the perovskite sample quality.

2. Experimental Section

The samples were synthesized using a previously reported method, where the precursor stoichiometry was carefully controlled by varying the ratio between MAI and $Pb(OAc)_2$ to yield MAPI films with fractionally varying stoichiometries: stoichiometrically balanced $MAPbI_3$, slightly over-stoichiometric $MA_{1.04}PbI_{3.04}$ and significantly over-stoichiometric $MA_{1.1}PbI_{3.1}$ (See Note S1, Supporting Information, for details). They were stored in a nitrogen environment, isolated from light exposure before and between measurements. The PL of the samples was excited and imaged using a home-built wide-field photoluminescence microscope based on Olympus IX71 and an EMCCD Camera (ProEM, Princeton Instruments). The samples were excited using a 485 nm diode laser (PicoQuant), controlled by a multichannel laser driver (SEPIA LD828, PicoQuant).

The PLQY mapping entails exciting the sample with a pulsed laser at repetition rate f [s^{-1}] and pulse fluence P [photons/cm^2/pulse] that were controlled by the laser driver and a neutral density filter wheel, respectively. For each combination of f and P and PL intensity (PL image for the setup) of the sample was measured. Because the entire system was calibrated, this data was later converted to the external PLQY (see Note S2, Supporting Information). To obtain the PLQY(*f*,P) map, PL was measured for a laser excitation spanning five orders of magnitude (from *ca.* 10^8 to 10^{12} photons/cm^2/pulse) in five steps with power fluences P1, P2, P3, P4, and P5 (each step changes the fluence approximately ten times) and almost seven orders of magnitude in pulse repetition rate, i.e., from 100 Hz to 80 MHz with the repetition rate changed by ≈2–3 times each step. For each pulse fluence P, the repetition rate, f, was scanned across the entire range. The final PLQY(*f*,P) map was plotted as PLQY versus the time averaged power density, W, which is defined as $W = \text{photon energy} \cdot f \cdot P$ with units W cm^{-2}. In total the map consists of ≈80 data points, see Note S3 (Supporting Information) for details.

Data acquisition was designed so that all data points for the entire PLQY(*f*,P) map were acquired automatically (**Figure 1**a). All components of the setup were controlled by a LabVIEW program that executes the experiment according to a pre-loaded table of parameters of the data acquisition (*f*, P, shutter timing, acquisition time of the camera, filters, etc.). To avoid unnecessary sample exposure, the shutter was synchronized with camera to allow the laser beam reaching the sample during the PL acquisition only. The program automatically saved the PL images, which were later processed using another program to yield the PLQY map. This ensured that the data acquisition conditions were absolutely reproducible meaning that the same experiment could be repeated with another sample. Automation also excludes human errors that are unavoidable when such long series of data at varied conditions are measured. The entire measurement took from 1 to 3 h, where the longest time took to acquire data for low P and low f values since exposure times as long as several minutes per data point were often required. In our particular case the total exposure of the sample was ≈19 J cm^{-2} that, however, was spread over ≈1 h of the experiment.

© 2023 The Authors. Advanced Optical Materials published by Wiley-VCH GmbH

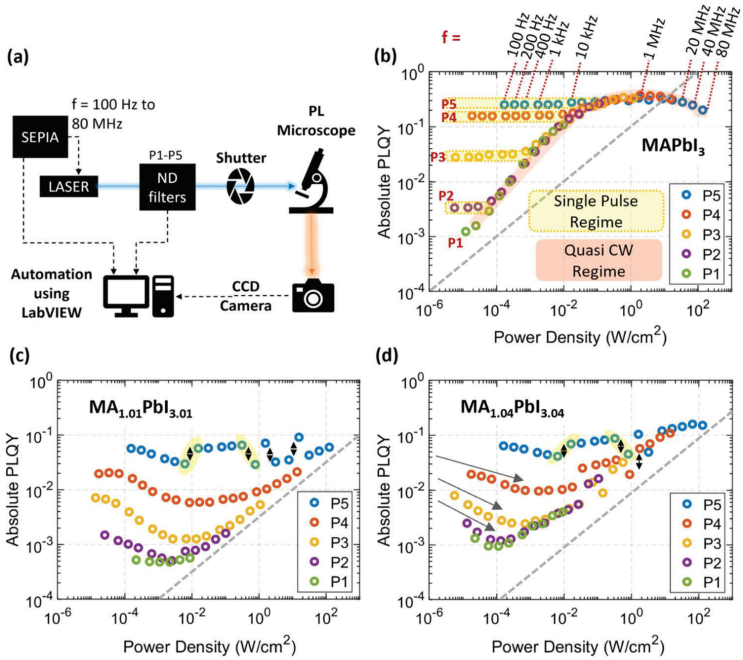

Figure 1. a) A schematic representation of the setup for acquisition of PLQY(f,P) maps. PLQY maps of b) $MAPbI_3$, c) $MA_{1.04}PbI_{3.04}$, and d) $MA_{1.1}PbI_{3.1}$ films. The map is formed by plotting together a family of 5 curves of PLQY versus Power Density. Each curve is obtained for its own pulse fluence, Pn. P1 is the lowest and P5 is the highest pulse fluence (in photons/cm^2/pulse). The scanning of the laser repetition rate f is illustrated in (b) for pulse fluence P5. See the text for details. The grey dash lines show the square root dependence between the excitation power density and PLQY, which aids to compare the slopes of the quasi-CW-regime of the samples. Different excitation regimes are marked in (b).

3. Results and Discussion

3.1. PLQY Map of the Standard $MAPbI_3$ and Explanation of the Excitation Regimes

First, let us consider the PLQY(f,P) maps of the fresh samples, as shown in Figure 1. A family of PLQY versus excitation power density curves, one for each pulse fluence (P1, P2, etc) are plotted together to give the final PLQY(f,P) map. The map of the stoichiometric MAPI film is quite close to the one previously reported.[35] The over stoichiometric samples show very differently looking maps: PLQY is lower at all conditions and the shape of the features of the map is unusual. Already here the visual comparison of the PLQY maps reveals that these samples are very different in terms of their PL and response to light irradiation in comparison to the stoichiometric MAPI.

The PLQY map of the standard MAPI is used here to recall the signatures of the different excitation regimes and charge recombination channels in semiconductors.[35] The data points on the PLQY map can be distinguished as belonging to two excitation regimes: i) the single pulse regime that is marked in yellow on Figure 1a, where the PLQY data points for fixed P follow a straight horizontal line when f is changed; ii) the Quasi-CW regime that is marked in orange on Figure 1a, where we observe merging of the individual lines measured at fixed P into one common dependence where PLQY depends the averaged power density W = photon energy·f·P only. In the single pulse regime, the PL excited by one laser pulse is free from the memory of the excited state dynamics produced by the previous pulse. In the quasi-CW regime, to the contrary, the PL excited by the first pulse affects the evolution of the PL induced by the next pulse because the time interval between two consecutive pulses is too short to ensure complete relaxation of all transient species (free and trapped charge carriers) created by the previous pulse. The existence of these two regimes is rather obvious and discussed in detail elsewhere.[35]

The PLQY map of our reference sample, plotted in the manner as shown in Figure 1a, with some imagination resembles a "horse neck with mane", where the "neck" corresponds to the quasi-CW regime, and the "mane" is formed by the separate strands of single pulse regime data points collected for fixed values of P (P1, P2,..., P5).[35] These features of the PLQY maps will be referred to in the following sections of the article to explain, analyze and compare the MAPI film samples.

The dotted grey line shows a square root dependence of PLQY on the average excitation power density (slope 0.5 in the log-log plot) expected for the quasi-CW regime in the case of

© 2023 The Authors. Advanced Optical Materials published by Wiley-VCH GmbH

photodoping (SRH model without trap saturation). The line is used as a reference for the slopes of the quasi-CW regime. The map of the stoichiometric MAPI film shows a quasi-CW slope of ≈0.77 that was previously explained by a partial trap saturation,[35] and the single pulse regime forming well-separated, almost horizontal lines for different pulse fluences. This PLQY map can be reasonably well explained by an extended SRH charge recombination model.[35]

3.2. PLQY Maps of the Overstoichiometric MAPI and Evidence of the Observer Effect

As seen in Figure 1c,d, the PLQY maps of overstoichiometric MAPI samples differ substantially from the standard map. First, the maps are shifted down in comparison with the reference, indicating a lower absolute PLQY at all excitation regimes. Second, the slope of the quasi-CW regime is reduced to 0.5 for the slightly over-stoichiometric MAPI (Figure 1c) and to <0.5 for the significantly over-stoichiometric MAPI sample (Figure 1d). Third, for both these samples the single-pulse regimes show an uncharacteristic initial reduction of PLQY as f increases (marked by three grey arrows in Figure 1d) and then a recovery to join the quasi-CW "horse neck". Changes of PLQY in the single pulse regime are not consistent with any charge recombination model where the defect concentration and trapping rates are static. Note that these maps were highly reproducible when measured multiple times for each different sample, at nine different locations within the samples. So, we must investigate the possibility that the data acquisition itself changes the charge recombination dynamics, or in order words, we need to examine the presence of the observer effect.

Another highly unusual feature clearly visible in the PLQY maps of $MA_{1.04}PbI_{3.04}$ and somewhat less pronounced for $MA_{1.1}PbI_{3.1}$ sample, is an apparent "discontinuity" in the single-pulse regime ("horse mane") for the highest pulse fluence P5, as marked by yellow ovals highlighted with double-sided arrows. This feature was reproduceable, irrespectively in the particular sample or the excitation spatial location. Even multiple measurements at the same region yielded the same peculiar jumps in the PLQY values by a factor of two without any obvious reason. As we will show below, this feature has the same origin as the previously discussed "curved single pulse regime": it is the observer effect, related to photosensitivity of the material and the exact details of sample light exposure controlled by a shutter and the time window over which the PL photons are acquired by the camera at the sub-second timescale.

3.3. PL Response on Switching the Laser, Reversible Bleaching

Before we explain the reasons for these unexpected observations, let us discuss the time-resolved response of the PL intensity on switching the laser excitation on (**Figure 2**). During this experiment the PL signal from $MA_{1.04}PbI_{3.04}$ sample was recorded constantly with 0.03 s time resolution while the shutter blocking the laser beam was opened and closed multiple times. The PL intensity is high at the start of each excitation period, but quickly

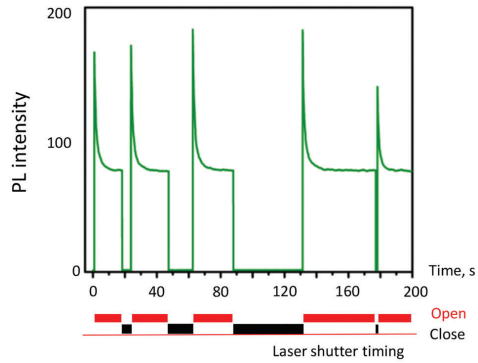

Figure 2. Evolution of PL of $MA_{1.04}PbI_{3.04}$ sample under interrupted laser irradiation (pulse repetition rate 10 MHz, pulse fluence P5). PL is bleaching at the time scale of seconds, however, after a short rest in dark, the PL intensity fully recovers.

declines by approximately a factor of two, reaching a steady state value. Remarkably, after a few seconds in dark, the sample shows exactly the same PL response when excited again, meaning that the observed PL bleaching (or decline) under illumination is fully reversible. This reversible PL dynamics at timescale from milliseconds to tens of seconds (depending on the excitation power density) must affect the PL intensity measurements for PLQY mapping.

An important point to note is that for measuring of a PLQY map the data acquisition is programmed for a minimum, but sufficient acquisition time. For a low power density excitation, the PLQY is very low and the acquisition times as long as 10–300 s are needed, whereas for high excitation power densities, acquisition times from 0.07 to 1 s are sufficient. Considering the fast bleaching noted above, we expect the PL intensity to change during the acquisition time of the data points of the PLQY(f,P) map.

3.4. Quantitative Assessment of the Effect of Temporal PL Bleaching on the PLQY Map

3.4.1. The Curvature in the Single Pulse Regime

To consider this, we modified the acquisition scheme in such a way that instead of one long acquisition time per data point, a movie of the same length consisting of several images was recorded. This allows us to monitor the PL intensity evolution during the data acquisition of selected datapoints of the PLQY map.

Figure 3a shows a part of the PLQY map with the peculiar "dip" in the single pulse regime for the $MA_{1.1}PbI_{3.1}$ sample (green circles). The same figure also shows the data for the reference MAPI that is horizontal as is to be expected (black diamonds). The other panels of the figure show the time-resolved PL kinetics during the single acquisition of 6 selected data points where the "dip" is observed (f varies from 400 Hz to 50 kHz). The green coloration shows the integrated signal that is actually measured and plotted at the PLQY map. The pink coloration shows the

© 2023 The Authors. Advanced Optical Materials published by Wiley-VCH GmbH

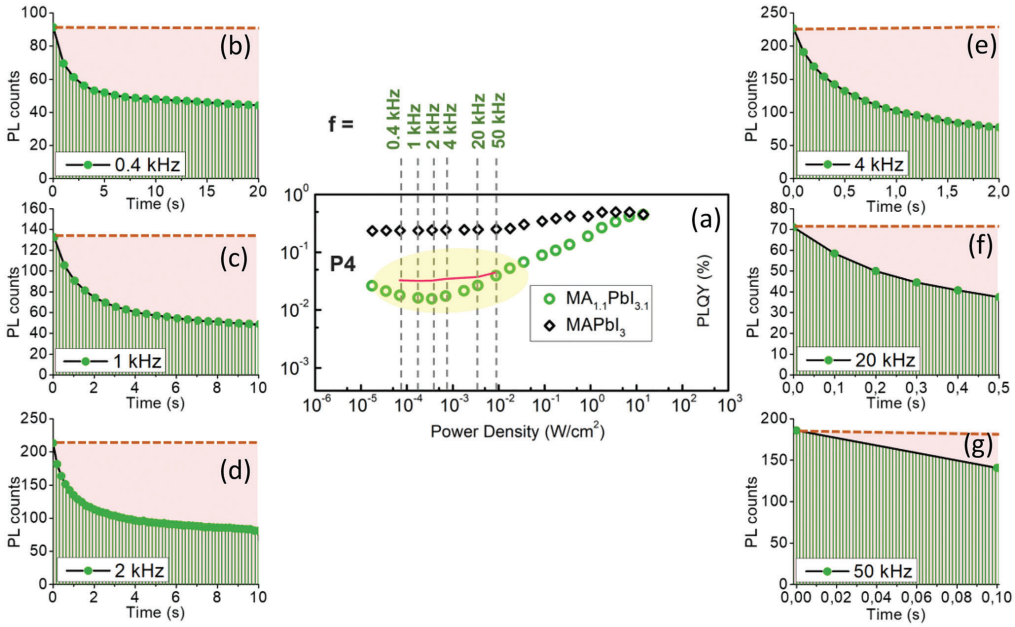

Figure 3. a) Dependence of PLQY on repetition rate *f* for the pulse fluence P4 for the significantly overstoichiomeric $MA_{1.1}PbI_{3.1}$ (green circles) and for the stoichiometric $MAPbI_3$ (black diamonds). For frequencies <50 kHz we expect to have single pulse excitation regime implying constant PLQY as the $MAPbI_3$ sample shows. The dependence for the overstoichiomeric sample, however, shows unusual bending down with the lowest value at 2 kHz. This unusual region is highlighted by yellow, see also Figure 1d. The reason for that is PL kinetics at the time scale of the signal acquisition illustrated in (b–g). The time range for each plot is equal to the signal acquisition time for the corresponding datapoints shown in (a). PL signal evolution is shown in green. The integrals under these curves (green coloration) are proportional to the measured PLQY ((a), green circles). The pink rectangular areas show the "true" PL signal as it would be if the sample was stable. The red line in (a) shows these "true" values which, as expected, form a horizontal line in the given repetition rate range. So, the anomaly in PLQY shown in (a) is due to the PL bleaching at the time scale of seconds shown in (b–g).

expected signal in the case PL did not decrease during the acquisition time. These expected PLQY values are illustrated by the pink line. This data demonstrates that it is the PL dynamics just after switching on the excitation laser that is responsible for the data points being lower than expected at the certain regions of the PLQY map. The behavior of the "corrected" PLQY (pink line) is close to the constant PLQY as expected from the single pulse regime.

Because the acquisition time and power density are different for different data points, and the PL bleaching kinetic does not scale in the same way as the sample exposure time needed for PL collection, the influence of the PL bleaching is different for different regions of the PLQY map. It not only results in the downward shift in the PLQY map (PL bleaching means lower PLQY), but also impacts on its shape that can be immediately detected by visually analyzing the maps. Obviously, the experiment is heavily influenced by the observer effect, i.e., when the excitation light required to induce PL also leads to a change in the material, thus resulting in the change of the observable parameter (PL in our case).

3.4.2. Jump-Like Artefacts, Effect of Synchronization between the Shutter and the Camera

Let us consider the region of the map where the average excitation power is quite large and PLQY is also large. In this region the acquisition time needed for obtaining a good signal is very short. Due to the limitation of the shutter installed at the laser beam, the minimum irradiation time of the sample is 70 ms. As one can see in Figure 3, the PL bleaching at high excitation power is very fast with a characteristic time of the order of 100 ms. Importantly, there are two time-intervals that need to be synchronized throughout the experiment: the opening and closing of the shutter blocking the laser (light irradiation interval) and the starting and stopping of the data collection by the CCD camera (data acquisition interval). For a stable sample, the PL signal is just proportional to the overlapping time between these two intervals. However, when the sample is not stable during the measurement, particular details of the timing between the shutter and CCD start to become crucially important (**Figure 4**). Note that these considerations are not limited to PL intensity

© 2023 The Authors. Advanced Optical Materials published by Wiley-VCH GmbH

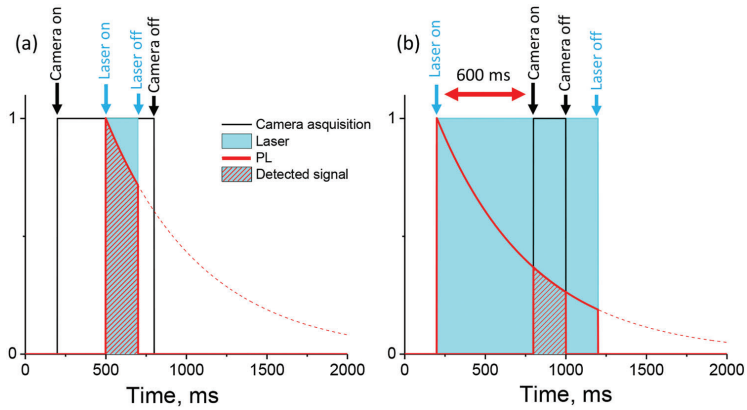

Figure 4. A schematic representation of the critical importance of synchronization between the laser irradiation interval and the signal acquisition window. The evolution of PL intensity after opening the laser shutter is shown by the red line. a) Data acquisition in the "fast shutter mode", where the effective data acquisition time is equal to the laser irradiation time as both are determined by the laser shutter. b) Data acquisition in the "slow shutter mode", where there is a delay between the start of the laser illumination and the start of PL acquisition. This delay is 600 ms in our experiments. The acquisition time is 100 ms in both cases, however, the signal detected in (b) is several times smaller than in (a) due to the PL bleaching over the first 600 ms after opening the laser shutter.

measurements, they are valid for any optical experiments and careful experimentalists must consider them.

The jump-like artefacts observed for non-stoichiometric samples at several positions on their PLQY maps originate from the issue mentioned above. The reason for the drastic jumps of the PLQY from one data point to another observed in some regions of the PLQY map is that they originate from the two different regimes of the data acquisition in terms of the synchronization between the laser irradiation and PL acquisition time intervals.

Figure 4 illustrates these two different modes used in the measurements. The reason for having these two different modes in the setup was purely historical, as it is common in any setup/measurement routine that is constantly under development in a research lab. The two modes being: a) the "fast shutter" mode, where the sample irradiation and PL collection intervals are identical (perfect synchronization, was used for irradiations times <100 ms), and b) the "slow shutter" mode where the sample irradiation time is longer than the PL acquisition time (delayed synchronization, was used when the irradiation time >100 ms). It is obvious that if PL is bleaching at the time scale comparable with the synchronization delay (600 ms), the PL intensity measured with the "slow shutter" should be smaller than that measured with the "fast shutter" for the same PL acquisition time, as represented in Figure 4c. However, when the acquisition time is >1 s, there should be no difference between these two modes.

The easily observed reproducible artefacts visible in the PLQY maps are therefore due to sensitivity of the overstoichiometric samples to light. In fact, we do not see any real possibility to eliminate these artefacts. The observer effect is always there. We can only conclude that by applying automatic measurement routines, for example, PLQY(*f*,P) mapping, it is possible to identify and classify samples by their photosensitivity.

3.5. Time Evolution of the PLQY Maps during Long-Term Storage

Having identified the reasons for the artefacts in the PLQY maps, we examine how these maps change upon storage of the samples. We always used the same data acquisition routine, that is why the maps of different samples and the same samples measured after different storage time can be directly compared. We find that the artefacts due to the defect dynamics in overstoichiometric samples decrease with the age of the films (**Figure 5**). The most drastic changes are for $MA_{1.04}PbI_{3.04}$. As the PLQY maps show, PLQY increases with age and the jumps due to fast dynamics at high excitation power also decrease. Although the PLQY map for the 6 weeks old sample still shows artefacts like non-constant PLQY for the single pulse regime, it has become much closer to the reference stoichiometric MAPI (compare with Figure 1b). This dramatic change in the PL response signifies healing of the sample. We hypothesize that the excessive iodide in the crystal structure (I^- interstitials inherent to overstoichiometric samples), first diffuse to the surface of the grains and then leave the surface over time upon exposure to oxygen and light illumination, see also the discussion in ref. [16] where healing of an overstoichiometric MAPI film was observed after deliberate photo-oxidation.

Evolution of the PLQY maps for the significantly overstoichiometric $MA_{1.1}PbI_{3.1}$, is shown in the bottom row, in Figure 5d–f. Although the PLQY value also slightly goes up as the sample ages, the artefacts due to fast light-induced defect dynamics remain the same. It means that when the degree of overstoichiometry is over a certain limit, the sample cannot spontaneously transform to its normal state. Even after long storage time it retains the charge carrier and defect dynamics significantly different from that of the stoichiometric MAPI film.

© 2023 The Authors. Advanced Optical Materials published by Wiley-VCH GmbH

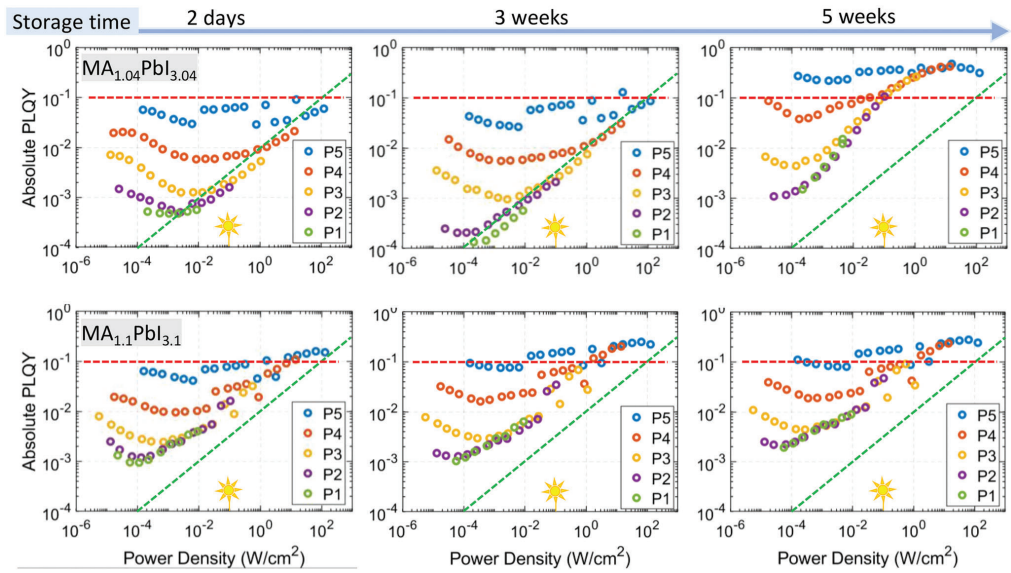

Figure 5. A series of PLQY(f,P) maps demonstrating the evolution of the response of the non-stoichiometric MAPI films as a function of the storage time after synthesis. Top raw—the slightly over-stoichiometric $MA_{1.04}PbI_{3.04}$, bottom raw—the significantly over-stoichiometric $MA_{1.1}PbI_{3.1}$ films. Red horizontal dash line shows PLQY = 10%, the tilted green dash line is the square root dependence (slope 0.5 in log-log scale) expected for the quasi-CW regime for the case of photodoping without trap saturation. These lines aid comparison of the plots between each other. The "sun" marks the excitation power density of 0.1 W cm^{-2}.

3.6. Possible Mechanisms and Origin of Defect Photosensitivity and Sample Maturing

To date there is no complete understanding about which particular defects are responsible for the apparent photosensitivity of MAPI exemplified in Figure 2. Note that we were not able to find any publication where PL evolution of MHPs on the sub-second time scale has been demonstrated. Our results as well as the literature data[18,25,26,36] indicate that iodide interstitials inherently present at high concentrations in overstoichiometric samples is at least one of the factors. The corresponding excess of MA^+ counter ions also exist in the overstoichiometric samples; however, they are believed to be much less important for non-radiative recombination processes.[37]

Here we would like to make a connection to the mixed halide perovskites (e.g., Br/I mixtures[38,39]) where the steady state of the material in terms of its bandgap and many other properties depends on the light (intensity, repetition rate for pulsed excitation[40,41]) the sample is irradiated by. Although it is easy to study phase segregation in these systems experimentally, even for the model $MAPbI_xBr_{3-x}$ perovskite the full physical picture of the processes is not yet established.[38] In general, steady state of any photosensitive material with reversible photo-induced reactions (mixed halides MHPs as a very clear case and, as we propose here, MHPs in general) is determined by kinetic equilibrium between several processes involving various reactants/products and photons (or electronic excitations). Changing of light irradiation condition inevitably changes the resulting equilibrated state. We speculate that in MAPI films initially containing lots of defects (I^- and MA^+ interstitials) irradiation by light intensifies the defect migration. This migration leads to spatial redistribution of ions and may lead to local segregation of the material in terms of defect concentration/local composition that results in enhanced non-radiative charge recombination in overstoichiometric samples. This material state exists in a dynamic equilibrium between light-driven segregation and gradient driven diffusion in analogy to mixed halide perovskites. In this model, the degree of segregation depends on the light intensity and so does the equilibrated value of PL.

3.7. The Observer Effect as a Problem for Understanding Perovskites

The reversible fast PL bleaching process discussed in this work can be easily overlooked because it happens on time scale of seconds while in most of experiments steady state values of parameters (in terms of the data acquisition time) are measured. Indeed, commonly the sample is considered unstable and not suitable for measurements only if the experimentally measured parameter in the second experiment is different (e.g., PL intensity is lower) from that measured in the first and so on. However, this simple test is not enough for photosensitive perovskites. Due to self-healing the measured parameters in the second experiment

© 2023 The Authors. Advanced Optical Materials published by Wiley-VCH GmbH

most probably will not be different from the first one. It means that the sample appears as "stable" as soon as the same experimental routine is applied again and again.

Indeed, the temporal bleaching we discuss here is not related to permanent degradation, but to the equilibrium state of the material under light irradiation. We observe that PL intensity changes when the material transfers to a new equilibrium when the irradiation conditions are changed (e.g., the laser was switched on, or the intensity of the laser is changed). As soon as the new equilibrium is reached, the PL (and therefore, the defect concentration) stabilizes. Whether or not the experimentalist has a chance to notice this instability depends on the interplay of multiple experimental conditions such as the sample relaxation time, data acquisition time, gaps between measurements, type of irradiation (constant, interrupted) and many other experimental details.

The problem with these steady-state data is that the quasi-stable equilibrium condition of the sample depends on the light intensity, which means that obtained steady-state parameters cannot be compared with the same parameters measured at different light irradiation conditions. In other words, changing the irradiation conditions is equivalent to changing the sample. This problem undermines the commonly applied method of varying photogenerated charge carrier concentration as the universal approach for understanding charge carrier dynamics.

Thanks to the automated experimental routine and the unique mapping in very large *f* and P space, we can immediately identify that some samples exhibit unusual behavior and should be not even tried to be analyzed without serious consideration of their photosensitivity. Strictly speaking, for materials with photosensitive defect concentration standard types of spectroscopic methods and theoretical models might not be fully applicable.

4. Conclusion

Automatically recorded PLQY(*f*,P) maps serve as easily readable fingerprints of sample electronic properties. Such a fingerprint depends on charge carrier recombination pathways which to a large extent are controlled by defect state properties and their concentration that can be strongly photosensitive. Photosensitivity of defect concentration is very pronounced in overstoichiometric films having excess of MA^+ and I^- in their composition. This was revealed in the PLQY(*f*,P) maps as clear artifacts beyond any sensible explanation in the framework of standard charge recombination models. These films show a strong observer effect, meaning that by performing an optical experiment one changes the sample and thus the results reflect properties of the material convoluted with the details of the experimental routine used in the particular laboratory. The reason behind these artifacts is that PL intensity reversibly declines under light exposure with characteristics timescale from hundreds of milliseconds to tens of seconds depending on light excitation conditions. Following these artifacts over the storage time of the film over weeks, we find that slightly overstoichiometric films change their properties toward being more stable, having a higher PLQY and PLQY(*f*,P) maps closer to the one for the standard MAPI. This phenomenon is one more example of the self-healing ability of metal halide perovskite semiconductors enabled by efficient ion diffusion in the crystal. The observer effect and self-healing must be considered in any optical and electronic measurement of metal halide perovskites.

Supporting Information

Supporting Information is available from the Wiley Online Library or from the author.

Acknowledgements

The work was supported by the Swedish Research Council (2020-03530). Q.A. and Y.V. thank the center for advancing electronics Dresden (cfaed) for generous funding in the framework of the postdoc program and the Deutsche Forschungsgemeinschaft (DFG) for funding the "PERFECT PVs" project (Grant No. 424216076) via the Special Priority Program 2196. Y.V. has received funding from the European Research Council (ERC) under the European Union's Horizon 2020 research and innovation programme (ERC grant agreement number 714067, ENERGYMAPS).

Conflict of Interest

The authors declare no conflict of interest.

Data Availability Statement

The data that support the findings of this study are available from the corresponding author upon reasonable request.

Keywords

defects, photoluminescence, photosensitivity, PLQY, semiconductors

Received: April 27, 2023
Revised: June 24, 2023
Published online:

[1] L. Schmidt-Mende, V. Dyakonov, S. Olthof, F. Ünlü, K. M. T. Lê, S. Mathur, A. D. Karabanov, D. C. Lupascu, L. M. Herz, A. Hinderhofer, F. Schreiber, A. Chernikov, D. A. Egger, O. Shargaieva, C. Cocchi, E. Unger, M. Saliba, M. M. Byranvand, M. Kroll, F. Nehm, K. Leo, A. Redinger, J. Höcker, T. Kirchartz, J. Warby, E. Gutierrez-Partida, D. Neher, M. Stolterfoht, U. Würfel, M. Unmüssig, et al., *APL Mater.* **2021**, *9*, 109202.
[2] A. K. Jena, A. Kulkarni, T. Miyasaka, *Chem. Rev.* **2019**, *119*, 3036.
[3] H. Dong, C. Zhang, X. Liu, J. Yao, Y. S. Zhao, *Chem. Soc. Rev.* **2020**, *49*, 951.
[4] J. M. Ball, A. Petrozza, *Nat. Energy* **2016**, *1*, 1.
[5] D. Cahen, L. Kronik, G. Hodes, *ACS Energy Lett.* **2021**, *6*, 4108.
[6] S. G. Motti, D. Meggiolaro, S. Martani, R. Sorrentino, A. J. Barker, F. De Angelis, A. Petrozza, *Adv. Mater.* **2019**, *31*, 1901183.
[7] S. Singh, Laxmi, D. Kabra, *J. Phys. D: Appl. Phys.* **2020**, *53*, 503003.
[8] K. P. Goetz, A. D. Taylor, F. Paulus, Y. Vaynzof, *Adv. Funct. Mater.* **2020**, *30*, 1910004.
[9] S. Kosar, A. J. Winchester, T. A. S. Doherty, S. Macpherson, C. E. Petoukhoff, K. Frohna, M. Anaya, N. S. Chan, J. Madéo, M. K. L. Man, S. D. Stranks, K. M. Dani, *Energy Environ. Sci.* **2021**, *14*, 6320.
[10] K. P. Goetz, Y. Vaynzof, *ACS Energy Lett.* **2022**, *7*, 1750.

© 2023 The Authors. Advanced Optical Materials published by Wiley-VCH GmbH

[11] P. Fassl, V. Lami, A. Bausch, Z. Wang, M. T. Klug, H. J. Snaith, Y. Vaynzof, *Energy Environ. Sci.* **2018**, *11*, 3380.
[12] Y. Tian, M. Peter, E. Unger, M. Abdellah, K. Zheng, T. Pullerits, A. Yartsev, V. Sundström, I. G. Scheblykin, *Phys. Chem. Chem. Phys.* **2015**, *17*, 24978.
[13] Y. Tian, A. Merdasa, E. Unger, M. Abdellah, K. Zheng, S. McKibbin, A. Mikkelsen, T. Pullerits, A. Yartsev, V. Sundström, I. G. Scheblykin, *J. Phys. Chem. Lett.* **2015**, *6*, 4171.
[14] L. Lin, L. Yang, G. Du, X. Li, Y. Li, J. Deng, K. Wei, J. Zhang, *ACS Appl. Energy Mater.* **2023**, https://doi.org/10.1021/acsaem.2c04120.
[15] J. Liu, M. Hu, Z. Dai, W. Que, N. P. Padture, Y. Zhou, *ACS Energy Lett.* **2021**, *6*, 1003.
[16] K. P. Goetz, F. T. F. Thome, Q. An, Y. J. Hofstetter, T. Schramm, A. Yangui, A. Kiligaridis, M. Loeffler, A. D. Taylor, I. G. Scheblykin, Y. Vaynzof, *J. Mater. Chem. C* **2023**, *11*, 8007.
[17] N. Phung, A. Mattoni, J. A. Smith, D. Skroblin, H. Köbler, L. Choubrac, J. Breternitz, J. Li, T. Unold, S. Schorr, C. Gollwitzer, I. G. Scheblykin, E. L. Unger, M. Saliba, S. Meloni, A. Abate, A. Merdasa, *Joule* **2022**, *6*, 2152.
[18] D. W. deQuilettes, W. Zhang, V. M. Burlakov, D. J. Graham, T. Leijtens, A. Osherov, V. Bulović, H. J. Snaith, D. S. Ginger, S. D. Stranks, *Nat. Commun.* **2016**, *7*, 11683.
[19] K. Domanski, B. Roose, T. Matsui, M. Saliba, S.-H. Turren-Cruz, J.-P. Correa-Baena, C. R. Carmona, G. Richardson, J. M. Foster, F. De Angelis, J. M. Ball, A. Petrozza, N. Mine, M. K. Nazeeruddin, W. Tress, M. Grätzel, U. Steiner, A. Hagfeldt, *Energy Environ. Sci.* **2017**, *10*, 604.
[20] D. Cahen, I. Lubomirsky, *Acc. Chem. Res.* **2017**, *50*, 573.
[21] D. R. Ceratti, R. Tenne, A. Bartezzaghi, L. Cremonesi, L. Segev, V. Kalchenko, D. Oron, M. A. C. Potenza, G. Hodes, D. Cahen, *Adv. Mater.* **2022**, *34*, 2110239.
[22] M. H. J. J. Galle, J. Li, P. A. Frantsuzov, T. Basché, I. G. Scheblykin, *Adv. Sci.* **2023**, *10*, 2204393.
[23] S. Seth, E. A. Podshivaylov, J. Li, M. Gerhard, A. Kiligaridis, P. A. Frantsuzov, I. G. Scheblykin, *Adv. Energy Mater.* **2021**, *11*, 2102449.
[24] A. Merdasa, Y. Tian, R. Camacho, A. Dobrovolsky, E. Debroye, E. L. Unger, J. Hofkens, V. Sundström, I. G. Scheblykin, *ACS Nano* **2017**, *11*, 5391.
[25] S. G. Motti, D. Meggiolaro, A. J. Barker, E. Mosconi, C. A. R. Perini, J. M. Ball, M. Gandini, M. Kim, F. De Angelis, A. Petrozza, *Nat. Photonics* **2019**, *13*, 532.
[26] S. G. Motti, D. Meggiolaro, S. Martani, R. Sorrentino, A. J. Barker, F. De Angelis, A. Petrozza, *Adv. Mater.* **2019**, *31*, 1901183.
[27] P. V. Kamat, M. Kuno, *Acc. Chem. Res.* **2021**, *54*, 520.
[28] C. Li, A. Guerrero, Y. Zhong, A. Gräser, C. A. M. Luna, J. Köhler, J. Bisquert, R. Hildner, S. Huettner, *Small* **2017**, *13*, 1701711.
[29] A. D. Taylor, Q. Sun, K. P. Goetz, Q. An, T. Schramm, Y. Hofstetter, M. Litterst, F. Paulus, Y. Vaynzof, *Nat. Commun.* **2021**, *12*, 1878.
[30] Ç. Odabaşı, R. Yıldırım, *Energy Technol.* **2020**, *8*, 1901449.
[31] M. S. Jamal, M. S. Bashar, A. K. M. Hasan, Z. A. Almutairi, H. F. Alharbi, N. H. Alharthi, M. R. Karim, H. Misran, N. Amin, K. B. Sopian, M. Akhtaruzzaman, *Renewable Sustainable Energy Rev.* **2018**, *98*, 469.
[32] Z. Chen, P. He, D. Wu, C. Chen, M. Mujahid, Y. Li, Y. Duan, *Front. Mater.* **2021**, *8*, 723169.
[33] W. S. Yang, B. W. Park, E. H. Jung, N. J. Jeon, Y. C. Kim, D. U. Lee, S. S. Shin, J. Seo, E. K. Kim, J. H. Noh, S. I.l Seok, *Science* **2017**, *356*, 1376.
[34] Q. Chen, H. Zhou, T.-B. Song, S. Luo, Z. Hong, H.-S. Duan, L. Dou, Y. Liu, Y. Yang, *Nano Lett.* **2014**, *14*, 4158.
[35] A. Kiligaridis, P. A. Frantsuzov, A. Yangui, S. Seth, J. Li, Q. An, Y. Vaynzof, I. G. Scheblykin, *Nat. Commun.* **2021**, *12*, 3329.
[36] P. Fassl, Y. Zakharko, L. M. Falk, K. P. Goetz, F. Paulus, A. D. Taylor, J. Zaumseil, Y. Vaynzof, *J. Mater. Chem. C* **2019**, *7*, 5285.
[37] S. Reichert, Q. An, Y.-W. W. Woo, A. Walsh, Y. Vaynzof, C. Deibel, *Nat. Commun.* **2020**, *11*, 6098.
[38] K. Suchan, J. Just, P. Beblo, C. Rehermann, A. Merdasa, R. Mainz, I. G. Scheblykin, E. Unger, *Adv. Funct. Mater.* **2023**, *33*, 2206047.
[39] M. C. Brennan, S. Draguta, P. V. Kamat, M. Kuno, *ACS Energy Lett.* **2018**, *3*, 204.
[40] X. Yang, X. Yan, W. Wang, X. Zhu, H. Li, W. Ma, C. Sheng, *Org. Electron.* **2016**, *34*, 79.
[41] A. J. Knight, L. M. Herz, *Energy Environ. Sci.* **2020**, *13*, 2024.

© 2023 The Authors. Advanced Optical Materials published by Wiley-VCH GmbH

Printed by Media-Tryck, Lund 2023 NORDIC SWAN ECOLABEL 3041 0903

LUND UNIVERSITY

Faculty of Science
Department of Chemistry
Division Chemical Physics

ISBN 978-91-7422-998-1